SURE 静岡大学学術リポジトリ
Shizuoka University REpository

Investigation of MoS2 layered nanostructures for photocatalytic applications

メタデータ	言語: en 出版者: Shizuoka University 公開日: 2017-12-14 キーワード (Ja): キーワード (En): 作成者: Sabarinathan, Mani メールアドレス: 所属:
URL	https://doi.org/10.14945/00024359

DOCTORAL THESIS

Investigation of MoS_2 layered nanostructures for photocatalytic applications

M. Sabarinathan

Graduate School of

Science and Technology, Educational Division

Department of Optoelectronics and Nanostructure Science

Shizuoka University

July 2017

ACKNOWLEDGEMENT

First, I express my sincere and esteemed gratitude to my Research guide and Supervisor, **Prof. Yasuhiro Hayakawa,** Professor, Research Institute of Electronics, Shizuoka University, for his constant encouragement, committed guidance at every stage of my research work.

I would like to thank **Prof. M. Shimomura, Prof. K. Hara** and **Prof. H. Tatsuoka,** Research Institute of Electronics, Shizuoka University, for the evaluation of the thesis and valuable comments to improve the research in future.

I wish to thank **Mr. T. Koyama** and **Mr. W. Tomoda** for their assistance in instrumentation handling and characterization of the samples.

I would like to thank **Shizuoka University** for the financial assistance to complete the research work.

Also, I would like to acknowledge the support of my fellow researcher **Dr. S. Harish**, Research scholar, Research Institute of Electronics, Shizuoka University.

Very special thanks to my brother **Dr. M. Navaneethan,** Assistant Professor, Research Institute of Electronics, Shizuoka University, Japan. And my Sister – in – law **Dr. J. Archana,** Assistant Professor (Research), Department of Physics & Nanotechnology, SRM Research Institute, SRM University, India for their encouragement and support throughout my research work.

Finally, I would like to dedicate this to my parents: **T. Mani, M. Pappal** without their unending support and love from childhood to now, I never would have made it through this process or any of the tough times in my life.

Thesis outline

CHAPTER NO.	TITLE	PAGE NO.
	ABSTRACT	**iv**
Chapter 1	**Introduction**	
	1.1 Background	1
	1.2 Impacts of Nanotechnology	3
	1.3 Preparation of Nanomaterials	6
	1.4 Semiconducting Nanomaterials	9
	1.5 Nanostructure Photocatalysts	11
	1.6 Review of Literature	13
	1.7 Problem statement and objectives	15
	References	17
Chapter 2	**Hydrothermal growth of ligand-assisted monodispersed MoS_2 layered nanostructures for the realization of ultrafast degradation of an organic pollutant**	
	2.1 Background	23
	2.2 Experimental procedure	25
	2.2.1 Hydrothermal growth of layered MoS_2 nanostructures	25
	2.2.2 Photocatalytic dye degradation	26
	2.2.3 Characterization techniques	27
	2.3 Results and Discussion	33
	2.3.1 Photocatalytic activity	43
	2.4 Conclusion	53
	References	53
Chapter 3	**Hydrothermal synthesis and functional properties of highly efficient visible light photocatalytic activity of 2D layered MoS_2-TiO_2 nanocomposite hybrid photocatalyst**	
	3.1. Background	58
	3.2 Experimental procedure	60
	3.2.1 Synthesis of 2D layered MoS_2 nanostructures	60
	3.2.2 Synthesis of layered MoS_2-TiO_2 mixtures heterostructure	60

3.2.3 Photocatalytic dye degradation 60

3.3 Results and discussion 61

3.3.1 Photocatalytic activity 68

3.4. Conclusion 77

References 78

Chapter 4 Investigate the photocatalytic properties of hydrothermally synthesized Cerium doped MoS_2 nanostructures under visible light irradiation

4.1. Background 82

4.2 Experimental procedure 84

4.2.1 Synthesis of Ce doped MoS_2 nanostructures 84

4.2.2 Photocatalytic dye degradation 84

4.3 Results and discussion 85

4.3.1 Photocatalytic activity 96

4.4. Conclusion 104

References 104

Chapter 5 Summary and future work

5.1. Summary 108

5.2. Future work 109

List of publications and conferences 111

ABSTRACT

Nanotechnology is a new field of research for fabrication of devices based on the enhanced properties of materials in the realm of 1 - 100 nm. Semiconductor nanostructures are expected to exhibit enhanced optical properties when compared to bulk semiconductors because of quantum confinement. These semiconductor structures have been widely used in various applications such as optical sensors, photocatalysts in environmental protection, flat panel displays, storage devices, blue laser diodes, light emitting diodes etc. Among them, semiconductor photocatalyst nanostructures are very closely linked with the technical assessments of environmental cleanup. A remedial action provides important inputs to the environmental assessment on technology design and dimensioning, which are expected short remediation time and high remediation efficiency. A remediation technology removes a local contamination and contribute to environmental purification on the local, regional and global scale. Water is the most basic and most essential compound of all living processes in our water planet. Despite many attempts to stop the destruction and pollution of water resources, humans' impact on the natural cycle of water make irreparable risks in this area and it requires a consideration on the necessity of the use of new methods to prevent contamination of water resources. Wastewater compounds may be physical, chemical or biological, and cause environmental impacts including changes in aquatic habitat and its special structure, and the change in biodiversity and water quality.

The synthesis of nanoparticles with uniform size and morphology is one of the most significant challenges in nanotechnology. For semiconductor nanoparticles, different emission wavelengths are obtained for different particle sizes, and so the control of particle size is very important for these systems. The traditional approaches to prepare nanoparticles involve co-precipitation, deposition - precipitation, ion exchange, impregnation, successive reduction and calcinations, etc. These approaches, however, experience lack of control over

size, shape and stability of the produced nanoparticles. It is well known that without surface active agents, a narrow size distribution is hardly achieved. Such controllability or processibility of size, shape and surface properties are important in delineating the size effect in nanostructured catalysis. An ideal nanoparticles catalyst system should be not only catalytically accessible, but also morphologically stable or controllable. This can be achieved by surface-capping approaches.

In the present work, Molybdenum disulfide (MoS_2) layered nanosheets were synthesized by the hydrothermal method. Citric acid was used as an organic ligand to obtain the monodispersed layered MoS_2 nanostructures. The effect of citric acid on the formation and functional properties of the layered MoS_2 nanostructures was investigated. The X-ray diffraction patterns (XRD) revealed the formation of a hexagonal crystal structure of MoS_2. Significant peak shift was observed for the interaction of citric acid and Mo in the core level spectra of X-ray photoelectron spectroscopy (XPS). Citric acid-free hydrothermal growth resulted in the formation of micron-sized MoS_2 spheres, whereas citric acid-assisted hydrothermal growth resulted in the formation of well dispersed MoS_2 layered nanostructures, confirmed by morphological analysis. However, the highest concentration (0.05 M) of citric acid resulted in the formation of aggregated layers. The obtained MoS_2 nanostructures were used as photocatalysts to decompose methylene blue (MB) as a model pollutant. The obtained results showed that the MoS_2 layered nanosheets could effectively decompose the organic pollutant. The MB absorption peaks completely disappeared after 24 min of irradiation when using the nanosheets synthesized with a citric acid concentration of 0.04 M. The effect of pH on the MoS_2 nanosheets was studied, and 96 % MB degradation was observed at pH 12 after 2 min of visible-light irradiation.

2D layered molybdenum disulfide (MoS_2) and MoS_2/TiO_2 nanocomposite were synthesized by the hydrothermal method. The effect of TiO_2 concentrations on the formation of MoS_2/TiO_2 composites and functional properties were investigated. XRD revealed the formation of hexagonal and anatase structure of MoS_2 and TiO_2, respectively. XPS confirmed the presence of Mo and Ti interaction by significant peak shift. Morphological analysis revealed the formation of TiO_2 grown on the surface of MoS_2 nanosheets. The photocatalytic degradation of methylene blue (MB) in the aqueous suspension was employed to evaluate the visible light activity of as- prepared composite photocatalyst. The MB absorption peaks completely disappeared after 12 min with 99.33 % of degradation under visible light illumination at TiO_2 of 0.005 M. It was found that hydroxyl radical (•OH) played the important role for the degradation of MB under visible light illumination. The possible charge transfer mechanism was proposed.

Rare earth metal doped layered 2D molybdenum disulfide (MoS_2) nanostructures were synthesized by the hydrothermal method. XRD revealed the hexagonal formation MoS_2 nanostructures. XPS confirmed the presence of Ce ions in MoS_2 nanostructures which resulted significant peak shift. Morphological analysis of field emission scanning electron microscope (FESEM) and transmission electron microscope (TEM) images revealed the layered formation in MoS_2 nanostructures. The effect of Ce ions in MoS_2 nanostructures for photocatalytic activity was investigated and the photocatalytic degradation of methylene blue was evaluated under visible light irradiation. The methylene blue absorption peaks completely disappeared after 12 min with 99.39 % of degradation under visible light irradiation at Ce of 5 mM concentration. The introduction of cerium (Ce) ions into MoS_2 showed increased photocatalytic activity. Cerium ions effectively trapped the electrons from conduction band of MoS_2 which significantly controlled the recombination of charge carriers.

The hydroxyl radical (˙OH) played the important role for the degradation of methylene blue under visible light irradiation. The possible charge transfer mechanism has been proposed.

The above results clearly confirm that the well-defined 2D layered MoS_2 nanostructures was effective for the photocatalytic degradation of organic pollutant under visible light irradiation.

Chapter – 1

Introduction

1.1 Background

Nanoscience and nanotechnology are new approaches to research and development. These fields open up the possibility of understanding new phenomena and producing new properties that can be utilized at the micro and macroscale. Nanoscience is inherently multidisciplinary it transcends the conventional boundaries between physics, chemistry, biology, mathematics, information technology and engineering. Nanotechnology is engineering at the molecular level. It is the collective term for a range of technologies, techniques and processes that involve the manipulation of matter at the smallest scale. The prefix "nano" signifies one billionth. One nanometer is one billionth (= 0.000000001) of a meter, ten thousand times smaller than the width of a human hair. The main word in the hierarchy of terminology in nanotechnology and nanoscience related to size is 'nanoscale'. Nanoscale is a feature characterized by dimensions of the order of 100 nm or less. Nanostructure is any structure that is composed of discrete functional parts, either internally or at the surface, many of which have one or more dimensions of the order of 100 nm or less. Nanomaterial / nanocrystalline material is any form of a material that is composed of discrete functional parts, many of which have one or more dimensions less than 100 nm. Nanoscale is a magical point on the dimension scale. At these very small scales of length, energy and charge cannot be added continuously to matter but can only be added in small chunks. These chunks are called quanta, if they involve energy and are units of electronic charge if they involve charge. At this point of the size scale, the properties like conductivity, hardness or melting point meet the more exotic properties of the atomic and molecular world such as wave - particle duality and quantum effects. The familiar elements present in the periodic

table behave in unusual and surprising ways when rearranged into structures at the nanoscale. For example, titanium dioxide, a white pigment used in paints and sun screens, becomes transparent when reduced to particles of fewer than 100 nm while aluminum oxide, commonly used for teeth fillings, becomes explosive at this same scale. Nanostructured materials possess improved properties such as high strength, improved hardness and ductility in normally brittle materials, wear - resistance, erosion resistance, corrosion – resistance and higher chemical activity [1]. They are more formable than their conventional, commercially available counterparts. They have numerous commercial and technological applications in areas like analytical chemistry, drug delivery, bioencapsulation and in electronic, magnetic, optical and mechanical devices.

1.1.1 Environmental Remediation

The rapid pace of industrialization and the resultant by-products have affected the environment by producing hazardous wastes and poisonous gas fumes and smokes into the environment. Conventional technologies are used to treat all types of organic and toxic wastes by adsorption, biological oxidation, chemical oxidation and incineration. Supercritical water oxidation (SCWO) has been proposed as a technology capable of destroying a wide range of organic hazardous waste. It has been drawing attention due to its ability to destroy a large variety of high-risk wastes resulting from munitions demilitarization and complex industrial chemical processing. In parallel, the rapid growth in nanotechnology has gained a great deal of interest in the environmental applications of nanomaterials. Treatment of pollutants in water and air is a great challenge and nanomaterials are important for the environmental remediation. In the area of environmental remediation, nanomaterials offer potential for efficient removal of pollutants and biological contaminants. The nanomaterials are used for removal of contaminated chemicals (arsenic, iron, manganese, nitrate, heavy

metals, etc.), organic pollutants (aliphatic and aromatic hydrocarbons) and biological substances such as viruses, bacteria, parasites and antibiotics. Nanomaterials reveal better performance in environmental remediation than other conventional techniques used because of their high surface area (surface to volume ratio) and the associated high reactivity. Recent advances on the fabrication of novel nanoscale materials and processes for treatment of drinking water and industrial waste water contaminated by toxic metal ions, radionuclides, organic and inorganic solutes, bacteria and viruses and treatment of air are important.

1.2 Impacts of Nanotechnology

Nanotechnology literally means any technology at nanoscale. It is a new area which has generated excitement world - wide, by addressing the biggest challenges such as (1) clean, secure, affordable energy, (2) stronger, lighter, more durable materials, (3) low - cost filters to provide clean drinking water, (4) medical devices and drugs to detect and treat diseases more effectively with fewer side effects, (5) lighting that uses a fraction of the energy, (6) sensors to detect and identify harmful chemical or biological agents, etc. This emerging field also picturizes a new technology to protect, military and civilians from conventional, biological and chemical weapons. The implication of this technology is that it allows us to re-imagine our existing technologies with atomic precision and it provides a common platform to the technologist using atoms as a building block. Thus, it dissolves the boundaries between the existing technologies bringing them under a common umbrella. Moreover, nanotechnology takes the lead as it can provide us faster, more compact, less power consuming and greater storage capacity devices at cheaper rates. Nanotechnology holds promise in the quest for powerful computers and communications devices. The most fascinating applications are in the field of medical science. A programmable antibody, namely nano robot could be reprogrammed to selectively seek out and destroy the cancer

cells. A few applications of nanotechnology in various fields are mentioned below Drug delivery - Dendrimers (hyperbranched molecules) are a class of nanostructures which are designed to a variety of applications including treatment for cancer. Drug molecules can be attached to the branches of the dendrimers. Dendrimers can be used as coating agents to protect or deliver drugs to specific sites in the body or as time - release vehicles for biologically active agents. They are used as therapeutic agents in the treatment of cancer, namely Boron Neutron Capture Therapy (BNCT). In this process a stable isotope of boron, 10B along with non - radiative pharmaceutical is injected into the patient. This selectively migrates to the cancer cells. When the patient is irradiated by thermal neutrons, these neutrons react with the boron in the cancerous cells to generate alpha particles, which burns up the tumor cells [2]. Dendrimers also act as vectors in gene therapy. Vectors are carriers which carry genes through to cell membrane to the nucleus [3]. Apart from biomedical applications, they are also used to improve industrial processes. Their high surface area and solubility enable them to do the role of nanoscale catalyst [4]. Water filtration techniques / Waste water treatment – CNTs (carbon nanotubes) are used for purification based on filtration processes called size exclusion. The principle is that water is allowed to flow through the interior of the nano tube while the chemicals and the contaminants are filtered out. Additionally, CNTs show strong ability to adsorb chemicals and contaminants [5,6].

Dendrimers, metal - containing nanoparticles, zeolites and carbonaceous nanomaterials are employed for waste water treatment. Stoimenovet. al., [7] showed that MgO nanoparticles and magnesium (Mg) nanoparticles are very effective biocides against bacteria (Escherichia coli and Bacillus megaterium) and bacterial spores (Bacillus subtillus). Zinc oxide nanoparticles have been used to remove arsenic from water. Ag (I) and silver compounds have been used as antimicrobial compounds for coliform found in waste water [8]. Zeolites are effective sorbents and ion exchange media for metal ions. Dendrites serve as

a functional material for water purification. They can be used as high capacity and recyclable water soluble ligands for toxic metal ions, radio nuclide and inorganic anions [9]. Nanotechnology in space applications – Carbon nanotube (CNT) possess numerous application potentials in space [10]. It greatly reduces the mass of the space structures. CNTs are a perfect choice for space elevator cables, due to their exceptional properties, like light - weight and extra ordinary strength. CNTs are also used in the development of solar sails. These light weight devices use the pressure of sunlight's reflection to push the space craft forward. This will save a large amount of energy. Bio - nano robots implanted in the space suit of an astronaut will alert and save them from space - debris. Nanostructured metals can provide very hard coatings that are resistant to corrosion, useful for applications including aerospace components, such as landing gear and construction equipment such as drill bits and bulldozer blades. Electronics – CNTs now are mixed with polymers to make conducting composite materials for applications such as electromagnetic shielding in mobile phones and static electricity reduction in cars. Carbon nanotubes are already being used in the development of new flat screen displays. Zinc oxide nanoparticles and gallium nitride (GaN) are used for LEDs [11]. ZnO nanowires in LEDs may ultimately enable the development of large area lighting on flexible substrates [12]. Laser devices are fabricated from arrays of semiconductor nano - dots and nanowires [13]. CNTs and nanoparticles of vanadium, cobalt and manganese are used along with Lithium - ion batteries for enhanced performance [14]. Coatings containing nanoparticles are being used in some electrical products to protect the goods. Silver nanoparticles mixed in plastic resin are applied to major parts of the refrigerator in order to restrain the growth and increase of a wide variety of bacteria and to suppress odors [15]. Besides, using silver nanoparticles as coatings, a new technique, the so called 'silver wash' technology is designed to improve the washing of clothes [16].

1.3 Preparation of Nanomaterials

Nanomaterials can be prepared by several 'physical' and 'chemical' methods. In general, there are two general approaches to the synthesis of nanomaterials and the fabrication of nanostructures. Both the approaches play a very important role in nanotechnology. The methods for the synthesis of nanomaterials are broadly classified into two types:

(i) Top - down approach

(ii) Bottom - up approach.

(i) Top - down approach

Top - down approaches use larger (macroscopic) initial structures, which can be externally - controlled in the processing of nanostructures. Typical examples are lithographic techniques (etching through the mask), plasma arcing method, ball milling etc. By nature, top - down approaches aren't cheap and quick to manufacture. The biggest problem with top - down approach is the imperfection of the surface structure. This approach offers no control over the size and morphology of particles

(ii) Bottom - up appraoch

Bottom - up approaches include the miniaturization of materials components (upto atomic level) with further self - assembly process leading to the formation of nanostructures. During self - assembly the physical forces operating at nano scale are used to combine basic units into larger stable structures. Typical examples are quantum dot formation during epitaxial growth and formation of nanoparticles from colloidal dispersion. There are advantages and disadvantages in both approaches. But, the bottom - up approach promises a better chance to obtain nanostructures with less defects, more homogeneous chemical

composition and better short and long range ordering. This is because bottom - up approach is driven by the reduction of Gibb's free energy, so that nanostructures and nanomaterials produced are in a state closer to a thermodynamic equilibrium state. Bottom - up approach is considered as an efficient processing method for nano technological applications [17]. Bottom - up fabrication techniques includes gas phase methods, liquid phase methods (wet chemical methods), solid phase methods and biological methods. The principle of gas phase method is that gas phase precursors interact with the liquid or a solid phase material. The wet chemical synthesis, include sol - gel method, electro deposition, colloidal methods, hydrothermal method, etc. A few commonly used methods in the nanoparticle synthesis are as follows:

1.3.1 Plasma Arcing Method

This method is used extensively in the fabrication of CNTs. A typical plasma arching system consists of two electrodes inside a discharge chamber or at a low pressure inert atmosphere. When the electric arc passes between the two electrodes, the anode vaporizes and gets deposited on the cathode. In CNTs synthesis, carbon electrodes are used.

1.3.2 Ball Milling Method

The principle is that small hard balls are allowed to rotate inside a container and then it is made to fall on a solid with high force to crush the solid into nanoparticles. The balls are generally made up of hardened steel or tungsten carbide. These balls are put in a container along with powder of particles (50 μm) of a desired material. The container is closed with tight lids. When the container is rotating around the central axis, the material is forced to press against the walls. The milling balls impart energy on collision and produce smaller grain size of nanoparticle. Ball milling is also known as mechanical alloying or crushing.

1.3.3 Chemical Vapor Deposition (CVD)

CVD involves the formation of nanomaterials from the gas phase at elevated temperatures - usually onto a solid substrate or catalyst. The reactant particles are mixed with carrier gas and allowed to pass on through the hot solid substrate surface. When the reactant particles and substrate comes in contact, the heat energy initiates the chemical reactions and form nano film on the substrate surface. The byproducts of the reactions on the solid surface can be removed by washing.

1.3.4 Sol - gel Method

Sol - gel process consists in the chemical transformation of a liquid (the sol) into a gel state and with subsequent post - treatment and transition into solid oxide material. The sol is a colloidal solution made of solid particles few hundred nano meters in diameter, suspended in a liquid phase. The gel can be considered as a solid macromolecule immersed in a solvent. Synthesis of sol - gel in general involves hydrolysis of precursors, condensation followed by poly condensation to form particles, gelation and drying process.

1.3.5 Electro - Deposition Method

The principle of electro - deposition is to induce chemical reactions in an aqueous electrolyte solution with the help of applied voltage, e.g. this is the process of using electrical current to coat an electrically conductive object with a relatively thin layer of metal. This method is being exploited now to make complex 3D electrical interconnects in computer chips.

1.3.6 Hydrothermal Method

This is a wet chemical process employed to synthesize nanostructures. In this method, nanoparticles are synthesized in hot water / solvent in an autoclave under high pressure. The

reaction is carried out in sealed containers, Teflon - lined stainless steel autoclave. Under these conditions, autogenously pressure is self-developed within the container. The pressure within increases with the temperature as well as with the percentage fills of the vessel. This method allows generating high pressures even at temperatures below the critical point of water. In addition, it offers the advantage of significant solubility and reactivity of the inorganic compounds. And also, the chemical reactivity of insoluble solvents is enhanced.

1.3.7 Advantages of Hydrothermal Method

By hydrothermal method, it is possible to grow semiconducting quantum nanostructures as well as metal quantum nanostructures. It offers a greater control over the physical and chemical parameters; it is possible to finely control the growth and thus, obtain quantum nanostructures with small size, narrow size distribution and desired stoichiometry. The growth can be size selective by varying parameters such as temperature, precursor's type, surfactant type and their concentrations and the reaction time. Taking all these into consideration, this method is chosen to grow the 2-D layered MoS_2 nanostructures and nanocomposites in the present work. MoS_2 nanostructures has been deposited by many methods [18] including chemical bath deposition [19], atomic layer epitaxy [20], metal organic chemical vapor deposition (MOCVD) [21], pulsed laser deposition [22] and spray pyrolysis [23]. The hydrothermal method has several other advantages such as, low cost facilities, possibly to produce large amount of material, small size, high crystallinity and surface modifiable nanoparticles can be produced.

1.4 Semiconducting Nanomaterials

Semiconductor nanocrystals are termed as artificial atoms or quantum nanostructures [24] with their size in range of 2 - 8 nm in diameter. They are composed of approximately 100 - 1000 atoms. They are a special class of materials, composed of periodic groups of II -

VI, III - V, or IV - VI semiconductors. A major feature of these materials is the quantum confinement effect which leads to spatial enclosure of the charge carriers within the nanocrystals. The concept of quantum confinement by band gap engineering has led to the tremendous progress in the ability to synthesis quantum wells [25,26], quantum wires [27,28]and QDs [29] with high - efficiency, high - speed electronic and optoelectronic devices. This consequently paved way for miniaturization as well as high speed devices. The resolution of a television, or a monitor, improves with a reduction in the size of the pixel, or the phosphors. Nanocrystalline zinc selenide, zinc sulphide, cadmium sulphide and lead telluride are candidates for improving the resolution of monitors. Also, the flat - panel displays constructed out of nanomaterials [30] possess much higher brightness and contrast than the conventional ones owing to their enhanced electrical and magnetic properties.

Semiconductor quantum nanostructures are also currently being applied in biomedical imaging due to their unique fluorescence properties [31,32]. For instance, fluorescent quantum nanostructures can be conjugated with bioactive moieties (e.g., antibodies, receptor ligands) to target specific biologic events and cellular structures, such as labeling plastic cells [33,34] peroxisomes [35], DNA [36] and cell membrane receptors [37,38]. Nanocrystals possess several qualities that make them very attractive for fluorescent tagging: broad excitation spectrum, narrow emission spectrum, preciset unability of their emission peak, longer fluorescence lifetime than organic fluorophores and negligible photo bleaching. The semiconductor nanocrystals fascinate physicists, chemists and biologists due to their extra ordinary fluorescent properties [39,40]. Michalet et.al., [41] in their work exploited the semiconductor nanocrystal spectral properties to increase the resolution of fluorescence microscopy measurements down to the nanometer level.

1.5 Nanostructure Photocatalysts

Nanostructure photocatalysts are ultra-small semiconductor particles which are only a few nanometers in size. The interest in these small semiconductor particles originates from their unique photo physical and photo catalytic properties [45]. Nano sized particles, with diameters ranging between 1 nm and 10 nm, possess properties which fall into the region of transition between molecular and the bulk phases [45]. In the bulk material, the electron excited by light absorption finds a high density of states in the conduction band, where it can exist, with different kinetic energies [46]. In the case of nanoparticles however, the particle size is the same as or smaller than the size of the first excited state. Thus, the electron and hole generated upon illumination cannot fit into such a particle unless they assume a state of higher kinetic energy [47]. Hence, as the size of the semiconductor particle is reduced below a critical diameter, the spatial confinement of the charge carriers within a potential well [48], like a 'particle in a box' [49], causes them to behave quantum mechanically [50]. In solid state terminology, this means that the energy bands split into discrete electronic states (quantized levels) in the valence and conduction bands [47] and the nanoparticle behaves more and more like a giant atom [46]. Nanosized semiconductor particles which exhibit size - dependent optical and electronic properties are called quantized particles (Q - particles) or quantum dots [51].

Quantum - size (Q - size) effects occur when the size of the semiconductor particles become smaller than the Bohr radius of the first excitation state [49]. Size quantization in semiconductor particles leads to drastic changes in numerous important properties of the material.

Firstly, size quantization affects the electronic properties of the semiconductor particle, science the ultra-small crystallites composed of a few molecular units maintain their

discrete HOMOs (Highest Occupied Molecular Orbital) and LUMOs (Lowest Unoccupied Molecular Orbital) [48]. This in turn affects the charge carrier dynamics [52,53]. For example, for aqueous gold and silver colloids, spatial size confinement resulted in substantially slower electronic relaxation due to reduction of non-equilibrium electron transport and weaker electron - phonon coupling [53].

Secondly, in the quantum size regime, the physical and chemical properties, which are related to electronic properties, strongly depend on the size of the nanoparticles [47]. The band gap of the semiconductor becomes larger with decreasing particle size and is indicated by an absorption shift to shorter wavelengths [46]. The band edges, thus shift to yield larger redox potentials [54]. The levels of the valence band are moderately shifted to lower energies, while those of the conduction band are strongly shifted to higher energies [55]. Further, there is a change in electronic properties of size quantized nanoparticles which will have pronounced effect on the spectral properties of semiconductors [56].

One of the main advantages of quantum sized particles is that the band gap energy increases with decreasing particle size. As the size of a semiconductor particle falls below the critical radius, the charge carriers begin to behave quantum mechanically and this charge confinement leads to a series of discrete electronic states. As a result, there is an increase in the effective band gap and a shift of the band edges. Thus, by reducing the size of the semiconductor particles, it is possible to enhance the redox potential of the valence band holes and the conduction band electrons [57]. However, the solvent reorganization free energy for charge transfer to a substrate remains unchanged. The increasing driving force and the unchanged solvent reorganizational free energy are expected to lead to an increase in the rate constants for charge transfer at the surface [50]. Thus, the use of size - quantized semiconductor particles may result in increased photo activity for systems in which the rate -

limiting step is interfacial charge transfer. Hence, nano sized semiconductor particles possess enhanced photo redox chemistry, with reduction reactions, which might not otherwise proceed in bulk materials, being able to occur readily using sufficiently small particles [48,58]. Another factor which could be advantageous is the fact that a large fraction of atoms that are located at the surface of the nanoparticle [46]. Quantum sized particles thus have high surface area to volume ratios, which further enhances their catalytic activity [57]. One disadvantage of nano sized particles is the need for light with a shorter wavelength for photo catalyst activation. Thus, a smaller percentage of a polychromatic light source will be useful for photo catalysis.

Metal oxides, metal sulphides and other semiconductors are being studied as photo catalysts because of their suitable band structure which facilitates the charge carrier generation by light irradiation. TiO_2, ZnO, Fe_3O_4, etc., are some of the examples of metal oxide semiconductor photo catalysts. Among the various metal sulphide photo catalysts (MoS_2, ZnS, CdS, etc.), MoS_2, ZnS and CdS are important catalyst which are reported to possess excellent photo catalytic activity comparable to that of well-known photo catalyst TiO_2. Apart from ZnS, MoS_2 exhibits good photo catalytic activity. Moreover, MoS_2 is a visible light active photo catalyst.

1.6 Review of Literature

Molybdenum disulfide (MoS_2) is an important semiconductor with a band gap, Eg = ~1.8 eV and an absorption onset at 650 nm. It has promising applications in multiple technical fields including photochemical catalysis, gas sensor, detectors for laser and infrared, solar cells, nonlinear optical materials, various luminescence devices, optoelectronic devices and so on [42,43]. It is one of the most important candidates among III - VI compounds for detecting visible radiation [44]. MoS_2 nanoparticles / nanostructures have been extensively

studied by many research groups owing to their excellent optical properties at nanoscale. MoS_2 nanostructures possess excellent photo catalytic property. It has an appropriate conduction and valence band edge position to reduce and oxidize the H^+ and OH^- ions, respectively. In addition, MoS_2 nanostructures absorbs light especially in the visible region and has a good photo -stability under irradiation. Hence, they play an important role in the production of hydrogen. In recent years, many researchers exploited this property of MoS_2 nanostructures for the hydrogen production and waste water treatment for the degradation of organic pollutant.

O'Neill et al. have reported that the exfoliation has been achieved by using high-boiling organic solvents, such as *N*-methyl-2-pyrrolidone (NMP), or surfactant solutions [59]. Jawaid and co-workers have shown that the exfoliation yield in NMP is sensitive to trace water and dissolved oxygen [60]. Xu et al. have reported a strategy for exfoliating crystalline MoS_2 into a suspension of nanosheets with retention of the semiconducting phase [61]. Sheng et al. synthesized flower-like MoS_2 nanospheres by applying the hydrothermal method at 220 °C for 24 h and investigated their photocatalytic properties [62]. Zhou et al. synthesized porous MoS_2 by hydrothermal growth at 240 °C for 24 h and measured its visible-light photocatalytic activity [63]. Wang et al. synthesized monodispersed MoS_2 nanoparticles using different capping agents, such as hexadecyltrimethylammonium bromide (CTAB) and polyvinylpyrrolidone (PVP), by the hydrothermal method, and measured their ability to catalyze the reactivity of 4-methylphenol [64].

Citric acid has been used as a capping agent to obtain layered nanostructures. Citric acid possesses three carboxyl groups (–COO) and one hydroxyl group (–OH), which can serve as binding sites. It has been used in fabricating inorganic nanomaterials as a nontoxic and stable biological ligand for metal ions. Santillo et al. synthesized MoS_2 nanoparticles and

investigated the effect of citric acid on their formation [65]. Vattikuti et al. controlled the morphology of MoS_2 nanorods formed by the co-precipitation method, exploiting the crucial role played by citric acid in the formation of the nanorods [66].

From the above, it is to be noted that MoS_2 nanostructures / nanoparticles despite their toxic nature, they have been used in making all kinds of electronic devices and have unlimited applications such as in hydrogen production, solar cell, optoelectronics and as fluorescence probes. Surface passivation / modification can give rise to unique optical properties which can be exploited for many new applications. This motivated to work on the synthesis of 2-D layered MoS_2 nanostructures using citric acid as a capping ligand.

1.7 Problem statement and objectives

The above literatures highlight the versatility of 2-D layered MoS_2 nanostructures in the realization of visible light photocatalytic activity for degradation of organic dyes, hydrogen production, optoelectronic devices such as LEDs, in high efficiency solar cells (Coupling it with TiO_2). The literature presented here stresses the importance of nanocrystal capping, which is sometimes referred to as derivatization or as functionalization. The role of the capping molecules in the surface passivation process is manifold. On the other hand, the recombination of charge carrier is controlled by heterostructure photocatalyst composites and dopants, it provides efficient charge carrier separation between two semiconductors photocatalysts for photocatalytic degradation of organic dyes. Some of the advantages for the use of capping agents and nanocomposites are mentioned below:

- The capping molecules cover the nanoparticle surface, terminate the dangling bonds and thus prevent non - radiative recombination at surface sites. They act as surface passivating agents.

- They control the growth kinetics. The affinity of the precursors for the capping molecules determines the size of the nanoparticle. The lesser the affinity the larger is the size due to uncontrolled growth. The nanoparticle grows beyond the quantum regime.

- The capping molecules via sterical hindrance (e.g. long chain molecules) or by charge stabilization (ex. COO^- or $^+NH3$ groups at the surface) prevent the nanoparticle aggregation.

- The capping agents assist nanoparticles to be soluble in any solvent. Hence, water soluble nanoparticles can be easily synthesized for in vivo applications by using appropriate capping agents.

- Capping agents can significantly control and reduce the toxicity of the nanoparticles [67].

- They serve as site for chemical attachment of conjugating ligands that also bind to target molecules to thereby fluorescently label them with the quantum nanostructures.

- The nanocomposite photocatalysts possess more surface-active sites and this enhances the light absorption.

- The recombination of charge carrier is controllable using heterostructure nanocomposite through interfacial charge transfer between photocatalysts.

- The nanocomposites provide proper oxidation states and strong absorption ability towards organic dye molecules.

With proper surface passivation / modification / functionalization, 2-D layered MoS_2 nanostructures can be widely used for a variety of applications from opto-electronics to

biomedical applications. The motive behind the thesis is to synthesize 2-D layered MoS_2 nanostructures and nanocomposites using certain organic molecules as capping agent / passivating agent and evaluate them for photocatalytic activity. The objectives of this thesis are described as follows:

1. To synthesize pure and capped 2-D layered MoS_2 nanostructures and nanocomposites with different amount of capping agent and precursor, and to investigate the influence on capping agent and the concentration of composites precursor.
2. To investigate the functional properties of pure and capped 2-D layered MoS_2 nanostructures and nanocomposites.
3. To investigate the effect of reaction parameters on photocatalytic activity of pure and capped 2-D layered MoS_2 nanostructures and nanocomposites.
4. To investigate the photocatalytic activity of pure and capped 2-D layered MoS_2 nanostructures and nanocomposites.

References

1. Edelstein, A. S. and Cammarata, R. C., (eds)., 1996, IOP publishing, Bristol, London.
2. Hawthorne, M. F., Angew. Chem. Int. Edn., 1993, 32, 950 - 984.
3. Bielinska, A.U., Kukowska - Latallo, J.F., Johnson,J., Tomalia, D.A. and Baker, J.R., Nucleic Acids Res., 1996, 24, 2176 - 2182.

4. Tomalia, D. A. and Dvornic, P. R., Nature, 1994, 372, 617 - 618.

5. Pan, B. and Xing, B., Environmental Science & Technology., 2008, 42(24), 9005 - 9013.

6. Upadhyayula, V., Water Science & Technology., 2008, 58(1), 179 - 184.

7. Stoimenov, P. K., Klinger, R. L., Marchin G. L. and Klabunde, K. J., Langmuir, 2002, 18, 6679 - 6686.

8. Jain, P. and Pradeep, T., Biotech. Bioeng., 2005, 90, 59 - 63.

9. Ottaviani, M. F., Favuzza, P., Bigazzi, M., Turro, N. J., Jockusch, S. and Tomalia, D. A., Langmuir, 2000, 19, 7368 - 7372.

10. Bachmann, G., Bimberg, D, and Brunner, K, 2003, published by VDI technology centre, Dusseldorf, Germany.

11. Matsui, I., Journal of Chemical Engineering of Japan, 2005, 38(8), 535 - 546.

12. Burgess, D., Photonics Spectra., 2006, 135 - 136.

13. Simonite, T., NewScientist.com news service, 2006.

14. Endo, M., Hayashi, T., Kim, Y. A. and Muramatsu, H., Japanese Journal of Applied Physics., 2006, 45 (6A), 4883 - 4892.

15. Thomai Panagiotou and Robert J.Fishcer, Reactions and Separations, 2008, 33 - 39.

16. Mane, R. S. and Lokhande, C. D., Mater. Chem. Phys., 2000, 65, 1 - 31.

17. Liu, Q. and Mao, G. B., Surf. Rev. Lett., 2009, 16, 469 - 474.

18. Luo, Y., Han, M., Slater, D. A. and Osgood, R. M., J. Vac. Sci. Technol., 2000, 18, 438 - 449.

19. Yim, W. M. and Stofko, E. J., J. Electrochem. Soc., 1972, 119, 381 - 388.

20. Ullrich, B., Sakai, H. and Segawa, Y., Thin Solid Films, 385, 220 - 224.

21. Ma, Y. Y. and Bube, R. H., 1977, J. Electrochem. Soc., 124, pp. 1430 - 1435.

22. Alivisatos, A. P., Science, 1996, 271, 933 - 937.

23. Dingle, R., Wiegmann, W. and Henry, C. H., Physical Review Letters, 1974, 33, 827 - 830.

24. Miller, R. C., Kleinman, D. A., Tsang, W. T. and Gossard, A. C., Physical Review B, 1981, 24, 1134 – 1136.

25. Petroff, P. M., Gossard, A. C., Logan, R. A., Wiegmann, W., Appl. Phys. Lett. 1982, 41, 635 - 638.

26. Arakawa, Y. and Yariv, A., IEEE Journal of Quantum Electronics, 1986, 22, 1887 - 1899.

27. Asada, M., Miyamoto, Y. and Suematsu, Y., IEEE Journal of Quantum Electronic, 1986, 22, 1915 - 1921.

28. Ma, X., Wu, K., Wang, E. G., Chen, J., Deng, S. Z, and Xu, N. S., Applied Physics Letters, 1999, 75, 3105 - 3107.

29. Alivisatos, P., Nat. Biotechnol., 2004, 22, 47 - 52.

30. Chan, W .C. W., Maxwell, D. J., Gao, X., Bailey, R. E., Han, M. and Nie, S., Curr. Opin. Biotechnol., 2002, 13, 40 - 46.

31. Gao, X., Cui, Y., Levenson, R. M., Chung, L. W. and Nie, S., Nat. Biotechnol., 2004, 22, 969 - 976.

32. Wu, X., Liu, H., Liu, J., Haley, K. N., Treadway, J. A. and Larson, J. P., Nat. Botechnol., 2003, 21, 41 - 46.

33. Colton, H. M., Falls, J. G., Ni, H., Kwanyuen, P., Creech, D. and McNeil, E., Toxicol Sci., 2004, 80, 183 – 192.

34. Dubertret, B., Skourides, P., Norris, D. J., Noireaux, V., Brivanlou, A. H. and Libchaber, A., Science, 2002, 298, 1759 - 1762.

35. Beaurepaire, E., Buissette, V., Sauviat, M. P., Giaume, D., Lahlil, K., Mercuri, A., Nano Lett., 2004, 4, 2079 - 2083.

36. Lidke, D. S., Nagy, P., Heintzmann, R., Arndt - Jovin, D. J., Post, J. N. and Grecco, H. E., Nat. Biotechnol., 2004, 22, 198 -203.

37. Brus, L., Physical Chemistry of Solids., 1998, 59, 459 - 465.

38. Efros, A. L. and Rosen, M., Annual Review of Material Science., 2000, 30, 475 - 521.

39. Xavier Michalet, Fabien Pinaud, Thilo Lacoste, D., MaximeDahan, Marcel Bruchez, P., Paul Alivisatos, A. and Shimon Weiss, Single Mol. 2001, 2(4), 261 - 276.

40. Wang, Q., Xu, G. and Han, G., J. Solid State Chem., 2008, 178, 2680 - 2685.

41. Morales - Acevedo, A., Solar Energy Materials and Solar Cells, 2006, 90, 2213 - 2220.

42. Singh, V. and Chauhan, P., Chalcogenide Letters., 2009, 6, 421 - 426.

43. W. W., Kim, K. J. and Moon, S. J., Int. J. Hydrogen Energy, 2003, 29, 229 - 234.

44. Koca, A. and Sahin, M., J. Chem. Edu., 2003, 80, 1314 - 1315.

45. Buhler, N., Meier, K. and Reber, J. F., J. Phys. Chem., 1984, 88, 3261 - 3268.

46. Sathish, M., Viswanathan, B. and Viswanath, R. P., Int. J. Hydrogen Energy, 2006, 31, 891 - 898.

47. Sant, P. A. and Kamat, P. V., Phys. Chem. Chem. Phy., 2002, 4, 198 - 203.

48. Kakuta, N., Park, K. H., Finlayson, M. F., Ueno, A., Bard, A. J., Campion, A., Fox, M. A., Webber, S. E. and White, J. M., J. Phys. Chem., 1985, 89, 732 - 734.

49. Chen, Y. F. and Rosenzweig, Z., Anal. Chem., 2002, 74, 5132 - 5138.

50. Tang, C. R., Su, Z. H., Lin, B. G., Huang, H. W., Zeng, Y. L., Li, S., Huang, H., Wang, Y. J., Li, C. X., Shen, G. L. and Yu, R. Q., Analytica. Chimica. Acta., 2010, 678, 203 - 207.

51. Lai, S., Chang, X., Mao, J., Zhai, Y., Lian, N. and Zheng, H., Annali di Chimica., 2007, 97, 109 - 121.

52. Dan Li, Zheng - Yu Yan. and Wei - Qing Cheng., Spectrochimica Acta Part A, 2008, 71, 1204 – 1211.

53. Sreekumari, N. P., Radhakrishnan, T., Revaprasad, N., Gaberiel, A. and O' Brien, P., Polyhedron, 2003, 22, 3129 - 3135.

54. Han, J., Su, H., Zhang, D., Chen, J. and Chen, Z., J. Mater. Chem., 2009, 19, 8741 - 8746.

55. Han, J., Su, H., Song, F., Zhang, D. and Chen, Z., Nanoscale, 2010, 2, 2203 - 2208.

56. Zheng, Y. M., Gao, X. F. and Jiang, L., Soft Matter., 2007, 3, 178 - 182.

57. Vukusic, P., Sambles, R., Lawrence, C. and Wakely, G., Applied Optics., 2001, 40, 1116 - 1125.

58. Matthew, P., Genovese, I., Lightcap, V. and Prashant, V., ACS Nano., 2012, 6, 865 - 872.

59. A. O'Neill, U. Khan and J. N. Coleman, Chem. Mater., 2012, 24, 2414 - 2421.

60. A. Jawaid, D. Nepal, K. Park, M. Jespersen, A. Qualley, P. Mirau, F. Drummy and R. Vaia, Chem. Mater., 2016, 28, 337 - 348.

61. X. Danyun, Z. Yuanzhi, L. Jiapeng, L. Yang, P. Wenchao, Z. Guoliang, Z. Fengbao and F. Xiaobin, Nanotechnology, 2016, 27, 1 - 7.

62. 14 S. Beibei, L. Jinsong, L. Ziquan, W. Menghui, Z. Kongjun, Q. Jinhao and W. Jing, Mater. Lett., 2015, 144, 153 – 156.

63. Z. Zhihua, L. Yuelai, Z. Pingan. A. Eric, S. Muhammad, L. Handong, W. Jiang and W. Zhiming, Mater. Lett., 2014, 131, 122 – 124.

64. W. Weiyan, Z. Kun, Q. Zhiqiang, L. Lu, L. Pengli amd Y. Yunquan, Ind. Eng. Chem. Res., 2014, 53, 10301 – 10309.

65. G. Santillo, F. A. Deorsola, S. Bensaid, N. Russo and D. Fino, Chem. Eng. J., 2012, 207 - 208, 322 – 328.

66. S. V. Prabhakar Vattikuti, C. Byon, Ch. Venkata Reddy and J. Shim, Appl. Phys. A., 2015, 119, 813 – 823.

67. Ma, N., Yang, J., Stewart, K. M. and Kelly S.O, Langmuir, 2007, 23, 12784 - 12787.

Chapter –2

Hydrothermal growth of ligand-assisted monodispersed MoS_2 layered nanostructures for the realization of ultrafast degradation of an organic pollutant

2.1 Background

Nanostructured materials [1, 2] form a new category of materials which bridge the gap between the bulk and the molecular levels. The boundaries between bulk and nanoparticle are depends upon the composition and crystal structure of the solid. The dependence of size arises from (1) change of surface - to - volume ratio with size and (2) quantum confinement effects. Quantum confinement [3,4] modifies the density of states (DOS) near the band - edges. This leads to the blue shift of band - gap energy, when the particle size falls below a particular value (depends on the semiconductor). Due to the high surface- to - volume ratio of the nanoparticles, the electronic quantum states associated with the surface have significant effect on the optical properties. The surface states arise from the unsatisfied bonds at the reconstructed surfaces and may be affected by the non - stoichiometry and voids. The energies of these surface states lie in the band gap of the quantum nanostructure [5]. These surface states can act as temporary 'traps' for electrons, holes or excitons, quenching radiative recombination and reducing the quantum yields. These surface states can be eliminated by surface passivation. The capping molecules form a layer on the nanoparticle and restrict the growth of the nanoparticles which yield size confinement and narrow size distribution. In addition, they eliminate the surface traps and therefore, some of the non - radiative relaxation pathways [6]. These molecules via steric hindrance or by charge stabilization prevent the aggregation of nanoparticles which provides good dispersity

[7]. They are tailored to meet specific application based parameters such as chemical reactivity and water - solubility. Using appropriate capping agent, smaller nanoparticles with excellent optical properties can be possible, so that these molecules would facilitate integration of MoS_2 nanoparticles into chemical systems, polymeric matrices, QLEDs, photo-voltaics and other applications [8,9]. For this reason, binding of organic capping agents, polymers, inorganic substances or biomaterials to nanoparticles [10] is essential. Hence, this area of nanoparticle research is opening up new challenges and is progressively under research. This process is carried out by depositing an organic or inorganic capping layer over the nanoparticle surface.

A new two-dimensional (2D) material, molybdenum disulfide (MoS_2), with a direct band gap of 1.9 eV, has attracted immense interest in various applications. For example, MoS_2 has been utilized for applications such as lithium ion batteries, dye-sensitized solar cells, gas sensors, photodetectors, memory devices, catalysts for hydrogen evolution and photocatalysts for dye degradation. Layered structures of MoS_2 have been extensively investigated as photocatalysts for decomposing organic compounds. The layered structure of MoS_2 consists of S–Mo–S units sandwiched in a graphite-like manner by relatively weak van der Waals forces and the crystal structure as shown in Fig 2.1. [11, 12]. The size of its direct band gap makes it a visible-active photocatalyst [13, 14]. Charge carriers are generated in the valence band and the conduction band of MoS_2 under light irradiation. The recombination rate of the photo-generated electron–hole pair is problematically high; however, recombination can be effectively suppressed by the formation of specific layered nanostructures [15-19].

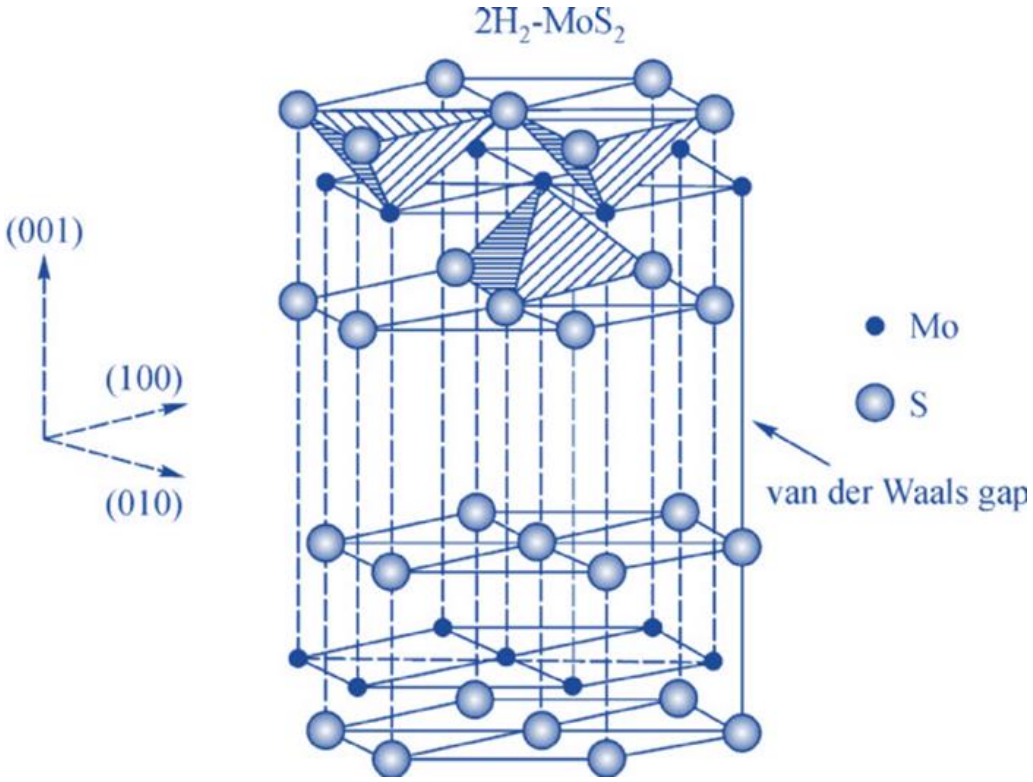

Figure 2.1 Crystal structure of MoS_2

In the research, well defined layered MoS_2 nanostructures were successfully synthesized by the hydrothermal method, using citric acid as a capping ligand. The effect of the concentration of citric acid on the formation of layered MoS_2 was investigated. The photocatalytic activity of the prepared samples was assessed by measuring the decomposition rate of methylene blue (MB) in aqueous solution under visible-light irradiation. The effect of pH on the MB degradation was also studied. Finally, a possible formation mechanism of the nanostructures was proposed.

2.2 Experimental procedure

2.2.1 Hydrothermal growth of layered MoS_2 nanostructures

In this synthesis, 0.04 M of sodium molybdate dihydrate was dissolved in 50 mL of deionized water and allowed to stir until complete dissolution of the compound. 0.08 M of thioacetamide was added and the reaction was allowed to stir for 3 h. Finally, the mixture was

transferred into a Teflon-lined autoclave and maintained at 180 °C for 24 h. The obtained precipitate was separated by centrifugation and washed several times with deionized water and ethanol. The obtained product was dried at 80 °C for 10 h. The samples of this product were denoted CA0. For the synthesis of citric acid-capped nanostructures, citric acid at four different concentrations, namely, 0.01, 0.02, 0.04 and 0.05 M, was added to the mixture of 0.04 M sodium molybdate dehydrate and 0.08 M thioacetamide under vigorous stirring, and the remaining procedure was followed as described for CA0. These samples were denoted CA1 (0.01 M), CA2 (0.02 M), CA3 (0.04 M) and CA4 (0.05 M).

2.2.2 Photocatalytic dye degradation

The photocatalytic activity of the synthesized MoS_2 samples was evaluated by examining the photo-assisted degradation of MB, as a model dye, at room temperature under a xenon light source as a source of visible-light irradiation. The procedure was adopted from a previous report, with the following modification [20]. In a typical reaction, the amount of dye was fixed at 5 mg and the solution pH was controlled at the desired level by the addition of NaOH. At regular time intervals, 3 mL of the suspension was collected, centrifuged, and analyzed by a UV–vis spectrometer. The degradation of MB was quantified from the decrease in the intensity of the associated characteristic absorption band at 664 nm. The photodegradation percentage of MB was calculated using the following equation [20]:

$$D(\%) = \frac{C_0 - C_t}{C_0} \times 100, \qquad (1)$$

2.2.3 Characterization techniques

The structure of the product was characterized by a Rigaku X-ray diffractometer (XRD) (RINT ULTIMA III, Japan) with CuKα radiation and a step interval of 0.02° s^{-1}.

Figure 2.2 Rigaku X-ray diffractometer at Center for Nano device Fabrication and Analysis, Shizuoka University

UV–vis spectroscopy analyses were performed by a Jasco UV-Vis (V-670) spectrophotometer (Japan).

Figure 2.3 Jasco UV-Vis (V-670) UV visible absorptions spectrophotometer at Center for Nano device Fabrication and Analysis, Shizuoka University

X-ray photoelectron spectroscopy (XPS) was performed by a XPS (AXIS ULTRA DLD) (Japan).

Figure 2.4 XPS (AXIS ULTRA DLD) X-ray photoelectron spectroscopy at Center for Nano device Fabrication and Analysis, Shizuoka University

FESEM of the product was measured by a field emission scanning electron microscope (FESEM) (JEOL JSM 7001F microscope) at an accelerating voltage of 15 kV.

Figure 2.5 JEOL - JSM 7001F field emission scanning electron microscope at Center for Nano device Fabrication and Analysis, Shizuoka University

TEM of the product was measured transmission electron microscope (TEM) (JEOL JEM 2100F microscope) at an accelerating voltage of 200 kV.

Figure 2.6 JEOL - JEM 2100F transmission electron microscope at Center for Nano device Fabrication and Analysis, Shizuoka University

Degradation of the organic pollutant was evaluated with a xenon light source of MAX-303, Asahi Spectra. Xenon lamp creates strong stable light and its spectrum is very close to the sunlight.

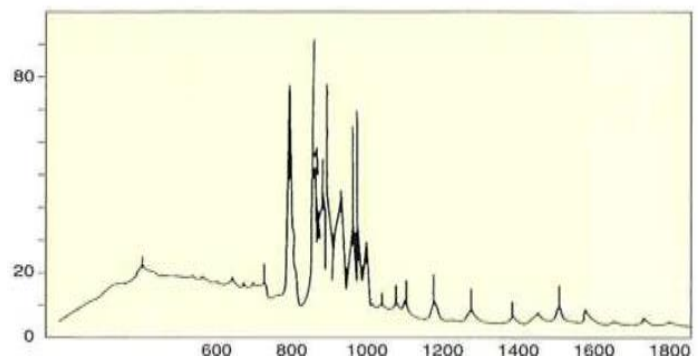

Xenon light spectral irradiance

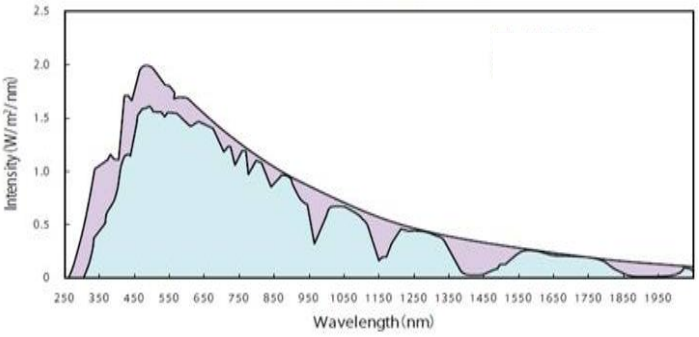

Sun light spectral irradiance

Figure 2.7 MAX-303, Xenon light, Asahi Spectra at Prof. Yasuhiro Hayakawa laboratory, Shizuoka University

2.3 Results and Discussion

The XRD patterns of the pure (CA0) and citric acid-capped MoS_2 structures (CA1, CA2, CA3, and CA4) are shown in Figure 2.8 (a). The pure sample exhibited a poorly crystalline structure. In contrast, the citric acid-capped MoS_2 possessed crystal planes with clear peak positions, closely matching the standard diffraction pattern of hexagonal MoS_2 (JCPDS card no. 24-0513). These results suggested that the citric acid played a crucial role in the formation of the hexagonal crystal structure [21]. We attribute this to the ability of the capping agent to retard the process of nucleation and particle growth during the reaction. Figure 2.8 (b) shows the UV-vis diffuse reflectance spectroscopy of as-prepared MoS_2 layered nanosheets. It was found that the samples exhibited the strong light absorption in the wavelength range of 600 - 800 nm [22]. As shown in Figure 2.8 (c), the bandgap of the samples is 1.96 eV. The obtained bandgap data indicated that the MoS_2 shows a blue shift bandgap of 1.96 eV compared to bulk MoS_2 of 1.23 eV because of its quantum confinement near the fermi level [23, 24].

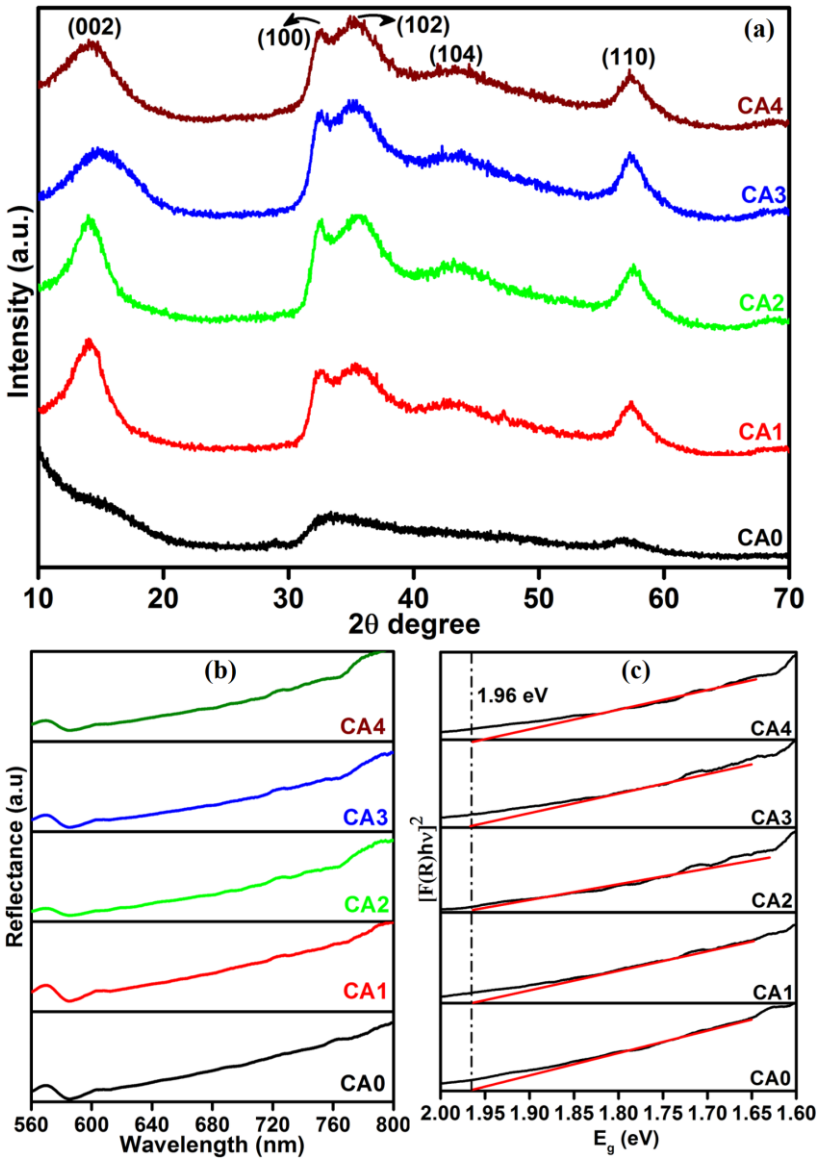

Figure 2.8 (a) XRD, (b) UV-vis DRS reflectance spectra and (c) band gap plot of MoS_2 layered nanosheets.

The core-level electronic states of the MoS_2 nanostructures were investigated by XPS analysis, as shown in Figures 2.9 (a) and (b). Figure 2.9 (a) shows the high-resolution XPS spectra of the Mo 3d state, with two symmetric peaks. The peaks at 228 and 231.20 eV correspond to Mo $3d_{5/2}$ and Mo $3d_{3/2}$, respectively. Their presence implies that the Mo was in the Mo^{4+} state. The separation energy between Mo $3d_{5/2}$ and Mo $3d_{3/2}$ was 3.2 eV, a typical value for this element [25]. When the concentration of citric acid was increased from 0.04 M

(CA3) to 0.05 M (CA4), the peak positions of samples were shifted from 228 to 228.30 eV for Mo $3d_{5/2}$ and 231.20 to 231.50 eV for Mo $3d_{3/2}$ state, respectively. This slight shift is attributed to the interaction of Mo and citric acid. Figure 2.9 (b) shows the high-resolution XPS spectra of the S 2p state. The S 2p peaks of CA1 can be deconvoluted into two peaks at 161 and 161.90 eV, which correspond to S $2p_{3/2}$ and S $2p_{1/2}$, respectively. These peaks exhibited a similar shift to that of the Mo 3d peaks between the CA3 and CA4 samples, i.e., from 161 to 161.20 eV and from 161.90 to 162.10 eV for S $2p_{3/2}$ and S $2p_{1/2}$, respectively, with the increase in the concentration of citric acid. The XPS core-level spectra of the Mo and S states thus provided evidence of a significant interaction of citric acid with MoS_2.

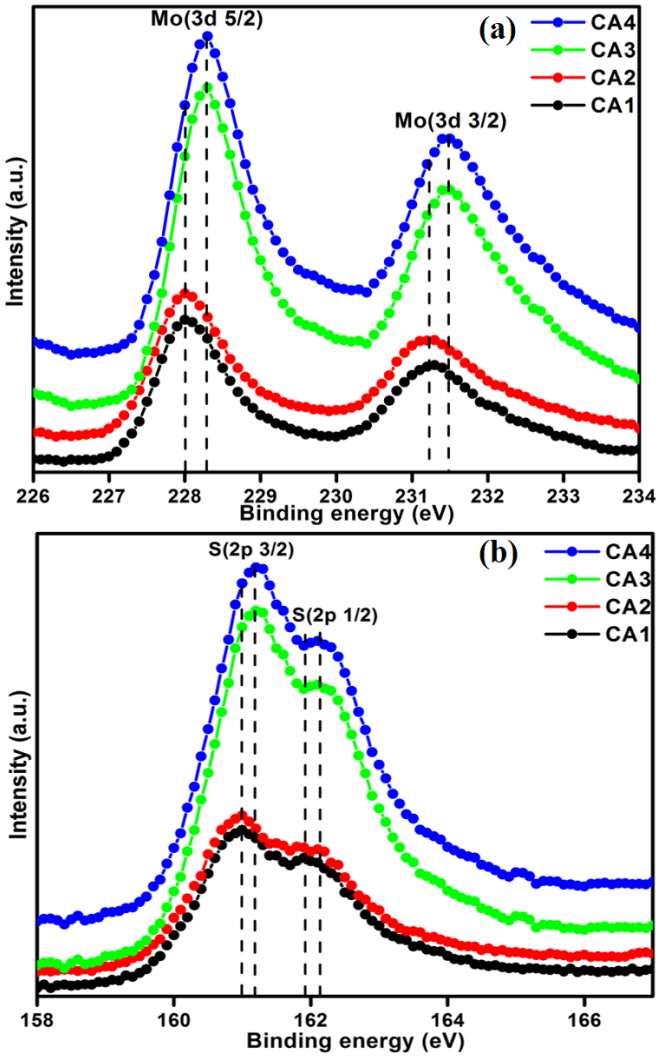

Figure 2.9 XPS spectra of Mo 3d state (a) and S 2p state (b) of samples.

The surface morphology and microstructures of the samples were characterized by FESEM, TEM and HRTEM, as shown in Figures 2.10–2.14. Figures 2.10 (a) and (b, c) show the morphology of the MoS_2 microspheres of CA0. It can be seen that these MoS_2 microspheres were composed of sheet-like subunits. In contrast, the FESEM images of sample CA1 indicated the formation of nanosheets (Figure 2.11 (b)). This change in morphology occurred in the presence of citric acid. When the concentration of citric acid was increased to 0.02 (CA2) and 0.04 M (CA3), similar layered nanosheets were observed, as shown in Figures 2.12 (b) and 2.13 (b). With the further increase in the concentration of citric acid to 0.05 M (CA4), the MoS_2 nanosheets became slightly agglomerated, as shown in Figure 2.14 (b). These results indicate that citric acid played a crucial role in determining the morphology of MoS_2. The citric acid effectively directed the MoS_2 nanostructures toward the formation of layers. The TEM and HRTEM images showed the presence of these layered MoS_2 nanostructures. The agglomeration of the MoS_2 nanosheets was attributed to the increased ionic strength with higher concentrations of citric acid, which facilitated interaction among the nanosheets [26]. The capping agent reduced the number of dangling bonds (a form of surface defect) present on the surface of the nanosheets, thus lowering their surface energy and stabilizing their growth. HRTEM analysis confirmed a lattice spacing of 0.6 nm, corresponding to the (002) plane of the MoS_2 nanosheets, as shown in Figure 2.13 (c).

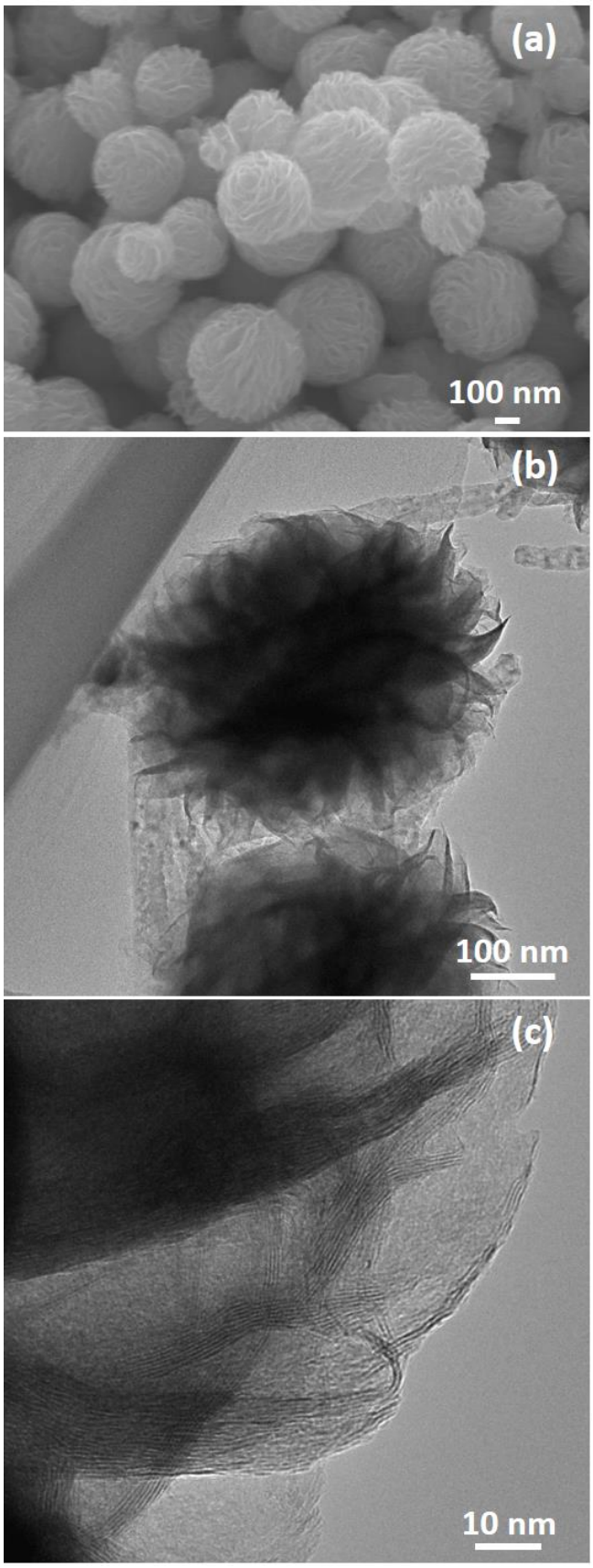

Figure 2.10. FESEM, TEM and HRTEM images of sample CA0 (a, b and c).

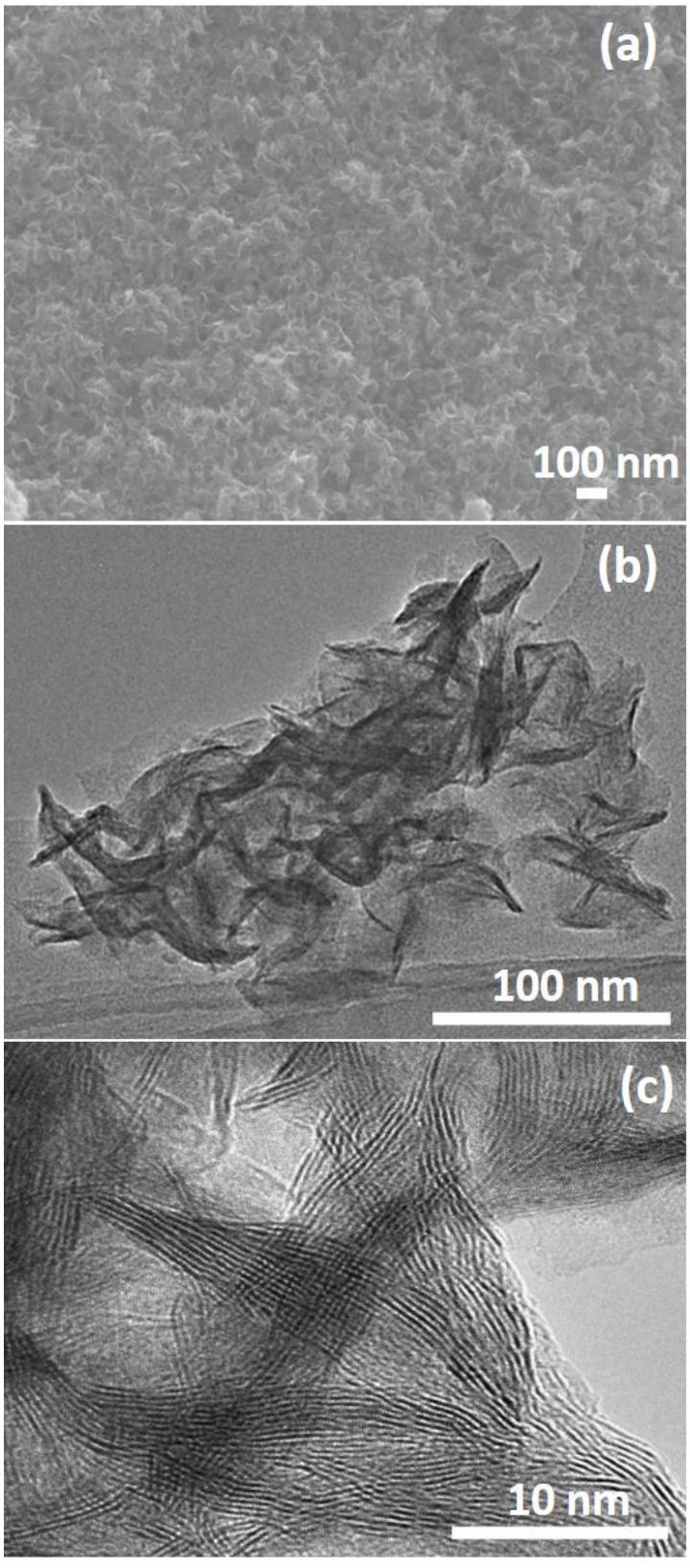

Figure 2.11. FESEM, TEM and HRTEM images of sample CA1 (a, b and c).

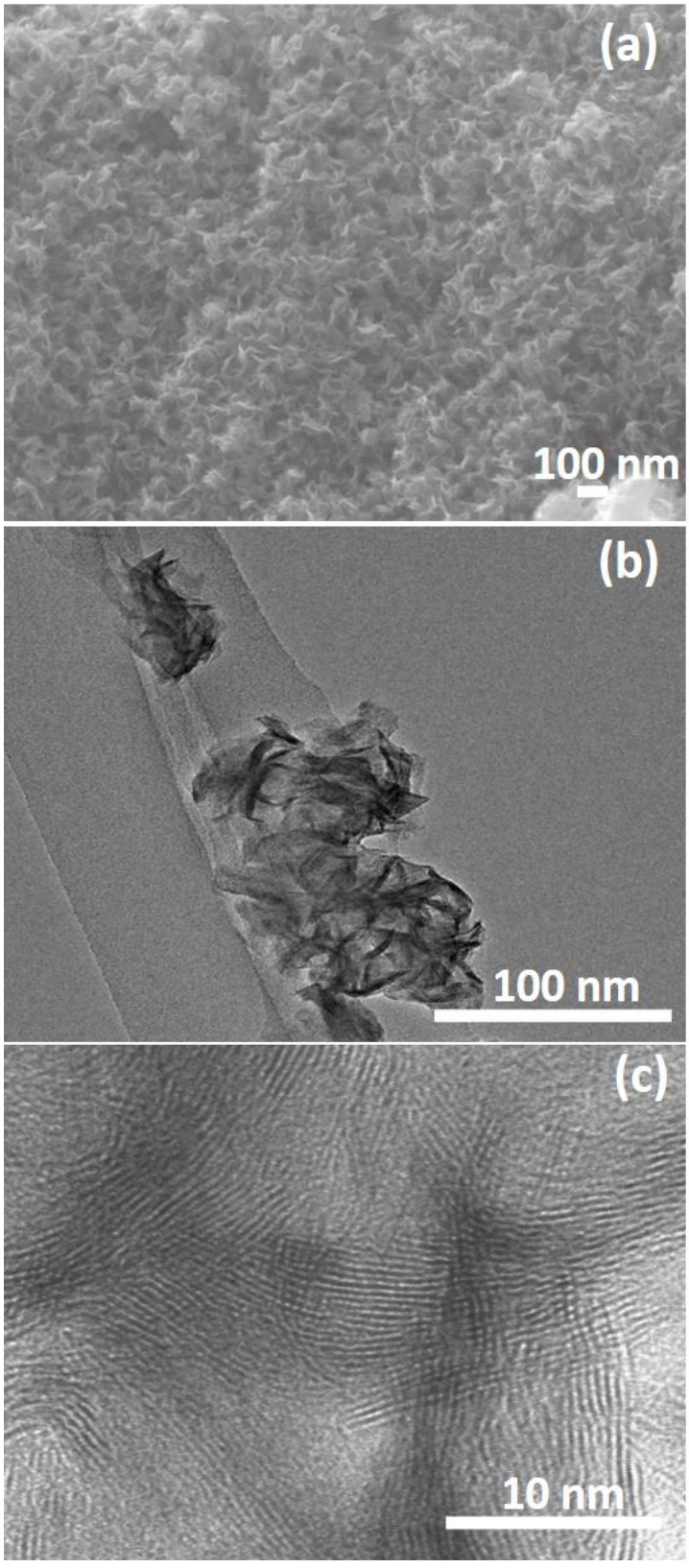

Figure 2.12. FESEM, TEM and HRTEM images of sample CA2 (a, b and c).

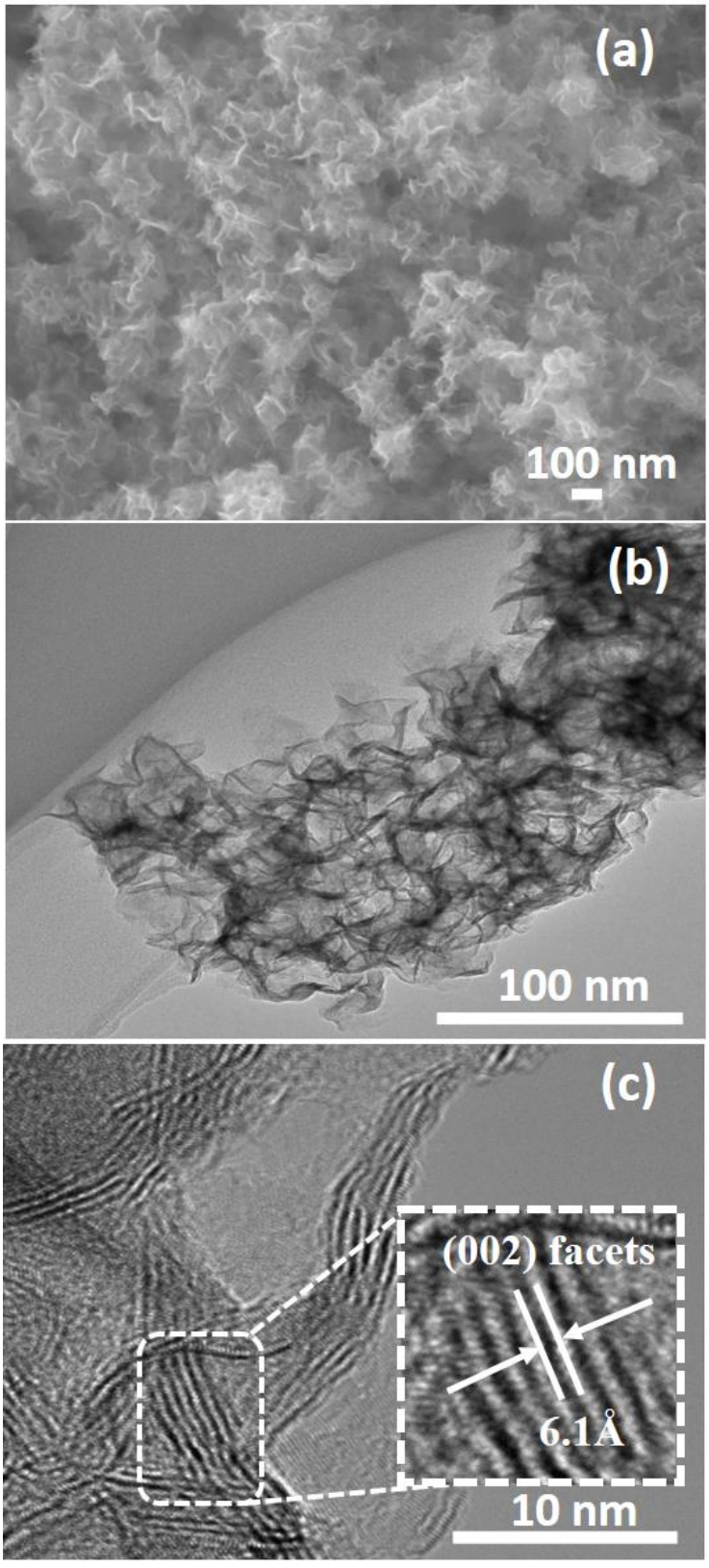

Figure 2.13. FESEM, TEM and HRTEM images of sample CA3 (a, b and c).

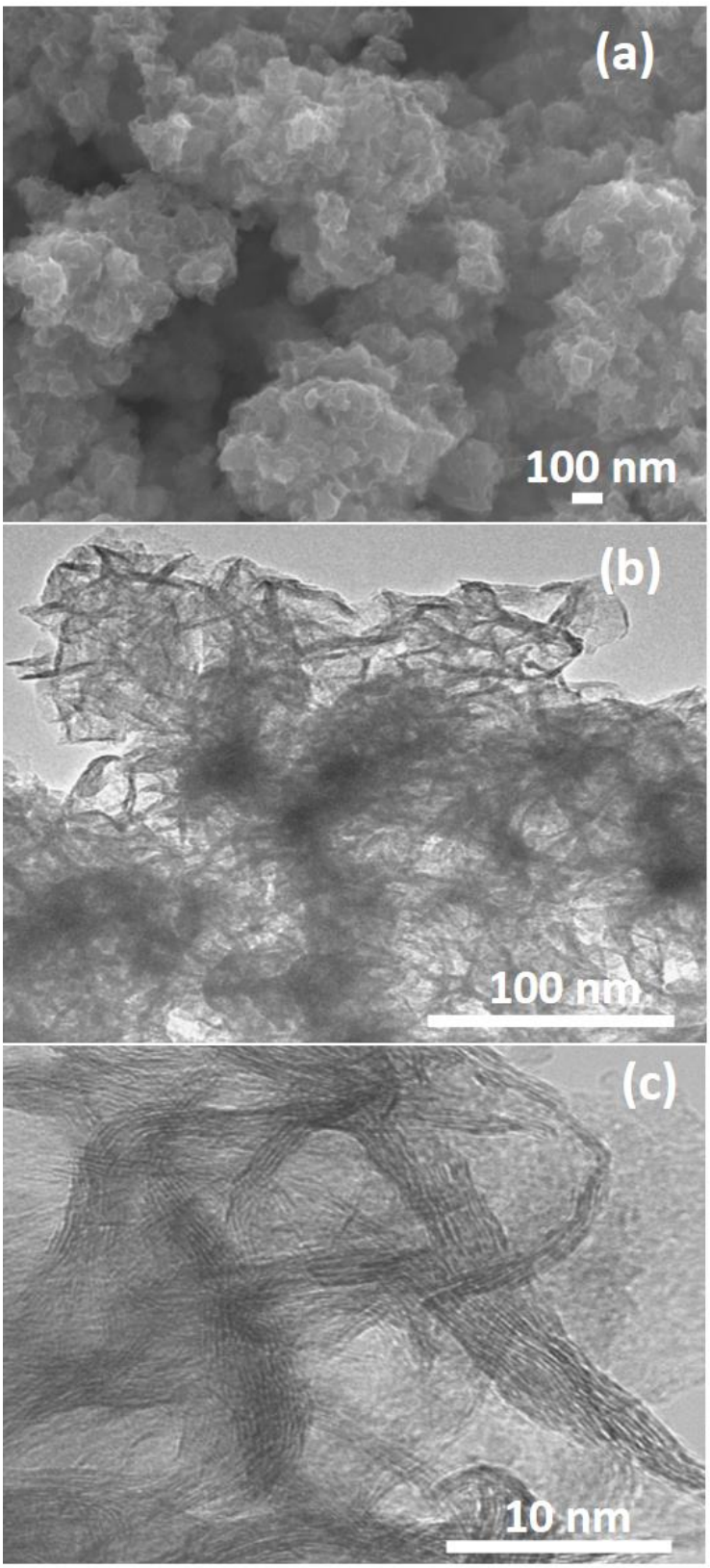

Figure 2.14. FESEM, TEM and HRTEM images of sample CA4 (a, b and c).

Based on the above structural and morphological analysis, we propose the following formation mechanism, as shown in Figure 2.15. It has been established previously that citric acid is an effective capping agent to adjust the relative activity of the cations and retard the grain growth of MoS_2. Citric acid can be hydrolyzed into $[C_6O_7H_5]^{3-}$ and H^+. The $[C_6O_7H_5]^{3-}$ ions can chelate Mo^{4+} to form $[C_6O_7H_5]^{3-}$ $[Mo^{4+}]$ complexes [27, 28]. In these complexes, hydrogen bonds can be formed between the carboxyl groups of citric acid and the hydroxyl ions, and also between two hydroxyl ions. The self-assembly growth of MoS_2 microspheres is controlled by the interaction between the $[C_6O_7H_5]^{3-}$ $[Mo^{4+}]$ complexes and the hydrogen bonds, directing the formation of layered nanosheets [29, 30]. The citric acid also has the effect of reducing the Mo valence state from Mo^{6+} to Mo^{4+}, in good agreement with the XPS data [31, 32].

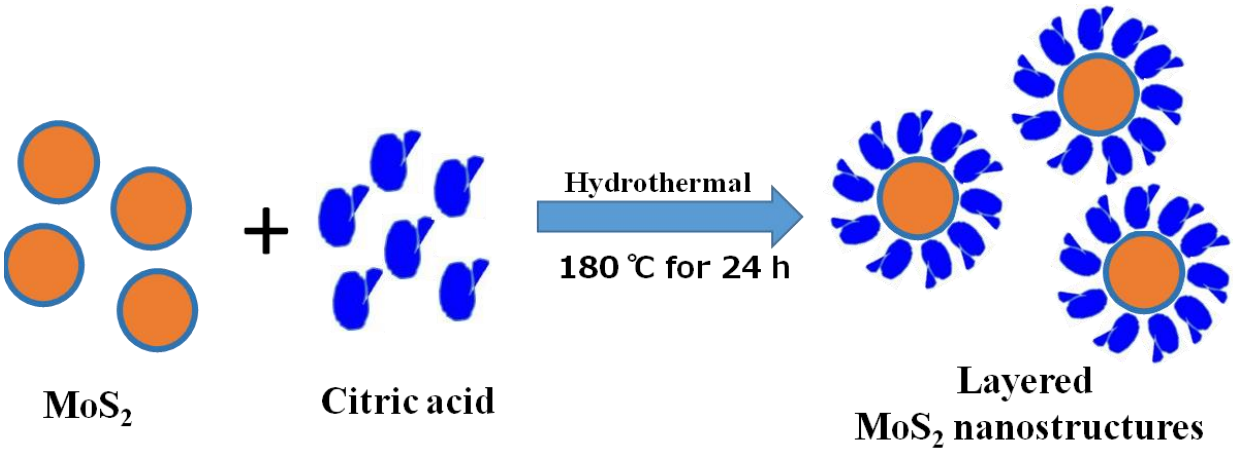

Figure 2.15. Schematic reaction mechanism of layered MoS_2 nanosheets.

2.3.1 Photocatalytic activity

The photocatalytic activity of the MoS_2 nanostructures was investigated via their ability to degrade MB as a model pollutant. Figure 2.16 (a) shows the time-dependent UV absorption spectrum of the pure (CA0) MoS_2 catalyst under visible-light irradiation. The MB

was completely decomposed after an irradiation time of 48 min. The time-dependent UV absorption spectra of MB under visible-light irradiation for samples CA1, CA2, CA3 and CA4 are shown in Figures 2.16 (b), (c), (d) and (e), respectively. For CA1, it can be seen that the maximum absorbance peak at 664 nm gradually decreased in intensity with the increase in irradiation time, and completely disappeared after 48 min. For CA2, CA3 and CA4, the total irradiation times required for the complete degradation of the MB absorbance peak were 40, 24 and 44 min, respectively. Figure 2.16 (f) shows the percentage of MB degradation achieved by the samples TiO_2 (P25), CA0, CA1, CA2, CA3 and CA4, which were 56.89 %, 99.17 %, 99.30 %, 98.82 %, 99.37 % and 98.89 %, respectively. Therefore, the citric acid-capped MoS_2 nanostructures showed enhanced photocatalytic activity compared with pure MoS_2 and commercial TiO_2 (P25) under visible-light irradiation. Among all the synthesized samples, CA3 showed the greatest photocatalytic activity and achieved complete degradation of MB within 24 min of irradiation.

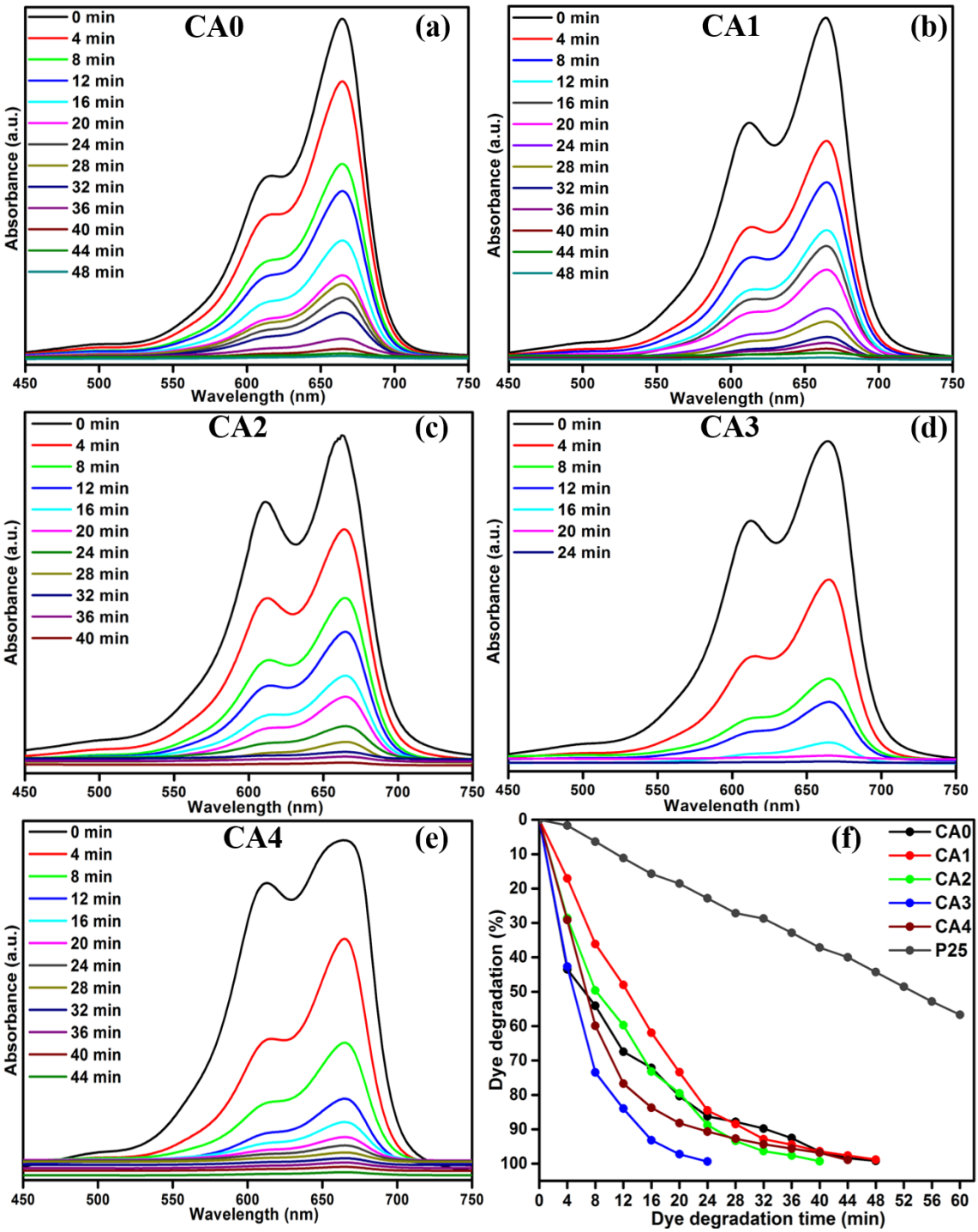

Figure 2.16. UV absorbance spectra of MB samples CA0 (a), CA1 (b), CA2 (c), CA3 (d) and CA4 (e), (f) Time (min) vs dye degradation (%).

The photocatalytic decomposition of MB by sample CA3 was studied at varying pH values of the suspension, as shown in Figures 2.17 (a)–(g). The greatest photocatalytic activity was attained at pH 12 and 14, where 96 % of the dye was degraded in 2 min. Thus, MB degradation was more active in alkaline medium. Figure 2.17 (h) shows the percentage of MB degraded as a function of pH. The degradation percentages achieved in 2 min at pH 1, 3, 6, 8 and 10 were 41, 49, 14, 78 and 90 %, respectively. The variation of photocatalytic efficiency with pH is generally an effect of the surface charge of the catalyst and the charge on the dye molecules [33]. At lower pH values, the surface of the catalyst was positively charged and the degradation efficiency was low. In contrast, higher pH values can instigate the formation of a large concentration of hydroxyl ions (OH^-), which can react with holes to form hydroxyl radicals (•OH), resulting in a rapid increase in the degradation efficiency. Whereas, the same sample exhibited the higher degradation percentage of 99.37 % in 24 min under MB dye degradation. It is clear that the MB degradation of CA3 photocatalyst shows the best enhancement in the photodecomposition of MB under visible light irradiation.

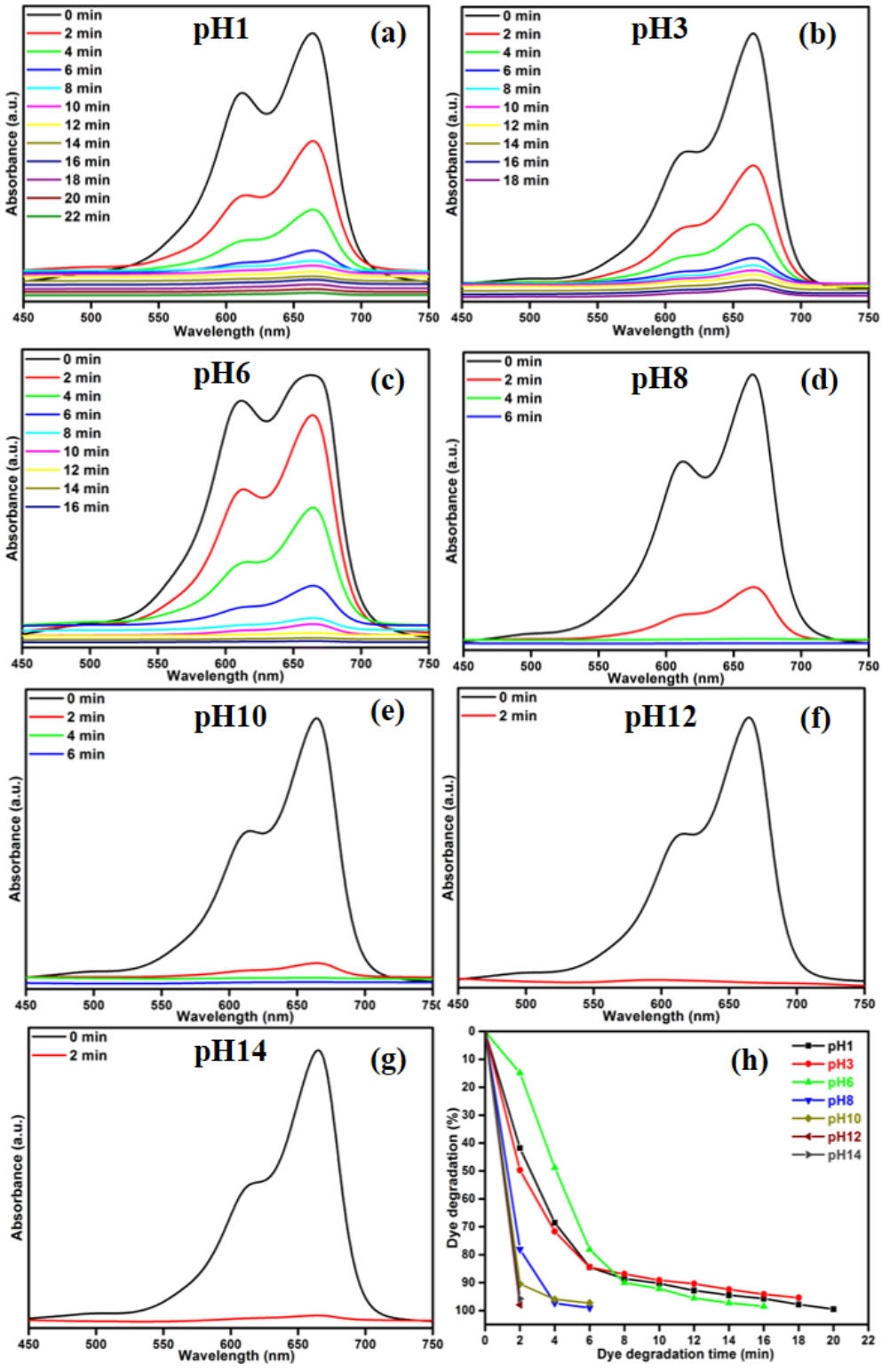

Figure 2.17. Effect of pH on degradation efficiency, (a)–(g) UV absorbance spectra of MB samples and (h) Time (min) vs dye degradation (%).

To elucidate the photocatalytic mechanism of MB degradation over MoS_2, the scavengers are used. The obtained results are shown in Figure 2.18 (a). Hydroxyl radical ($^{\bullet}OH$) and superoxide anions ($O_2^{-\bullet}$) are the possible active species in the photodegradation of organic pollutants. The scavengers are known to react with reactive oxygen species preferentially over the organic dye. The nitrogen (N_2) and disodium ethylenediaminetetraacetate (EDTA-2Na) [22, 34] were used as an electron acceptor and hole scavenger. When EDTA was added into the solution as $^{\bullet}OH$ radical scavenger, the degradation of MB slowed down slightly as shown in Figure. 2.18 (a). This conforms that the $^{\bullet}OH$ radical plays a minor role in the photocatalysis process. In order to further determine the degradation mechanism, another experiment was performed under N_2 atmosphere. A high purity N_2 gas was continuously purged throughout the reaction process under ambient condition, which eliminates the dissolved oxygen content from the reaction solution and thereby prevents the formation of $O_2^{-\bullet}$ [35, 36]. Therefore, it is clearly illustrated that $O_2^{-\bullet}$ radical from the reaction of photogenerated electron plays an important role, while the photogenerated h^+ also contributed in certain extent for the degradation of MB in the MoS_2 photocatalyst process.

Figure 2.18 (b) shows the reusability of CA3 photocatalyst for the degradation of MB examined over three cycles under visible light irradiation. After the photocatalysis experiments, the catalyst was separated from the reaction mixture by centrifugation and the concentration of the dye solution was adjusted to its initial value. Photocatalysts were reused for three cycles and the obtained degradation values were 93.35, 92.18 and 90.72 % for first, second and third cycles, respectively. The photocatalytic efficiency of the MoS_2 did not declined significantly, which suggests that the catalyst had good stability and sustainability.

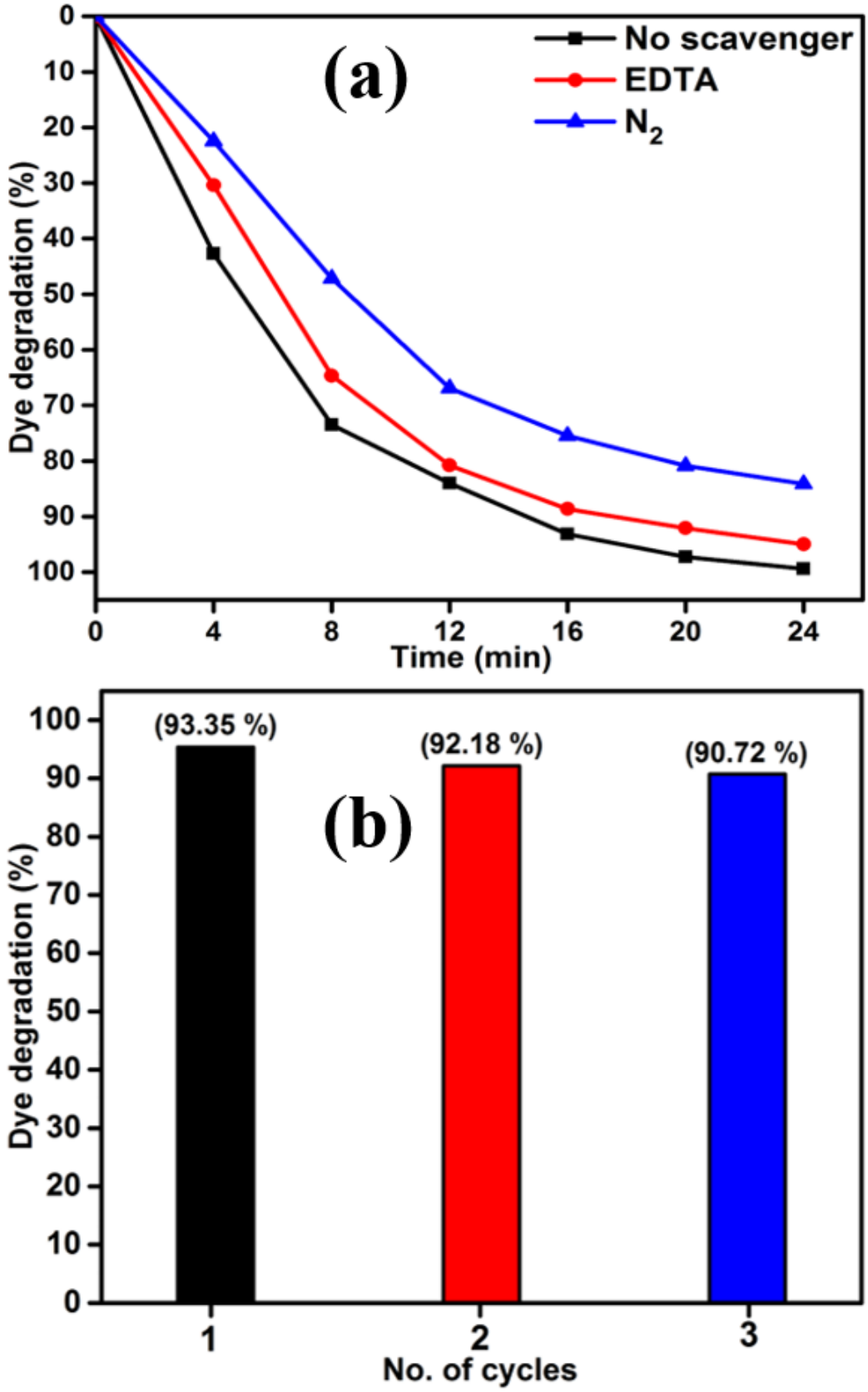

Figure 2.18. (a) MB over MoS_2 in the presence of various scavengers and (b) Reusability of CA3 photocatalyst under visible light irradiation.

To examine whether the process was consistent with pseudo-first-order kinetics, $\ln(C_0/C_t)$ was plotted versus irradiation time for the adsorption and degradation of MB on MoS_2 (Figure 2.19). A linear correlation was found between $\ln(C_0/C_t)$ and irradiation time. The apparent rate constants K_{app} obtained by the pseudo-first-order model were 0.0876, 0.1154, 0.0918, 0.2024 and 0.0898 min^{-1} for CA0, CA1, CA2, CA3 and CA4, respectively. The kinetic data obtained by the pseudo-first-order model, including the apparent rate constants, corresponding correlation coefficients (R^2) and maximum dye degradation in the presence of the MoS_2 nanostructures, are presented in Table 1. CA3 displayed a photocatalytic activity approximately twice that of the pure sample (CA0). A comparison was made between the photocatalytic performance of the materials developed in this work and those of other recently reported MoS_2 nanostructures, as shown in Table 2. It can be seen that the MoS_2 produced in this work showed enhanced activity, with a greater amount of dye loading (50 mg/L). The layered MoS_2 nanosheets achieved 99.37 % degradation of MB in 24 min (CA3), which is higher than any other reported value, indicating the enhanced effectiveness of the nanosheets generated by our method.

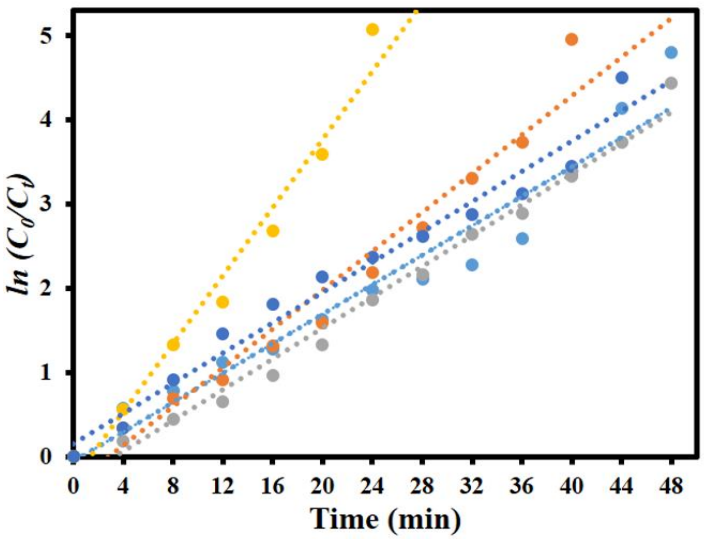

Figure 2.19. Kinetic plot of $\ln(C_0/C_t)$ as a function of time (min) for the degradation of MB.

Based on the above results, we propose a possible photocatalytic mechanism of the degradation of MB under visible-light irradiation [37]:

$$MoS_2 + h\nu \rightarrow MoS_2\,(e^-/h^+) \quad (1)$$

$$O_2 + e^- \rightarrow \bullet O_2^- \quad (2)$$

$$H_2O + h^+ \rightarrow \bullet OH + h^+ \quad (3)$$

$$\bullet O_2^- + 2H + e^- \rightarrow H_2O_2 \quad (4)$$

$$H_2O_2 + e^- \rightarrow \bullet OH + OH^- \quad (5)$$

$$h^+ + OH^- \rightarrow \bullet OH \quad (6)$$

$$\bullet OH + MB \rightarrow CO_2 + H_2O + NO_3^- + NH_4^+ + Cl^- \quad (7)$$

MoS_2 absorbs over a large fraction of the solar spectrum, as shown in Figure 2.20. This process results in the excitation of electrons (e^-) from the valence band (E_{VB} = 2.3 eV) to the conduction band (E_{CB} = 0.4 eV), subsequently generating holes (h^+) in the valence band [38-40]. The absorbed photons have a higher energy than the band gap of the catalyst. The photo-generated holes react with either water (H_2O) or hydroxyl ions (OH^-) adsorbed onto the catalyst surface to produce hydroxyl radicals (•OH), and the photo-generated electrons react with oxygen (O_2) to form superoxide radicals ($\bullet O_2^-$). Consequently, both •OH and $\bullet O_2^-$ radicals can decompose the organic compounds to form CO_2, H_2O and other inorganic molecules as harmless products [41].

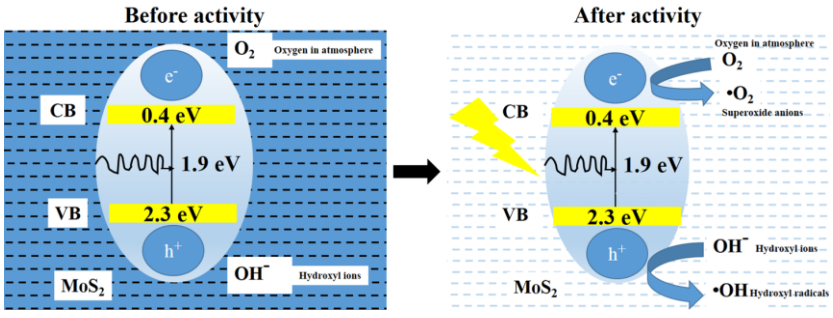

Figure 2.20. Schematic representation of photocatalytic mechanism.

Sample code	K_{app} (MoS_2)	R^2	Maximum degradation (%)	Time taken for maximum degradation (min)
CA0	0.0876	0.9479	99.17	48
CA1	0.1154	0.9613	99.30	40
CA2	0.0918	0.9858	98.82	48
CA3	0.0898	0.9717	99.37	24
CA4	0.2024	0.9717	98.89	44

Table 1 Observed pseudo-first-order rate constants, R^2 values, maximum degradation (%) and time required for maximum degradation by MoS_2 nanosheets.

Table 2 Comparison of photocatalytic performance of MoS_2 in this research and the reported literature

Material	Morphology	Dye concentration (mg/L)	Catalyst amount (mg)	Light Source	Dye	Dye degradation (%)	Time taken for degradation (min)	Ref.
MoS_2	Flower-like spheres	10	40	150 W Xenon lamp	MB	95.6	90	42
MoS_2	Porous microspheres	10	20	100 W Xenon lamp	MB	89.2	150	43
MoS_2	Nano flowers	30	20	175 W Halogen lamp	RhB	97.2	70	22
MoS_2	Nano sheets	20	15	N/A	MO	85	30	44
MoS_2/TiO_2	Nano belts	15	1	300 W Xenon lamp	RhB	86.9	20	45
MoS_2/TiO_2	Nano spheres	5	10	500 W Xenon lamp	RhB	81.8	180	46
MoS_2/C_3N_4	Nano sheets	5	5	300 W Xenon lamp	RhB & MO	N/A	N/A	47
MoS_2/GO	Nano sheets	1	10	500 W Xenon lamp	MB	99	60	48
MoS_2	Nano sheets	50	50	400 W Asahi spectra (Xenon lamp)	MB	99.3	24	This work

2.4 Conclusion

MoS_2 layered nanostructures were synthesized by hydrothermal growth. The role of citric acid in the formation of the layered MoS_2 nanostructures was studied. The obtained results confirmed that the citric acid played a determining role in the formation and functional properties of MoS_2. The XRD patterns revealed the formation of hexagonal MoS_2. The morphological analysis confirmed the presence of layered MoS_2 nanostructures. The photocatalytic activity of MoS_2 to degrade MB under visible-light irradiation was studied. The maximum degradation efficiency was observed within 24 min for MoS_2 capped with 0.04 M citric acid. Moreover, this sample exhibited 96% degradation of the dye within 2 min at the optimum pH value, 12. This performance is superior to the commercial P25 photocatalyst.

References

1. Kuchibhatla, S., Karakoti, A. S., Bera, and D., Seal, S., Prog. Mater. Sci., 2007, 52, 699 - 913.
2. Trindade, T., O'Brien, P. and Pickett, N. L., Chem. Mater., 2001, 13, 3843 - 3858.
3. Yoffe, A. D., Adv. Phys., 1993, 42, 173 - 266.
4. Yoffe, A. D., Adv. Phys., 2001, 50, 1 - 208.
5. Kucur, E., Bucking, W., Giernoth, R. and Nann, T., J. Phys. Chem. B., 2005, 109, 20355 - 20360.
6. Peng, Xiaogang, Michael Schlamp, C. andreas Kadavanich, V. and Alivisatos, A. P., J.Am.Chem. Soc., 1997, 119, 7019 - 7029.

7. Feldheim, D. L. and Foss, C. A., Jr., Metal Nanoparticles, Marcel Dekker, New York, 2002.

8. Lee, J., Sundar, V.C., Heine, J. R., Bawendi, M. G. and Jensen, K. F., Advanced Materials Communications, 2000, 12 (15), 1102 - 1105.

9. Huynh, Wendy, U., Janke Dittmer, William Libby, C., Gregory Whiting, L. and Paul Alivisatos, A., Advanced Functional Materials, 2003, 13, 73 - 79.

10. Zhu, G. H., Tomsia, K., Yu, E. M., Motlan, E. M. and Goldys, E.M., Chin. Chem. Lett., 2007, 18 (5), 581.

11. I. Song, C. Park and H. Cheul Choi, RSC Adv., 2015, 5, 7495 – 7514.

12. S. Shang, G. Lindwall, Y. Wang, J. Redwing, T. Anderson and Z. Liu, *Nano Lett.*, 2016, DOI: 10.1021/acs.nanolett.6b02443.

13. X. Bokhimi, J. A. Toledo, J. Navarette, X. C. Sun and M. Portilla, Int. J. Hydrogen Energy, 2001, 26, 1271 – 1277.

14. A. Splendiani, L. Sun, Y. Zhang, T. Li, J. Kim, C. Yung, G. Galli and F. Wang, Nano Lett., 2010, 10, 1271 – 1275.

15. C. Song, K. Yu, H. Yin, H. Fu, Z. Zhang, N. Zhang and Z. Zhu, J. Mater. Chem. C, 2014, 2, 4196 - 4202.

16. Y. Wang, S. Li, H. Shi and K. Yu, Nanoscale, 2012, 4, 7817– 7824.

17. H. Yin, K. Yu, C. Song, R. Huang and Z. Zhu, ACS Appl. Mater. Interfaces, 2014, 6, 14851– 14860.

18. H. Yin, K. Yu, C. Song, Z. Wang and Z. Zhu, Nanoscale, 2014, 6, 11820–11827.

19. L. Lu-Lu, C. Jie-Jie, Z. Xing, Z. Ai-Yong, H. Yu-Xi, R. Qing and Y. Han-Qing, NPG Asia. Mater., 2016, 8, 1 – 9.

20. S. Harish, M. Navaneethan, J. Archana, A. Silambarasan, S. Ponnusamy, C. Muthamizhchelvan and Y. Hayakawa, Dalton Trans., 2015, 44, 10490 – 10498.

21. S. V. Prabhakar Vattikuti, C. Byon, Ch. Venkata Reddy, B. Venkatesh and J. Shim, J. Mater. Sci., 2015, 50, 5024 – 5038.

22. L. Peitao, L. Yonggang, Y. Weichun, M. Ji and G. Daqiang, Nanotechnology, 2016, 27, 1 - 8.

23. W. Ho, J. C. Yu, J. Lin, J. G. Yu and P. S. Li, Langmuir, 2004, 20, 5865 - 5869.

24. X. Zong, H. J. Yan, G. P. Wu, G. J. Ma, F. Y. Wen, L. Wang and C. Li, J. Am. Chem. Soc., 2008, 130, 7176 - 7177.

25. F. A. Deorsola, N. Russo, G. A. Blengini and D. Fino, Chem. Eng. J., 2012, 1-6, 195 – 196.

26. T. C. Prathna, N. Chandrasekaran and Amitava Mukherjee, Colloids Surf. A, 2011, 390, 216 - 224.

27. Y. Huo, Y. Jin and Y. Zhang, J. Mol. Catal. A: Chem., 2010, 331, 15 - 20.

28. A. Parkinson, H. Sun and J. Sadler, Chem. Commun., 1998, 8, 881 - 882.

29. W. Luo, L. Zhu, N. Wang, H. Tang, M. Cao and Y. She, Environ. Sci. Technol., 2010, 44, 1786 - 1791.

30. J. Liang, J. Liu, Q. Xie, S. Bai, W. Yu and Y. Qian, J. Phys. Chem. B, 2005, 109, 9463 - 9467.

31. A. Samotus, A. Kanas, M. Dudek, R. Grybos and E. Hodorowicz, Trans. Mater. Chem., 1991, 16, 495 – 499.

32. D. H. Killeffer and Arthur Linz, Interscience Publication, 1952, 95 - 109.

33. J. Z. Kong, AD. Li, XY. Li, HF. Zhai, WQ. Zhang, YP. Gong, H. Li and D. Wu, J. Solid. State. Chem., 2010, 183, 1359 – 1364.

34. M. M. Ali and K. Yesodha Sandhya, New J. Chem., 2016, 40, 8123 - 8130.

35. S. Harish, J. Archana, M. Navaneethan, A. Silambarasan, K. D. Nisha, S. Ponnusamy, C. Muthamizhchelvan, H. Ikeda, D. K. Aswal and Y. Hayakawa, RSC Adv., 2016, 6, 89721 - 89731.

36. R. Vinoth, P. Karthik, C. Muthamizhchelvan, B. Neppolian and M. Ashokkumar, Phys. Chem. Chem. Phys., 2016, 18, 5179 - 5191.

37. A. Ajmal, I. Majeed, R. Naseem Malik, H. Idriss and M. Amtiaz Nadeem, RSC Adv., 2014, 4, 37003 - 37026.

38. G. Zhou, X. Xu, J. Yu, B. Feng, Y. Zhang, J. Hu and Y. Zhou, CrystEngComm, 2014, 16, 9025 - 9032.

39. Y. Liu, Y. X. Yu and W. D. Zhang, J. Phys. Chem. C, 2013, 117, 12949 - 12957.

40. H. Liu, T. Lv, C. Zhu, X. Su and Z. Zhu, J. Mol. Catal. A: Chem., 2015, 396, 136 - 142.

41. N. Chinh Chien, V. Nhu Nang and D. Trong-On, J. Mater. Chem. A, 2015, 3, 18345 - 18359.

42. S. Beibei, L. Jinsong, L. Ziquan, W. Menghui, Z. Kongjun, Q. Jinhao and W. Jing, Mater. Lett., 2015, 144, 153 – 156.

43. Z. Zhihua, L. Yuelai, Z. Pingan. A. Eric, S. Muhammad, L. Handong, W. Jiang and W. Zhiming, Mater. Lett., 2014, 131, 122 – 124.

44. Y. Lijuan, X. Haiyan, Z. Dingke and C. Shijian, Mater. Res. Bull., 2014, 55, 221 - 228.

45. D. Yong, Z. Yifeng, N. Wangyan and C. Pengpeng, Appl. Surf. Sci., 2015, 357, 1606 - 1612.

46. Z. Weijia, Y. Zongyou, D. Yaping, H. Xiao, Z. Zhiyuan, F. Zhanxi, L. Hong, W. Jiyang and Z. Hua, Small, 2013, 9, 140 - 147.

47. L. Qian, Z. Ning, Y. Yong, W. Guozhong and N. Dickon H. L, Langmuir, 2014, 30, 8965 - 8972.

48. W. Chuanxi, L. Huihui, L. Zhenyu, W. Jiapeng, X. Zhenzhu and Z. Chi, Part. Part. Syst. Charact., 2016, 33, 221 - 227.

Chapter – 3

Hydrothermal synthesis and functional properties of highly efficient visible light photocatalytic activity of 2D layered MoS_2-TiO_2 nanocomposite hybrid photocatalyst

3.1. Background

The energy crisis and environmental remediation are most important tasks to solve for society and living beings. The sun irradiates 1.5×10^{18} kWh energy to the earth every year, which is approximately 28000 times of the total annual energy consumption [1]. Hence, semiconductor photocatalysis seems to be more attractive and easy to apply for clean energy production and environmental remediation [2-4]. The photocatalytic activities of semiconductive material depend on several factors such as the absorption ability of photocatalysis, the separation and transporting rate of the photogenerated electrons and holes, photoabsorption ability in the available light energy region. Titanium dioxide (TiO_2) is the most explored and traditional semiconductor photocatalyst [5]. It has a strong oxidizing power, high stability, low-cost, an abundant source and is relatively non-toxic [6-10]. TiO_2 is considered to be the active photocatalytic component based on charge carrier dynamics, chemical properties and the activity of photocatalytic degradation of organic compounds. TiO_2 is close to being an ideal photocatalyst and the benchmark for photocatalysis performance. TiO_2 is photo stable in solution. Its holes are strongly oxidizing and redox selective. For these reasons, several novel heterogeneous photocatalytic reactions have been reported at the interface of illuminated TiO_2 photocatalyst, and TiO_2-based photocatalysis has been researched exhaustively for environmental cleanup applications. However, TiO_2 responds only for the UV light, which is only 3–5 % of total sunlight [11]. The band gap of

TiO_2 is in the range of 3.0 and 3.2 eV for rutile and anatase phase TiO_2 which is not compatible with visible light excitation [12]. Since the electron–hole recombination rate is faster, it is mainly responsible for limited application in catalysis [13]. Therefore, it is necessary to overcome this problem by charge separation through suppressing the recombination rate of the electron and hole pairs.

MoS_2 has drawn increasing attention because of its layered structure similar to that of graphene. Each layers are composed of three atom layers stacked together, in which Mo atom at the middle is strongly bonded to above and below S atoms [14, 15]. Such a two-dimensional (2D) layered crystal structure provides convenient electron transfer and many active sites for sunlight absorption. The band gap of MoS_2 increases with decreasing the number of layers due to quantum confinement effect. The direct band gap of ~1.8 eV makes it a visible light active photocatalyst [16, 17]. Weijia Zhou et al., synthesized a few layers of 2-D MoS_2/TiO_2 composite photocatalyst by hydrothermal method at 200 ºC for 24 h and enhanced the light absorption range for the photocatalytic H_2 production [18]. It is well known that the coupling of two semiconductors with narrow and wide band gaps could extend the solar spectrum for light utilization. Therefore, it is necessary to couple two semiconductors with the matched energy levels, leading to the enhanced photocatalytic activity under visible light irradiation through interfacial charge transfer between MoS_2 and TiO_2 nanosheets [19].

I prepared the layered MoS_2 and MoS_2/TiO_2 nanosheets by hydrothermal method. The effect of TiO_2 concentration on the formation of nanosheet were investigated. The photocatalytic activity of the synthesized materials was characterized by quantifying the rate of methylene blue (MB) degradation in the aqueous suspension under visible light irradiation. MoS_2/TiO_2 nanocomposite photocatalyst exhibited enhanced light absorption capacity when

comparing to pure MoS_2 and TiO_2 photocatalyst. Kinetics, electron trapping and possible photocatalytic mechanism were studied.

3.2 Experimental procedure

3.2.1 Synthesis of 2D layered MoS_2 nanostructures

2D layered MoS_2 nanosheets were prepared by a hydrothermal method similar to the chapter I. 0.04 M of sodium molybdate dihydrate, 0.08 M of thioacetamide and 0.04 M of citric acid were dissolved in 50 mL of deionized water under vigorous stirring for 4 h. The transparent aqueous solution was transferred into 100 mL capacity of stainless steel autoclave and maintained at 180 ºC for 24 h. The final product was collected from autoclave through centrifugation thrice with deionized water and ethanol and dried at 80 ºC for 10 h. The sample was termed as S1.

3.2.2 Synthesis of layered MoS_2-TiO_2 mixtures heterostructure

The MoS_2-TiO_2 mixtures heterostructure were prepared by hydrothermal method. The amount of DAHFT as a Ti source was changed as a parameter. In a typical reaction process, 0.04 M of sodium molybdate dihydrate, 0.08 M of thioacetamide, (0.0015, 0.0030, 0.0050, 0.010 and 0.015 M) of DAHFT and 0.04 M of citric acid were dissolved in 50 mL deionized water under vigorous stirring for 4 h. The transparent aqueous solution was transferred into 100 mL capacity of stainless steel autoclave and maintained at 180 ºC for 24 h. The final product was collected from autoclave through centrifugation thrice with deionized water and ethanol and dried at 80 ºC for 10 h. The samples were termed as S2 (0.0015 M), S3 (0.0030 M), S4 (0.0050 M), S5 (0.010 M) and S6 (0.015 M), respectively.

3.2.3 Photocatalytic dye degradation

Photocatalytic degradation of methylene blue (MB) was carried out under visible light irradiation. The optical absorption of MB at 664 nm was used as monitor wavelength of photodegradation. 5 mg of MB was added to 100 mL of aqueous solution and stirred for 30 min. 50 mg of MoS_2 and MoS_2/TiO_2 photocatalyst was separately added to the above solution. To establish the absorption / desorption equilibrium, the mixed solution was stirred for 30 min. in the dark before photodegradation reaction. The visible light source of xenon lamp was placed 15 cm away from the surface of the solution. The dye degradation surveys were conducted at an interval of 4 min. and the catalyst was isolated by centrifugation. The photodegradation percentage of MB was calculated using the following equation [20],

$$D(\%) = \frac{C_0 - C_t}{C_0} \times 100 \qquad (1)$$

where C_0 and C_t are the concentration of MB at time 0 and t (s), respectively and t is the irradiation time.

3.3 Results and discussion

Figure 3.1 shows the powder XRD patterns of pure MoS_2 and MoS_2/TiO_2 nanocomposites. Figure 1 (S1) shows the pure MoS_2 with diffraction peaks. It corresponded to hexagonal phase of MoS_2 which was well matched with standard JCPDS card number (024-0513). Peaks at 14.4º, 32.6º, 35.8º, 44.2º and 58.2º can be indexed to the (002), (100), (102), (104) and (110) crystal planes, respectively. After the addition of TiO_2, new peaks appeared at 25.2º, 37.8º, 48.0º, 53.8º, 55.0º and 62.6º which corresponded to (101), (103), (200), (105), (211) and (204) crystal planes. It confirmed the presence of TiO_2 in the composition. As the concentration of TiO_2 increased, peak intensity of TiO_2 was increased. The structure of MoS_2 and TiO_2 in all samples was indexed to the hexagonal (024-0513) and anatase structure (021-1272), respectively. No other characteristic peaks were observed.

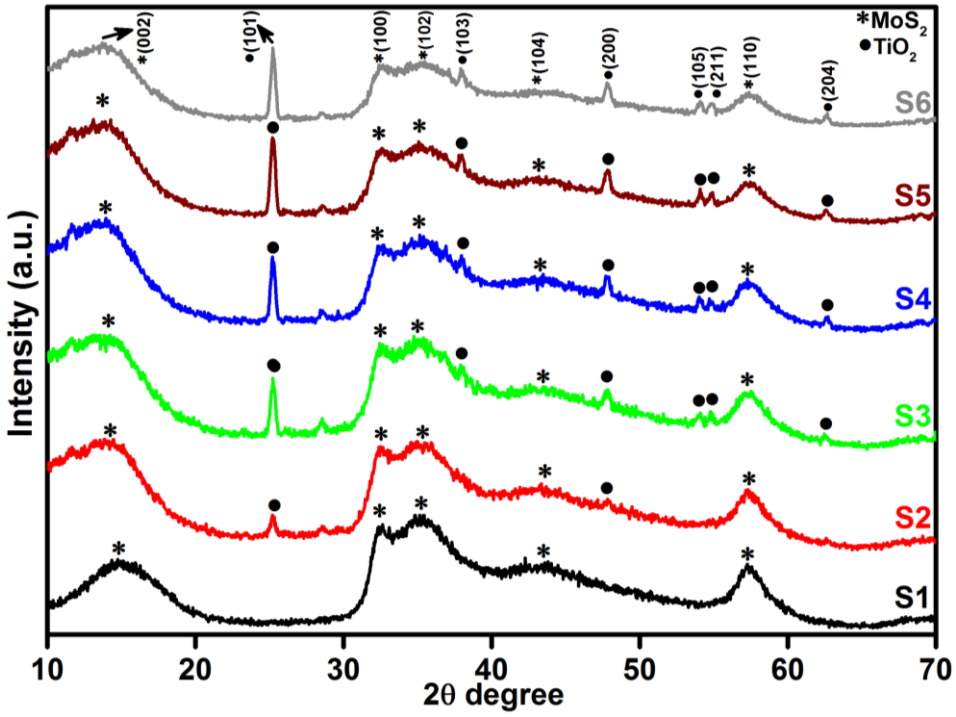

Figure 3.1. XRD patterns of layered MoS_2 and TiO_2 nanosheets.

XPS measurement was carried out to observe the chemical state of MoS_2 and MoS_2/TiO_2 nanocomposite. Figure 3.2 shows the survey spectra of MoS_2/TiO_2. The characteristic peaks at 36.90, 161.80, 229.40 and 529.89 eV, which can be attributed to Ti 3p, S 2p, Mo 3d and O 1s, respectively. The high resolution XPS spectra of Ti 3p, S 2p, Mo 3d and O 1s are shown in Fig. 3.3. Two symmetric peaks appeared for Mo 3d state as shown in Fig. 3.3 (a1-a6). The peaks centered at 228.30 and 231.45 eV (S1) can be attributed to Mo $3d_{5/2}$ and Mo $3d_{3/2}$ states, indicating a +4 oxidation state [21]. The separation between the Mo $3d_{5/2}$ and Mo $3d_{3/2}$ states was 3.1 eV, which was in good agreement with the standard value [22]. The binding energies of sample S2 were shifted to 227.80 and 231 eV from 228.30 and 231.45 eV of pure MoS_2. In further increase in the concentration of TiO_2, the peaks were shifted to 227.90 and 231 eV for sample S3, 227.55 and 230.80 eV for sample S4, 227.55 and 230.80 eV for sample S5, and 227.5 and 230.80 eV for sample S6, respectively. The samples showed the significant peak shift because of strong interaction between Mo and Ti. S 2p spectra shown in Fig. 3.3 (b1-b6) can be deconvoluted into two peaks located at 161 and

162.05 eV, which can be attributed to S $2p_{3/2}$ and S $2p_{1/2}$ orbitals of divalent sulfide ions (S^{2-}). The energy separation between S $2p_{3/2}$ and S $2p_{1/2}$ were 1.1 eV, which was in good agreement with the reported value [23]. The binding energies was shifted to 160.50 and 161.72 for sample S2, 160.75 and 161.95 for sample S3, 160.52 and 161.70 for sample S4, 160.52 and 161.70 for sample S5, respectively. Moreover, the samples S4 (a4, b4), S5 (a5, b5) and S6 (a6, b6) the binding energy of $Mo3d_{5/2}$, $Mo3d_{3/2}$, $S2p_{3/2}$ and $S2p_{1/2}$ were shifted about 0.20 eV when compared with samples S2 (a2) and S3 (a3), respectively. This slight shift was attributed to the strong interaction between MoS_2 and TiO_2. Fig. 3.3 (c1-c5) shows the Ti 3p state with peak center at 37 eV. There is no significant peak shift was observed in Ti 3p state. O 1s states of samples are shown in Fig. 3.3 (d1-d5). All the samples exhibited an asymmetrical shape and was deconvoluted into two symmetrical peaks were centered at 530.85 eV and 532.50 eV indicating two different kinds of O species in the samples. The binding energy of 530.85 eV corresponded to the O^{2-} ions surrounded by Ti in the TiO_2 compound system. The shoulder peak was observed at 532.50 eV which corresponded to the chemisorbed oxygen, dissociated oxygen, or OH^- groups on the surface. Similar shift in peaks was observed as the concentration of TiO_2 was increased, 530.60 eV for sample S3, 530 eV for sample S4, 530 eV for sample S5 and 530 eV for sample S6, respectively. O1s binding energy was shifted about 0.20 eV when compared with the samples S1 (d1) and S2 (d2). The XPS measurement confirmed that the presence of TiO_2 in the prepared nanocomposites.

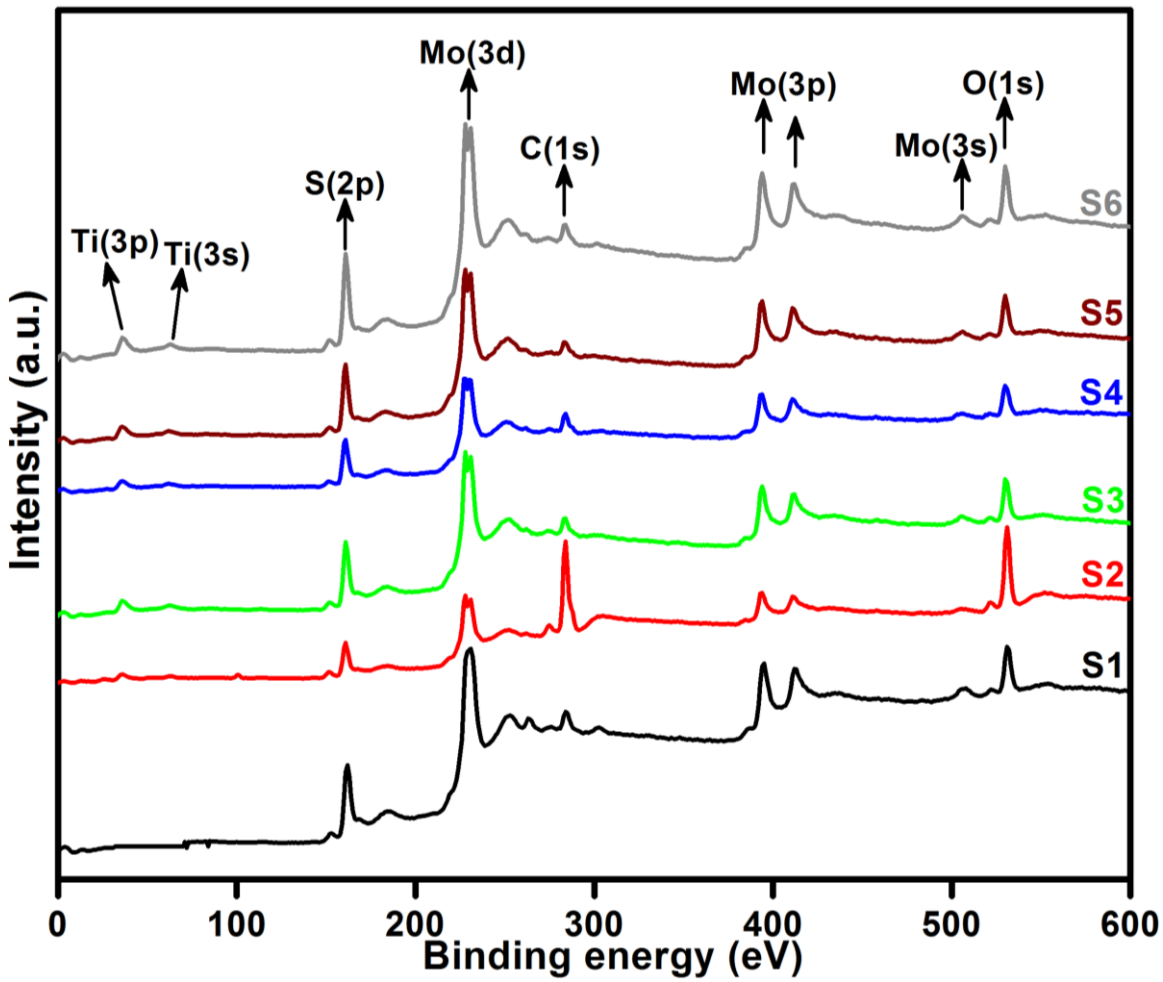

Figure 3.2. High resolution XPS spectra of layered MoS_2 and TiO_2 nanosheets.

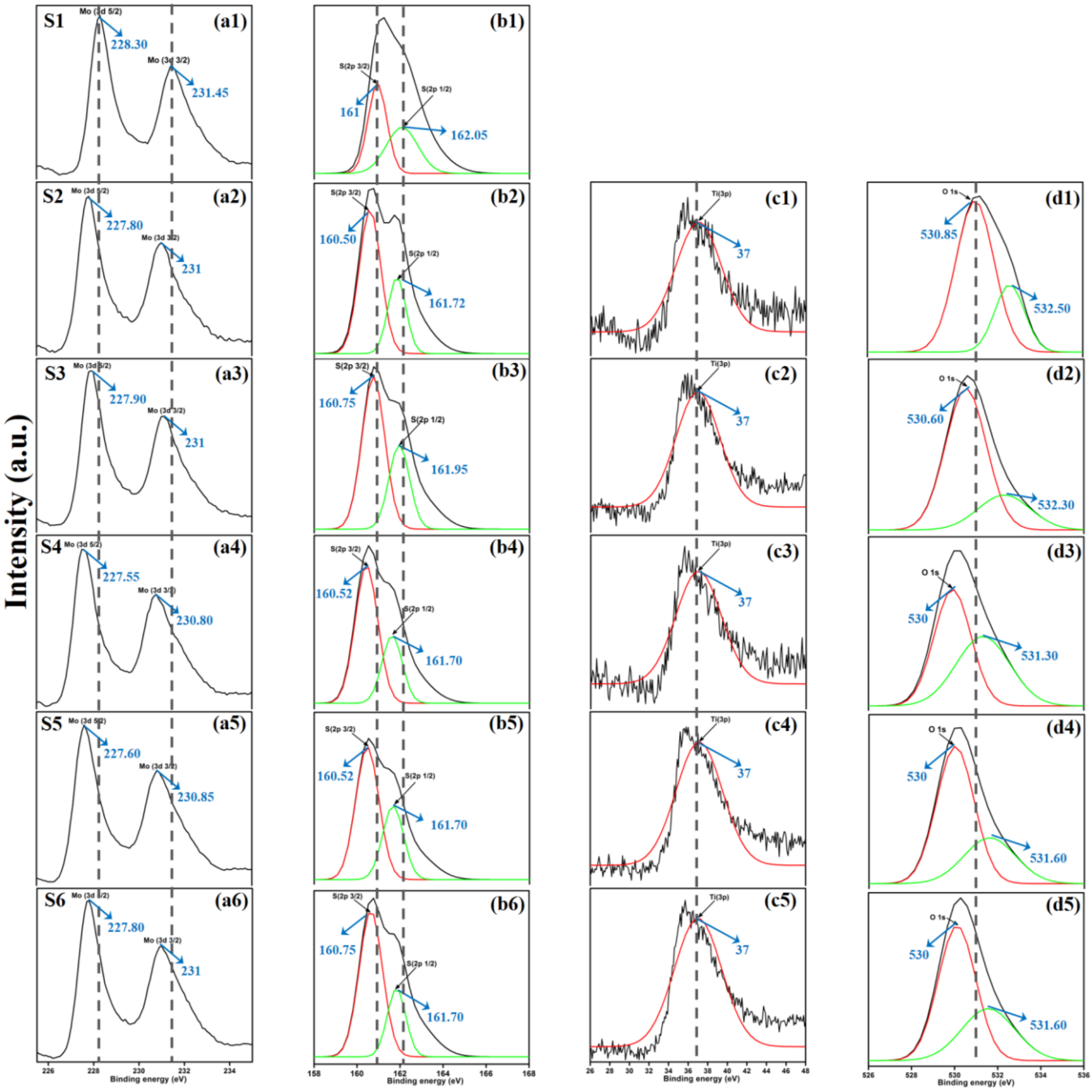

Figure 3.3. XPS spectra of Mo 3d state (a1-a6), S 2p state (b1-b6), Ti 3p state (c1-c5) and O 1s state (d1-d5) of samples S1 to S6.

The morphological analysis was performed using FESEM, TEM and HRTEM as shown in Fig. 3.4. Figure 3.4 (a) shows the monodispersed pure MoS_2 (S1) nanosheets with layered structure. The thickness of each layers was about 20 - 50 nm. When TiO_2 is incorporated into the MoS_2 nanosheets, TiO_2 were agglomerated on the surface of nanosheets. It can be clearly seen in the FESEM images of S4 (j), S5 (m) and S6 (p), respectively. This agglomeration was attributed to the increased ionic strength of TiO_2 nanoparticles. The layered structure of the sample was further characterized by TEM and HRTEM as shown in Figure. 3.4 (b) and (c). MoS_2 nanosheets had 5 - 9 layers and the lattice d-spacing was 0.61 nm which corresponded to the (002) plane. Figure. 3.4 (d), (e) and (f) shows the FESEM, TEM and HRTEM images of MoS_2/TiO_2 nanocomposites of S2 sample, respectively. In the HRTEM images of (f, i, l, o and r) white dash line corresponded to MoS_2 layered nanosheets and white square dot line indicated TiO_2 nanosheets. When the concentration of TiO_2 was increased from 0.0015 to 0.015 M, the formation of TiO_2 nanosheets were observed as shown in the samples S2 to S6. Nanocomposites were composed of MoS_2 and TiO_2 as shown in Fig. 3.4. It is concluded from XPS and TEM analysis that the layered MoS_2 nanosheets and TiO_2 was formed as composites.

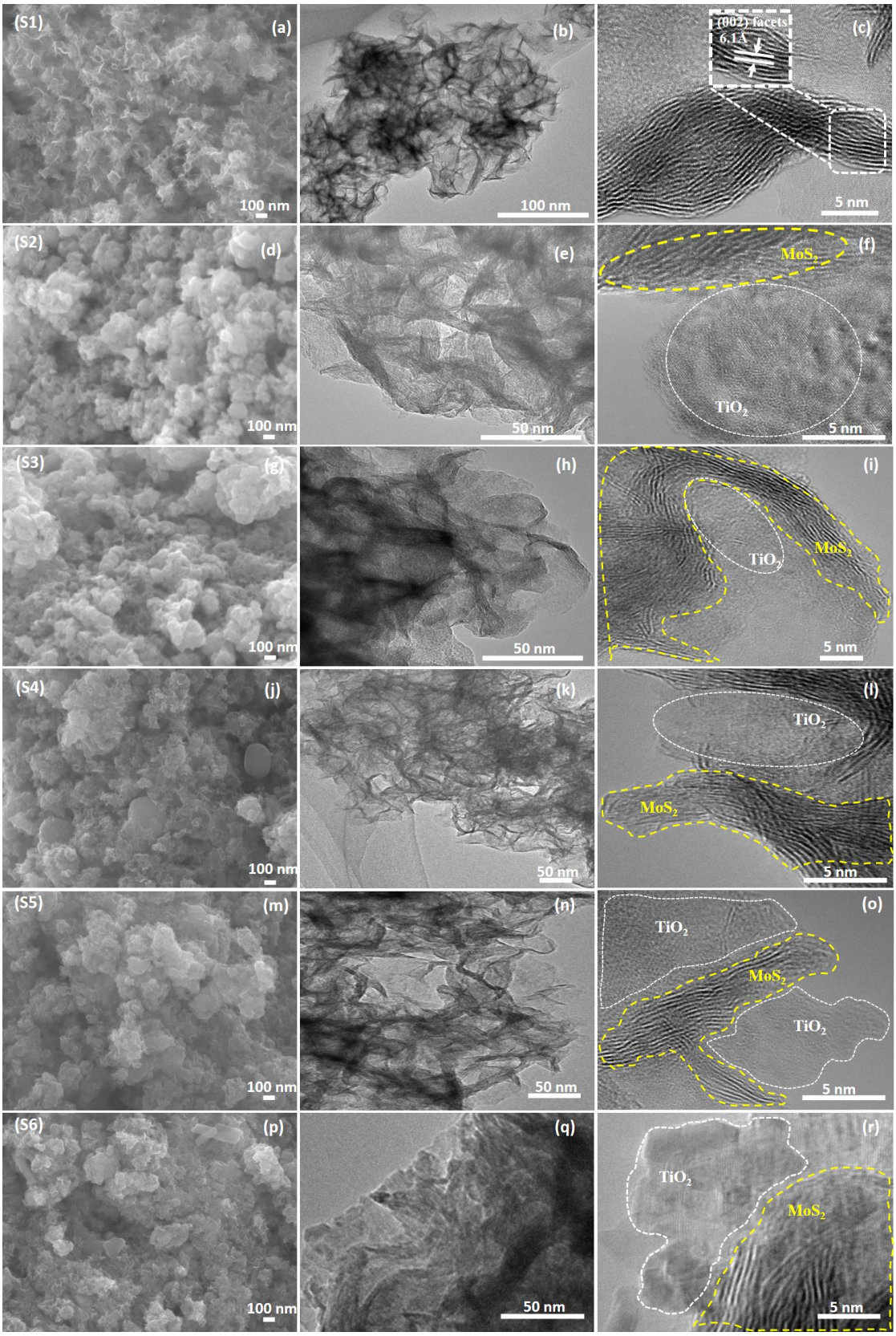

Figure 3.4. (a, d, g, j, m, p) FESEM, (b, e, h, k, n, q) TEM and (c, f, I, l, o, r) HRTEM images of sample S1 to S6.

3.3.1 Photocatalytic activity

Photocatalytic performances of MoS_2 and MoS_2/TiO_2 photocatalyst were examined by degrading MB under visible light irradiation. The characteristic absorption peak of MB at 664 nm is chosen to monitor the photocatalytic degradation of MB. Figure 3.5 shows the time dependent absorption spectra of pure MoS_2 (S1), MoS_2/TiO_2 (S2-S6), respectively. The absorption peak at 664 nm dropped rapidly with illumination time and almost disappeared after 32 min for sample S1. Whereas, for S2, S3, S4, S5 and S6 samples, irradiation time was decreased to 20, 16, 12, 24 and 28 min, respectively. Figure 3.6 shows the percentage of degradation for the samples S1, S2, S3, S4, S5, S6 and P25 (TiO_2) to be 99.20, 99.17, 98.68, 99.33, 98.08, 98.90 and 56.89 %, respectively. Moreover, 71.50, 93.99, 96.79, 99.17, 88.25 and 84.21 % MB was degraded in 12 min of irradiation for sample S1, S2, S3, S4, S5 and S6, respectively. It is evident that the photodegradation efficiency of the MoS_2/TiO_2 photocatalyst was significantly higher than that of pure MoS_2 and TiO_2 (P25). Among all the synthesized samples, S4 showed the enhanced photocatalytic activity because the oxidation state of MoS_2/TiO_2 photocatalyst provided more surface-active sites and strong absorption ability towards organic dye molecules. Moreover, the layered nanosheets favors to the photogenerated charge carrier transferred from TiO_2 to MoS_2. It is a key factor in determining the photocatalytic activities of layered MoS_2/TiO_2 nanocomposites as a photocatalyst. The formation of synergetic interaction between MoS_2 and TiO_2 semiconductors provided an efficient transport platform for charge carrier transfer and enhanced the photocatalytic activities.

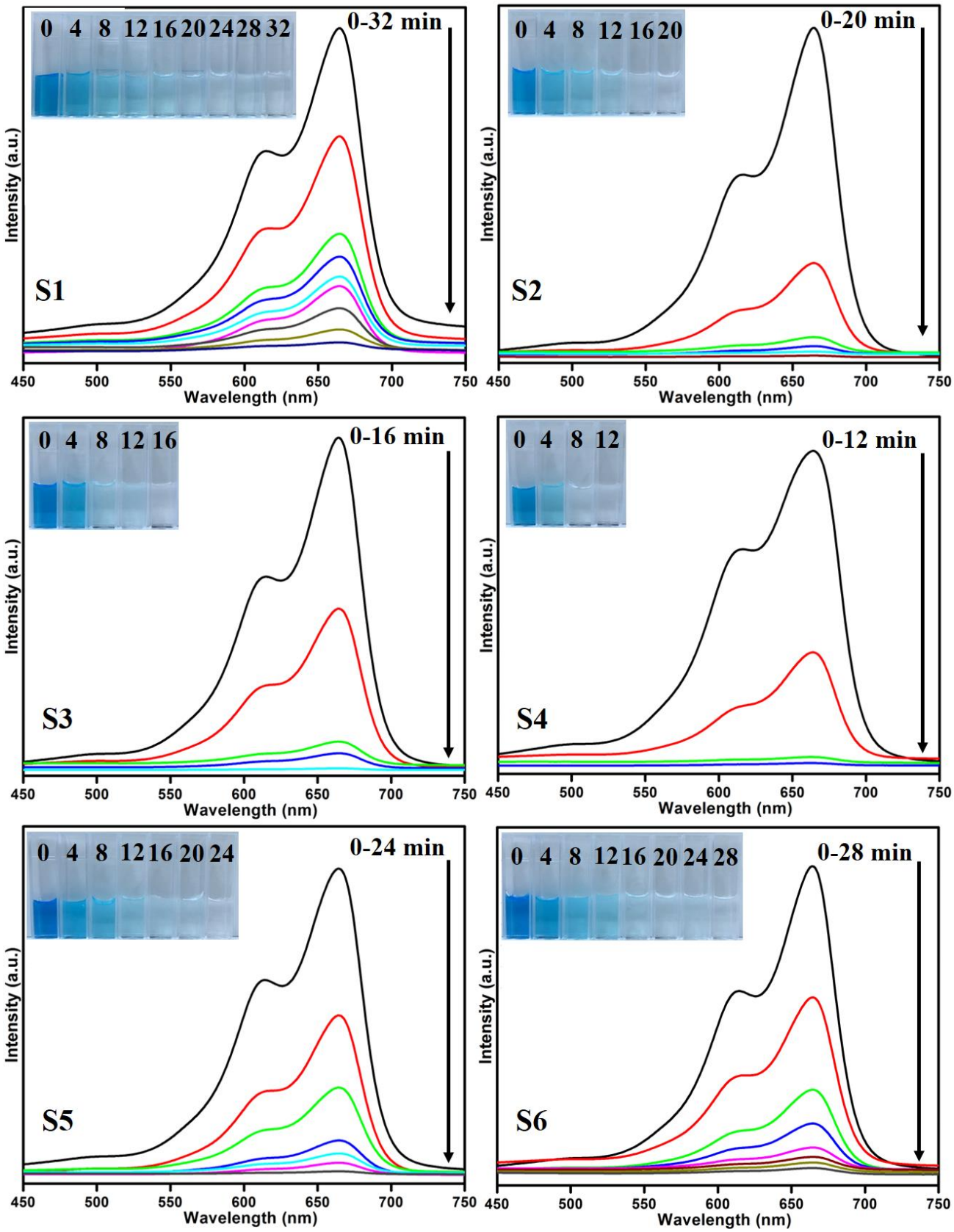

Figure 3.5. UV absorbance spectra of MB samples S1 (a), S2 (b), S3 (c), S4 (d), S5 (e) and S6 (f).

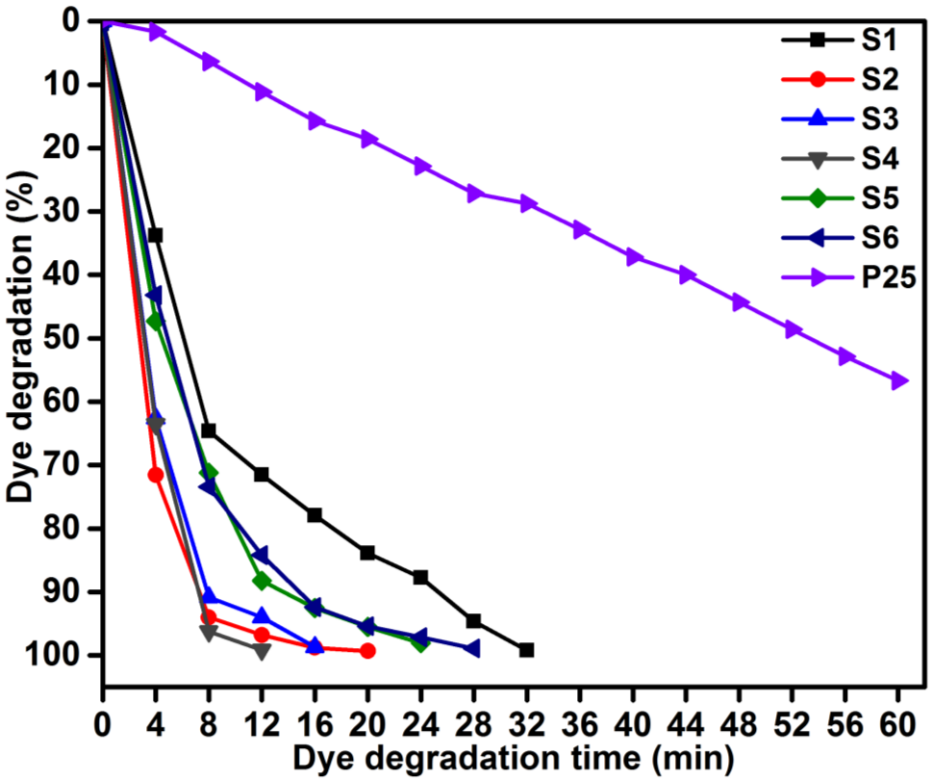

Figure 3.6. MB degradation of samples S1, S2, S3, S4, S5, S6 and P25 Time (min) vs dye degradation (%).

To understand the role of photocatalytic activity, the free radicals trapping experiments were carried out as shown in Figure 3.7. In general, during photocatalysis, hydroxyl radicals (•OH) and superoxide anions (O_2^-•) are the possible reactive species for the degradation of organic pollutants. The disodium ethylenediaminetetraacetate (EDTA-2Na) and N_2 were used as a hole (h^+) and electron acceptor scavenger, respectively [24, 25]. A high purity N_2 gas was purged continuously throughout the reaction process under ambient condition, which eliminated the dissolved oxygen content from the reaction solution and thereby prevented the formation of O_2^-•. The degradation percentage of MB was 88.39 % after 12 min of irradiation instead of 99.33 % in the scavenger free photocatalyst. This conformed that the superoxide anions played a minor role in the photocatalytic degradation of organic pollutant. To further determine the degradation mechanism, EDTA was added into

the solution as •OH radical scavenger. The dye degradation was 72.90 % which indicated suppression of MB degradation rate. This result confirmed that the photoinduced holes (h^+) are one of the main reactive species for the degradation of MB. Therefore, these results clearly determined that MB degradation mainly depended on photogenerated •OH radical. The possible reason for the dye degradation of MoS_2/TiO_2 as a photocatalyst was that superoxide anion radical had the potential to react directly by oxidative pathways. It can also produce singlet oxygen or decompose to H_2O_2, and transformed to hydroxyl radical during MoS_2/TiO_2 photocatalysis process [26-28]. This process was explained in the dye degradation mechanism of MB under visible light irradiation. This results suggest that the rate of photocatalytic degradation of MB was suppressed in the presence of EDTA as a hole (h^+) scavenger. Moreover, the reactive species of superoxide anions (O_2^-•) played a minor role for the degradation of MB. The obtained result indicated that the rate of photocatalytic degradation not only depended on organics but also the nature of catalysts.

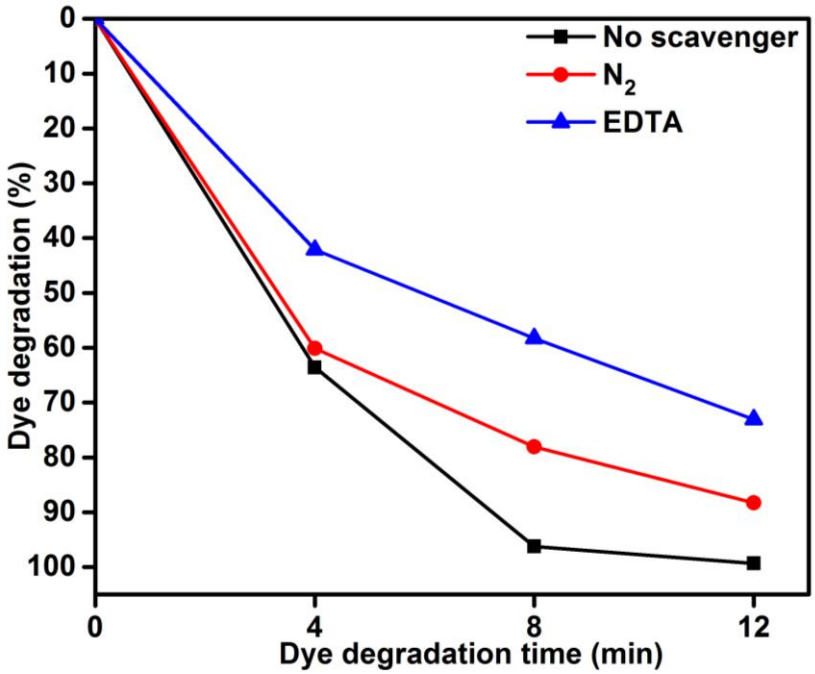

Figure 3.7. MB degradation using MoS_2/TiO_2 nanosheets without scavenger and with scavengers under visible light irradiation.

Figure 3.8 shows the kinetic plot of $ln(C_0/C_t)$ versus irradiation time to investigate whether the process obeyed pseudo first order model or not. A linear correlation exists between $ln(C_0/C_t)$ versus irradiation time. The kinetic data was obtained by the pseudo-first order model. The apparent rate constants (K_{app}), corresponding correlation coefficients (R^2) and maximum dye degradation in presence of MoS_2 and MoS_2/TiO_2 nanocomposites are presented in Table 3.1. The apparent rate constant K_{app} was 0.0965, 0.2512, 0.2895, 0.4162, 0.162 and 0.1564 min^{-1} for S1, S2, S3, S4, S5 and S6, respectively. K value increased with increase of the concentration of TiO_2 from 0.0965 to 0.4162 min^{-1} for sample S1 to S4. With further increase of the TiO_2 concentration, K value decreased to 0.1564 min^{-1} for sample S6. Plots of $ln(C_0/C_t)$ versus irradiation time show that apparent rate constant was about twice higher than pure MoS_2. A comparison was made between the photocatalytic performance of the materials developed in this work and those of other recently reported MoS_2/TiO_2 composite nanostructures, as shown in Table 3.2.

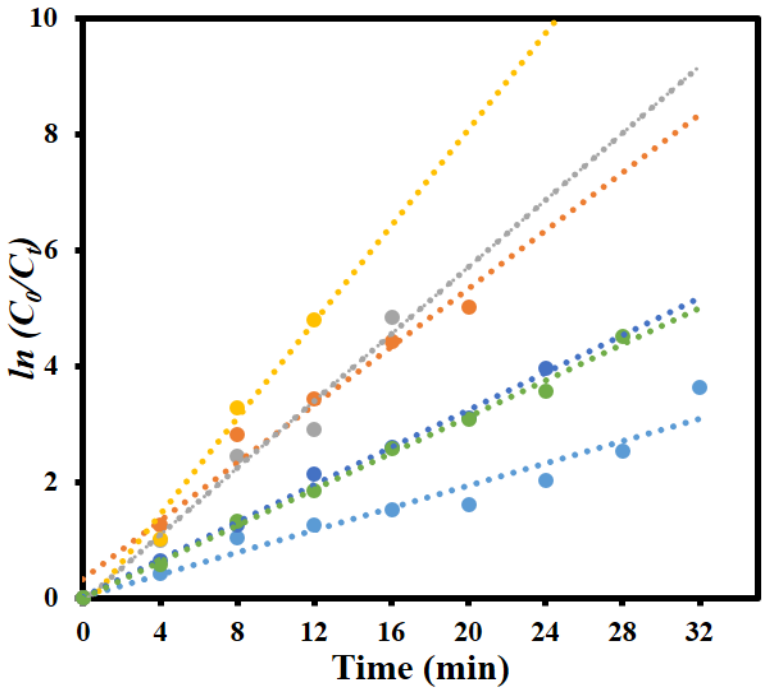

Figure 3.8. Kinetic plot of ln(C_0/C_t) as a function of time (min) for the degradation of MB.

Table 3.1 Observed pseudo-first-order rate constants, R^2 values, maximum degradation (%) and time required for maximum degradation by MoS_2/TiO_2 nanosheets.

Sample code	K_{app} (MoS_2/TiO_2)	R^2	Maximum degradation (%)	Time taken for maximum degradation (min)
S1	0.0965	0.937	99.17	32
S2	0.2512	0.9741	99.10	20
S3	0.2895	0.9723	98.68	16
S4	0.4162	0.9812	99.33	12
S5	0.162	0.9946	98.08	24
S6	0.1564	0.9956	98.90	28

Table 3.2 Comparison of photocatalytic performance of MoS_2/TiO_2 composites in this research and the reported literatures.

Material	Light source	Dye	Dye degradation (%)	Time taken for degradation (min)	Ref.
MoS_2/TiO_2	500 W xenon lamp	RhB	81.8	180	18
MoS_2/TiO_2	30 W day lamp	MB	98	90	32
MoS_2/TiO_2	30 W day lamp	MO	95.1	120	35
MoS_2/TiO_2	500 W xenon lamp	MO	97	60	36
MoS_2/TiO_2	300 W xenon lamp	RhB	86.9	20	37
MoS_2/TiO_2	400 W Asahi spectra (xenon lamp)	MB	99.33	12	This work

Based on the above result, we propose the possible photocatalytic mechanism for the degradation of MB using MoS_2/TiO_2 as photocatalysts [29]:

$$MoS_2/TiO_2 + h\nu \rightarrow MoS_2\,(h^+)/TiO_2\,(e^-) \qquad \text{(Step 1)}$$

$$O_2 + e^- \rightarrow \bullet O_2^- \qquad \text{(Step 2)}$$

$$H_2O + h^+ \rightarrow \bullet OH + H^+ \qquad \text{(Step 3)}$$

$$\bullet O_2^- + H_2O \rightarrow \bullet HO_2 + OH^- \qquad \text{(Step 4)}$$

$$\bullet HO_2 + H_2O \rightarrow H_2O_2 + \bullet OH \qquad \text{(Step 5)}$$

$$H_2O_2 \rightarrow 2\bullet OH \qquad \text{(Step 6)}$$

$$\bullet OH + MB \rightarrow CO_2 + H_2O + NO^-_3 + NH^+_4 + Cl^- \qquad \text{(Step 7)}$$

Figure 3.9 shows the reusability of sample S4 photocatalyst for the degradation of methylene blue was studied over four cycles under visible light irradiation. The dye concentration was adjusted each run to its initial value. Photocatalysts were reused for four cycles and obtained degradation values are 95.18, 92.80, 86.66 and 83.15, respectively. The efficiency of the sample S4 did not declined significantly, which suggested that the catalyst had good stability and sustainability.

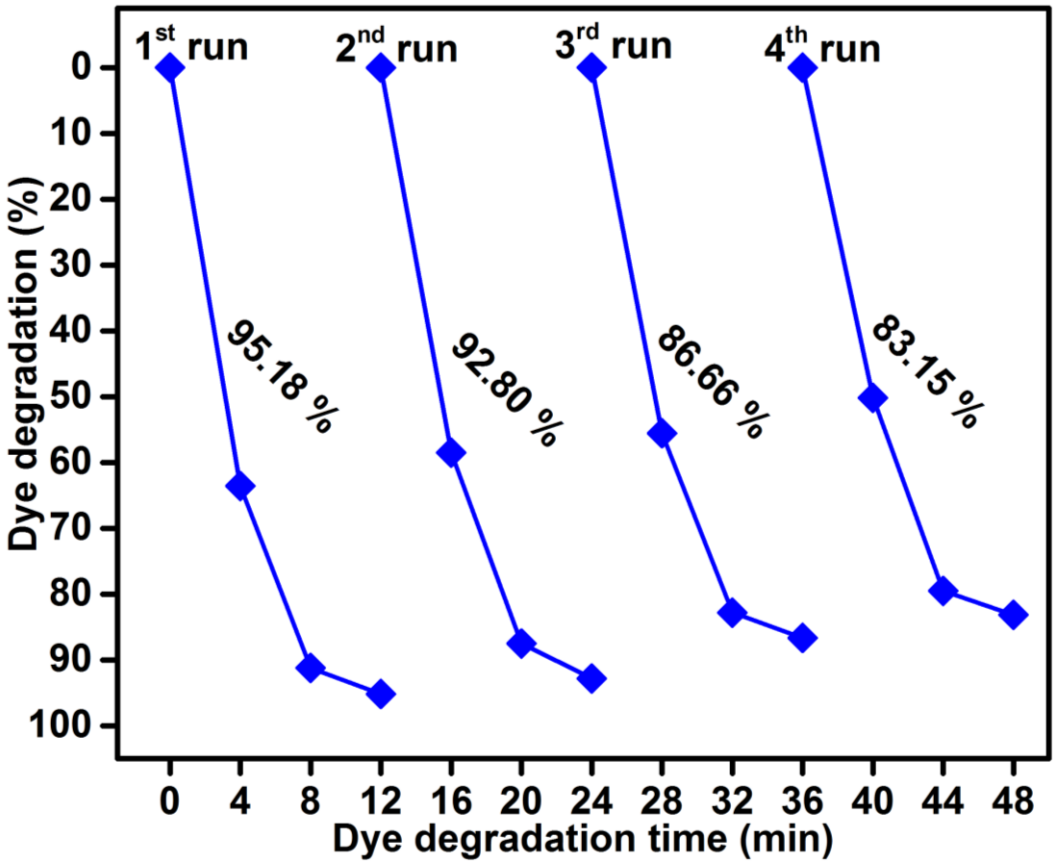

Figure 3.9. Reusability of sample S4 photocatalyst under visible light irradiation.

The schematic diagram (Figure 3.10) illustrates the energy band structure and the charge transfer mechanism. MoS_2 is a narrow band gap (1.9 eV) semiconductor with a work function of 4.52 eV, while anatase TiO_2 is a wide band gap (3.2 eV) semiconductor with a work function of 4.5 eV [30, 31]. The electron affinity of MoS_2 was 4.07 ± 0.35 and for TiO_2

value between 3.9 and 4.4 eV, respectively [32-34]. Under the visible light irradiation, electrons are excited from valance band of MoS_2 to conduction band, leaving behind holes in the valance band. The photoinduced electrons in the conduction band of MoS_2 are transferred to the conduction band of TiO_2 which act as a photoelectronic receiver. The photo-generated holes react with either water (H_2O) or hydroxyl ions (OH^-) adsorbed onto the catalyst surface to produce hydroxyl radicals (•OH) and the photo-generated electrons react with oxygen (O_2) to form superoxide radicals ($•O_2^-$). Consequently, both •OH and $•O_2^-$ radicals can decompose the organic compounds to form CO_2, H_2O and other inorganic molecules as a harmless compound.

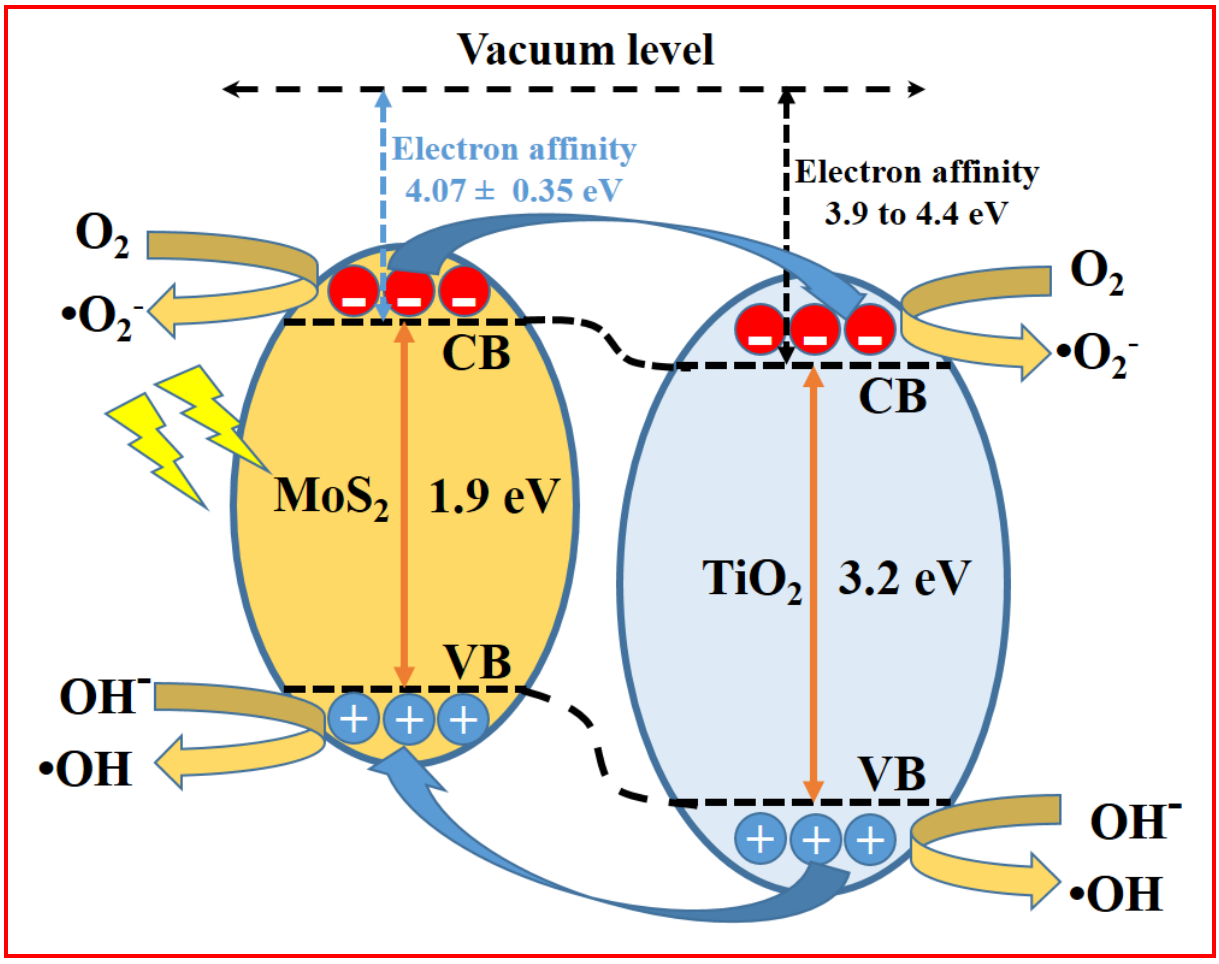

Figure 3.10. Schematic representation of charge transfer mechanism between MoS_2 to TiO_2 photocatalysis.

3.4. Conclusion

Pure layered MoS_2 and MoS_2-TiO_2 nanocomposites were successfully synthesized by facile hydrothermal method. The XRD patterns revealed the hexagonal MoS_2 and anatase structure of TiO_2. The morphological analysis confirmed the presence of layered MoS_2 and TiO_2 nanosheets. The obtained results confirmed that the MoS_2/TiO_2 nanocomposite photocatalyst had obvious enhancement of photocatalytic activity for MB degradation under visible light irradiation. The interfacial charge carriers transferred between MoS_2 and TiO_2 nanosheets and was effectively suppressed the electron hole pair recombination. The maximum degradation efficiency was attained for MoS_2/TiO_2 (S4) nanocomposite photocatalyst in 12 min. The obtained result was three times higher than the pure MoS_2 and commercial P25 TiO_2. The free radicals trapping experiment confirmed that photogenerated (•OH) radicals played an important role in the degradation of organic pollutant.

References

1. C. Minero, E. Pelizzetti, S. Malato and J. Blanco, Chemosphere, 1993, 26, 2103 - 2119.
2. H. Liu, T. Lv, X. H. Wu, C. K. Zhu, Appl. Surf. Sci., 2014, 30, 242 - 246.
3. S. Ameen, M. S. Akhtar, M. Nazim, H. S. Shin, Mater. Lett., 2013, 96, 228 - 232.
4. S. Harish, M. Navaneethan, J. Archana, A. Silambarasan, S. Ponnusamy, C. Muthamizhchelvan and Y. Hayakawa, Dalton Trans 2015, 44, 10490-10498.
5. A. Fujishima and K. Honda, Nature, 1972, 238, 37 - 38.
6. J. Archana, M. Navaneethan and Y. Hayakawa, J. Power. Sources, 2013, 242, 803-810.
7. J. Archana, S. Harish, M. Sabarinathan, M. Navaneethan, S. Ponnusamy, C. Muthamizhchelvan, M. Shimomura, H. Ikeda, D.K. Aswal and Y. Hayakawa, RSC Adv., 2016, 6, 68092-68099.
8. B. Banerjee, V. Amoli, A. Maurya, A. Sinha and A. Bhaumik, Nanoscale, 2015, 7, 10504 - 10512.
9. G. H. Moon, W. Kim, D. Bokare, N. Sung and W. Choi, Energy Environ. Sci., 2014, 7, 4023 - 4028.
10. S. Hernandez, D. Hidalgo, A. Sacco, A. Chiodoni, A. Lamberti, V. Cauda, E. Tresso and G. Saracco, Phys. Chem. Chem. Phys., 2015, 17, 7775 - 7786.
11. C. Wang, H. Lin, Z. Liu, J. Wu, Z. Xu and C. Zhang, Part. Part. Syst. Charact., 2016, 33, 221 - 227.

12. H. G. Yang, C. H. Sun, S. Z. Qiao, J. Zou, G. Liu, S. C. Smith, H. M. Cheng and G. Q. Lu, Nature, 2008, 453, 638 - 641.

13. L. Zheng, S. Han, H. Liu, P. Yu and X. Fang, Small, 2016, 12, 1527 - 1536.

14. Y. G. Li, H. L. Wang, L. M. Xie, Y. Y. Liang, G. S. Hong and H. J. Dai, J. Am. Chem. Soc., 2011, 133, 7296 - 7299.

15. I. Song, C. Park and H. Cheul Choi, RSC Adv., 2015, 5, 7495 - 7514.

16. T. S. Li and G. L. Galli, J. Phys. Chem.C., 2007, 111, 16192 - 16196.

17. A. Splendiani, L. Sun, Y. Zhang, T. Li, J. Kim, C. Yung, G. Galli and F. Wang, Nano Lett., 2010, 10, 1271 - 1275.

18. W. Zhou, Z. Yin, Y. Du, X. Huang, Z. Zeng, Z. Fan, H. Liu, J. Wang and H. Zhang, Small, 2013, 9, 140-147.

19. H. L. Wang, L. S. Zhang, Z. G. Chen, J. Q. Hu, S. J. Li and Z. H. Wang, Chem. Soc. Rev., 2014, 43, 5234 - 5244.

20. S. Harish, J. Archana, M. Navaneethan, A. Silambarasan, K. D. Nisha, S. Ponnusamy, C. Muthamizhchelvan, H. Ikeda, D. K. Aswal and Y. Hayakawa, RSC Adv., 2016, 6, 89721 - 89731.

21. Y. Yan, B. Xia, N. Li, Z. Xu, A. Fisher and X. Wang, J. Mater. Chem. A, 2015, 3, 131 - 135.

22. F. A. Deorsola, N. Russo, G. A. Blengini and D. Fino, Chem. Eng. J., 2012, 1-6, 195-196.

23. J. Baltrusaitis, Courtney R. Usher and Vicki H. Grassian, Phys. Chem. Chem. Phys., 2007, 9, 3011-3024.

24. L. Peitao, L. Yonggang, Y. Weichun, M. Ji and G. Daqiang, Nanotechnology, 2016, 27, 225403 - 225410.

25. G. Gong, Y. Liu, B. Mao, B. Wang, L. Tan, D. Li, Y. Liu and W. Shi, RSC Adv., 2016, 6, 99023 - 99033.

26. S. Zheng, Y. Cai and Kevin E. O'Shea, J. Photochem. Photobiol., A, 2010, 210, 61 - 68.

27. P. Zheng, Z. Pan, H. Li, B. Bai and W. Guan, J. Mater. Sci. - Mater. Electron., 2015, 26, 6399 - 6410.

28. X. V. Doorslaer, P. M. Heynderickx, K. Demeestere, K. Debevere, H. V. Langenhove and J. Dewulf, Appl. Catal., B., 2012, 111-112, 150 - 156.

29. W. Ho, J. C. Yu, J. Lin, J. Yu and P. Li, Langmuir, 2004, 20, 5865 - 5869.

30. Y. Liu, Y. X. Yu and W. D. Zhang, J. Phys. Chem.C, 2013, 117, 12949 - 12957.

31. E. Scalise, M. Houssa, G. Pourtois, V. V. Afance'ev and A. Stesmans, Physica E, 2014, 56, 416 - 421.

32. R. Schlaf, O. Lang, C. Pettenkofer and W. Jaegermann. J. Appl. Phys. 1999, 85, 2732-2753.

33. J. Robertson, J. Vac. Sci. Technol., B: Microelectron. Process. Phenom, 2000, 18, 1785-1791.

34. M. Pergo, G. Seguini, G. Scarel, M. Fanciulli and F. Wallrapp, J. Appl. Phys. 2008, 103, 043509.

35. K. Hong Hu, Y. Kui Cai and S. Li, Adv. Mat. Res., 2011, 197-198, 996-999.

36. K. Hong Hu, X. Guo Hu and Y. Fu Xu, J. Mater. Sci., 2010, 45, 2640-2648.

37. W. Zhang, X. Xiao, L. Zheng and C. Wan, Can. J. Chem. Eng., 2015, 93, 1594-1602.

38. D. Yong, Z. Yifeng, N. Wangyan and C. Pengpeng, Appl. Surf. Sci., 2015, 357, 1606-1612.

Chapter – 4

Investigate the photocatalytic properties of hydrothermally synthesized Cerium doped MoS_2 nanostructures under visible light irradiation

4.1. Background

In recent years, various semiconductors have been demonstrated to own the capable of utilizing sunlight to produce electrical and chemical energy for environmental production [1]. The demand for the environmental production, larger scale of industries has produce the waste water affected the living beings due to their non-biodegradability and high toxicity [2, 3]. Among them the pollution of organic is one of the most dangerous sources of the environmental contaminations they are widely used in a number of industrial wastes, such as electroplating, pigments and synthetic dyes [4-7]. To overcome the environmental protection on the global scale, the technologies of water purification has been attracting and extensive attention. Recently, semiconductor photocatalysis have been extensively utilized in the fields of solar energy conversion and waste water treatment [8]. In particular, TiO_2 as a leading photocatalyst candidate has exhibited the catalytic activites of hydrogen evolution reaction (HER) and dye degradation [9]. However, the wide band gap of 3.2 eV has limited its utilization of the visible light in the solar spectrum [10]. Moreover, the low quantum efficiency of TiO_2 induced the fast recombination of photogenerated electron hole pairs greatly limited the photocatalytic activity [11].

MoS_2 is a 2D material, with a direct band gap of 1.9 eV [12]. The MoS_2 have been extensively utilized for applications such as super solid lubricants, sensors, lithium ion batteries, dye sensitized solar cells and photocatalysis for dye degradation [13-17]. The layered structure of MoS_2 were consists of S-Mo-S units sandwiched by relatively weak

Vander Waals forced in a graphite like manner [18,19]. The direct band gap of MoS_2 makes it a visible light active photocatalyst [20]. To enhance the visible light activity of MoS_2 many efforts have been made such as increasing the surface area of MoS_2 and coupled with two semiconductors to inhibit the electron hole pair recombination rate [21]. However, the investigation by the impurity doping of rare earth metal (REM) on the photocatalytic activity of MoS_2 is limited.

Rare earth metals (REM) are active elements that have been widely added in optoelectronic devices to improve the photoelectric conversion efficiency [22]. Impurity doping of rare earth elements with proper oxidation states provides adsorption edge as well as reducing the rate of electron-hole recombination which enhance the photocatalytic activity of dye degradation [23]. It is well known that doping of the REM ions in MoS_2 is the trapping agent of the photogenerated charge carriers [24]. The REM of cerium (Ce) is an inexpensive and relatively nontoxic material, thermally stable and the adsorption edges can be obtained which improves the photocatalytic activity [25, 26]. Ce ions has both Ce^{3+} and Ce^{4+} oxidation states, which is owing to their redox potential chemistry and the oxygen storage capacity [27]. Therefore, the impurity doping of rare earth elements with MoS_2 which generates more active sites which could enhance the photocatalytic activity of MoS_2 under visible light irradiation.

Here, I synthesized Ce doped MoS_2 nanostructures by simple hydrothermal method. The Ce doped MoS_2 nanostructures were characterized by XRD, XPS, FESEM, TEM and their photocatalytic activity was evaluated by degrading methylene blue (MB) as an organic pollutant. The Ce role on the enhancement of photocatalytic activity was investigated in detail. Ce doped MoS_2 photocatalyst was exhibited excellent photocatalytic activity than pure MoS_2. The possible degradation mechanism and the separation of charge carriers between MoS_2 and Ce ions are discussed.

4.2 Experimental procedure

4.2.1 Synthesis of Ce doped MoS_2 nanostructures

The MoS_2 nanosheets were synthesized by a hydrothermal method and it was followed by the chapter I with few modifications. In a typical synthesis 0.04 M of sodium molybdate dihydrate, 0.08 M of thioacetamide and 0.04 M of citric acid were dissolved in 50 mL of deionized water under vigorous stirring for 4 h. After 4 h the transparent aqueous solution was transferred into 100 mL capacity of stainless steel autoclave. The stainless steel autoclave was maintained at 180 ºC for 24 h and then autoclave was naturally allowed to cool. The final product was collected from autoclave through centrifugation thrice with deionized water and ethanol and dried at 80 ºC for 10 h. The sample was termed as MS-1. For the synthesis of Ce doped MoS_2 nanostructures, Cerium was taken at four different concentrations and the difference are 2.5, 5, 7.5 and 10 mM have added with the mixtures of 0.04 M sodium molybdate dehydrate, 0.08 M of thioacetamide and 0.04 M of citric acid under vigorous stirring, and the hydrothermal growth was followed as described for MS-1. These samples were named as MC-2, MC-3, MC-4 and MC-5 with the concentrations of Ce as 2.5, 5, 7.5 and 10 mM, respectively.

4.2.2 Photocatalytic dye degradation

Photocatalytic degradation of methylene blue (MB) was carried out under visible light irradiation. The optical absorption of MB at 664 nm was used as monitor wavelength of photodegradation. 5 mg of MB was added to 100 mL of aqueous solution and stirred for 30 min. 50 mg of MoS_2 and MoS_2/TiO_2 photocatalyst was separately added to the above solution. To establish the absorption / desorption equilibrium, the mixed solution was stirred for 30 min. in the dark before photodegradation reaction. The visible light source of xenon lamp was placed 15 cm away from the surface of the solution. The dye degradation surveys were

conducted at an interval of 4 min. and the catalyst was isolated by centrifugation. The photodegradation percentage of MB was calculated using the following equation [28],

$$D(\%) = \frac{C_0 - C_t}{C_0} \times 100 \qquad (1)$$

where C_0 and C_t are the concentration of MB at time 0 and t (s), respectively and t is the irradiation time.

4.3 Results and discussion

Figure 4.1 shows the XRD patterns of undoped and Ce doped MoS_2 layered nanostructures. The observed diffraction peaks of the sample exhibit a pure hexagonal phase of MoS_2 which is in good agreement with standard JCPDS card no: 24-0513. Stick pattern of MoS_2 was exactly matched to the planes of (002), (100), (102), (104) and (110), respectively. None of the peaks of cerium phase are found and the cerium did not alter the MoS_2 crystalline type. However, the intensity of the diffraction peaks (002) in XRD patterns decreased, with increasing the Ce concentration from 2.5 to 10 mM. The ionic radius of Mo^{4+}, S^{2-} and Ce^{3+} seems to be 0.65, 1.84 and 1.03 Å, respectively. It was found that the ionic radius of Mo^{4+}, which was close to the rare earth ions. So, the rare earth ions maybe enter into the lattice of MoS_2 to replace Mo^{4+} while S^{2-} ionic radii was much larger than Ce^{3+} [38, 39]. No other characteristic peaks are observed in XRD analysis.

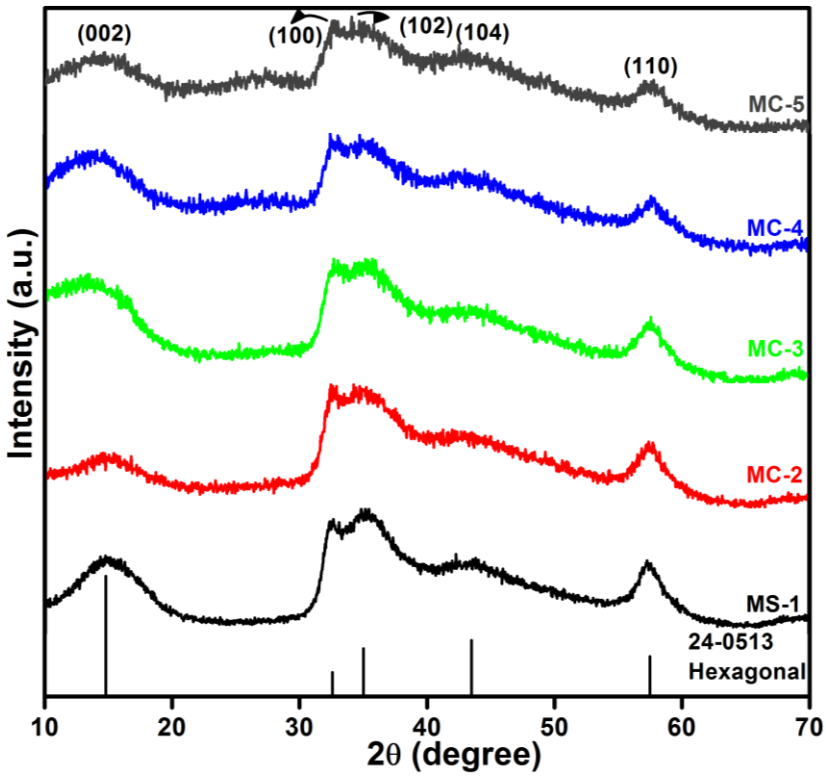

Figure 4.1. XRD patterns of pure layered MoS_2 and Ce doped MoS_2 nanosheets.

The elemental composition and chemical state of undoped and Ce doped MoS_2 was investigated using XPS as shown in Fig. 4.2 (a-e). The high resolution spectra was indicated that all the samples contain Mo, S and Ce elements and the binding states of Mo $3d_{5/2,}$ Mo $3d_{3/2}$, S $2p_{3/2}$ and S $2p_{1/2}$ were 228.23, 231.46,161.03 and 162.20 eV, respectively for sample MS-1 as shown in Fig. 4.2 (a1-a2). The binding energies of Mo $3d_{5/2,}$ Mo $3d_{3/2}$, S $2p_{3/2}$ and S $2p_{1/2}$ which were corresponded to Mo^{4+} and S^{2-} states, respectively [31]. The energy separation between Mo $3d_{5/2}$, Mo $3d_{3/2}$ were 3.1 eV and for S $2p_{3/2}$, S $2p_{1/2}$ were 1.1 eV, which is in good agreement with the literature [32, 33]. The sub-peaks at 229.12 eV and 232.26 eV are also observed, representing Mo $3d_{3/2}$ and Mo $3d_{5/2}$, respectively, indicating the presence of MoO_x (Mo^{6+} state), which might arise from surface oxidization. The Ce doped MoS_2 surface is composed of only Mo, S and Ce. The binding energies of Mo $3d_{5/2,}$ Mo $3d_{3/2}$, S $2p_{3/2}$, S $2p_{1/2}$, Ce $3d_{5/2}$ and Ce $3d_{3/2}$ were 228.20, 231.40, 161.15, 162.39 and 883.82 eV,

respectively. Whereas, the Ce $3d_{3/2}$ was deconvoluted into two peaks at the center of 903.07 and 919.38 eV for sample MC-2 as shown in Fig. 4.2b (b1-b3). Fig. 4.2c (c1-c3), Fig. 4.2d (d1-d3) and Fig. 4.2e (e1-e3) shows the binding state and the binding energies of Mo $3d_{5/2,}$ Mo $3d_{3/2}$, S $2p_{3/2}$, S $2p_{1/2}$ and Ce $3d_{5/2}$ were observed at 228.20, 231.45, 161.10, 162.35, 884.25 eV for sample MC-3, 228.18, 231.44, 161.13, 162.30 and 884.33 eV for sample MC-4, 228.20, 231.55, 161.10, 162.34 and 884.20 eV for sample MC-5, respectively. Moreover, the Ce $3d_{3/2}$ was deconvoluted into two peaks at the center of 902.07 and 917.70 eV for sample MC-3, 901.60 and 917.85 eV for sample MC-4, 902.60 and 920.68 eV for sample MC-5, respectively. It is clearly observed that a slight shift in the binding energy have been observed with increase in the concentration of Ce from MC-2 to MC-5. The binding energies of Mo $3d_{5/2,}$ Mo $3d_{3/2}$, S $2p_{3/2}$ and S $2p_{1/2}$ were shifted about 0.20 eV when compared to undoped MoS_2. Whereas, Ce $3d_{5/2}$ and Ce $3d_{3/2}$ were shifted about 2 eV. This significant peak shift was observed due to the formation of redox couple Ce^{3+}/ Ce^{4+} based on oxidizing and reducing conditions, and it could easily form oxygen vacancies with relatively high mobility of bulk oxygen species [34].

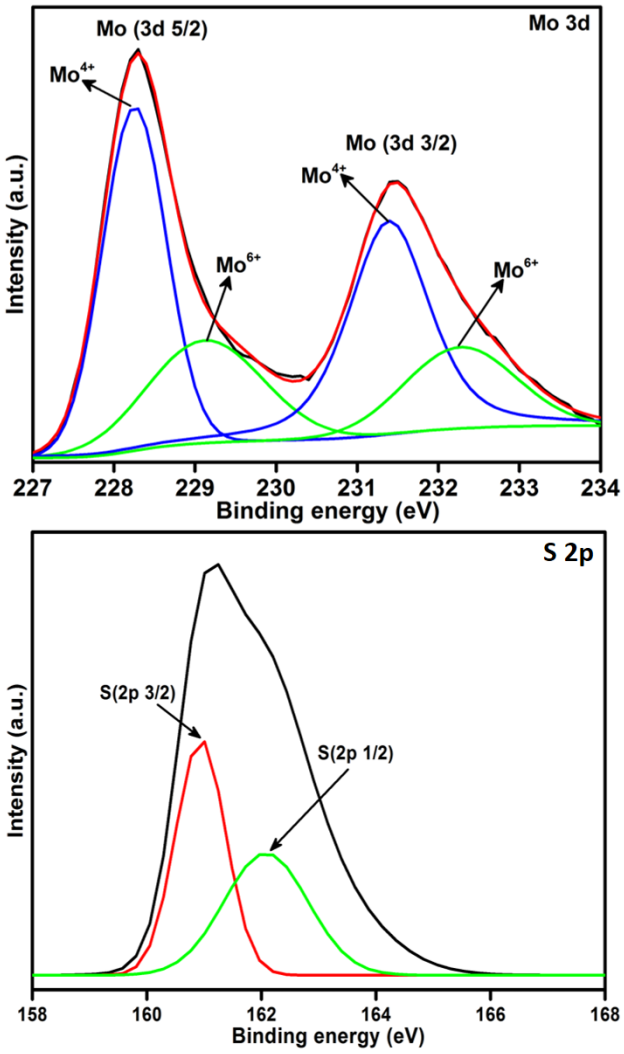

Figure 4.2 (a). XPS spectra of pure layered MoS_2 (MS-1) nanosheets.

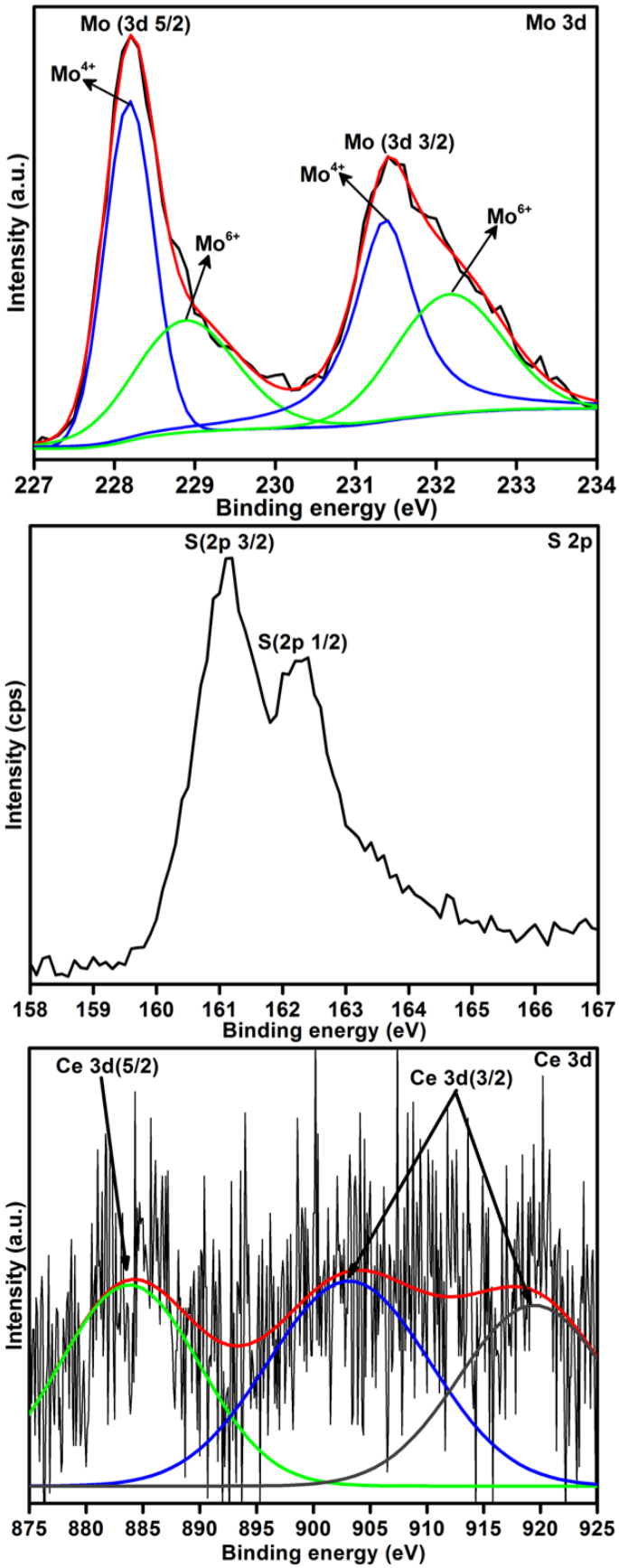

Figure 4.2 (b). XPS spectra of Ce doped layered MoS_2 (MC-2) nanosheets.

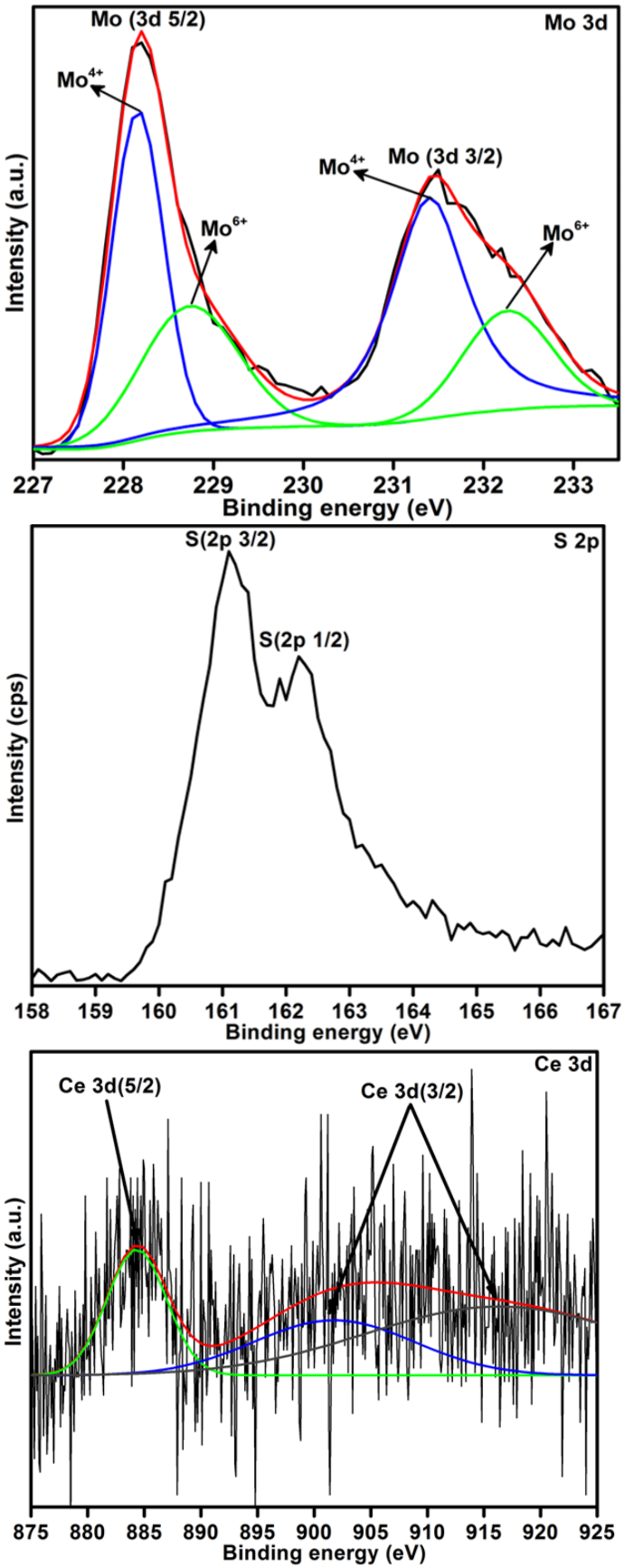

Figure 4.2 (c). XPS spectra of Ce doped layered MoS_2 (MC-3) nanosheets.

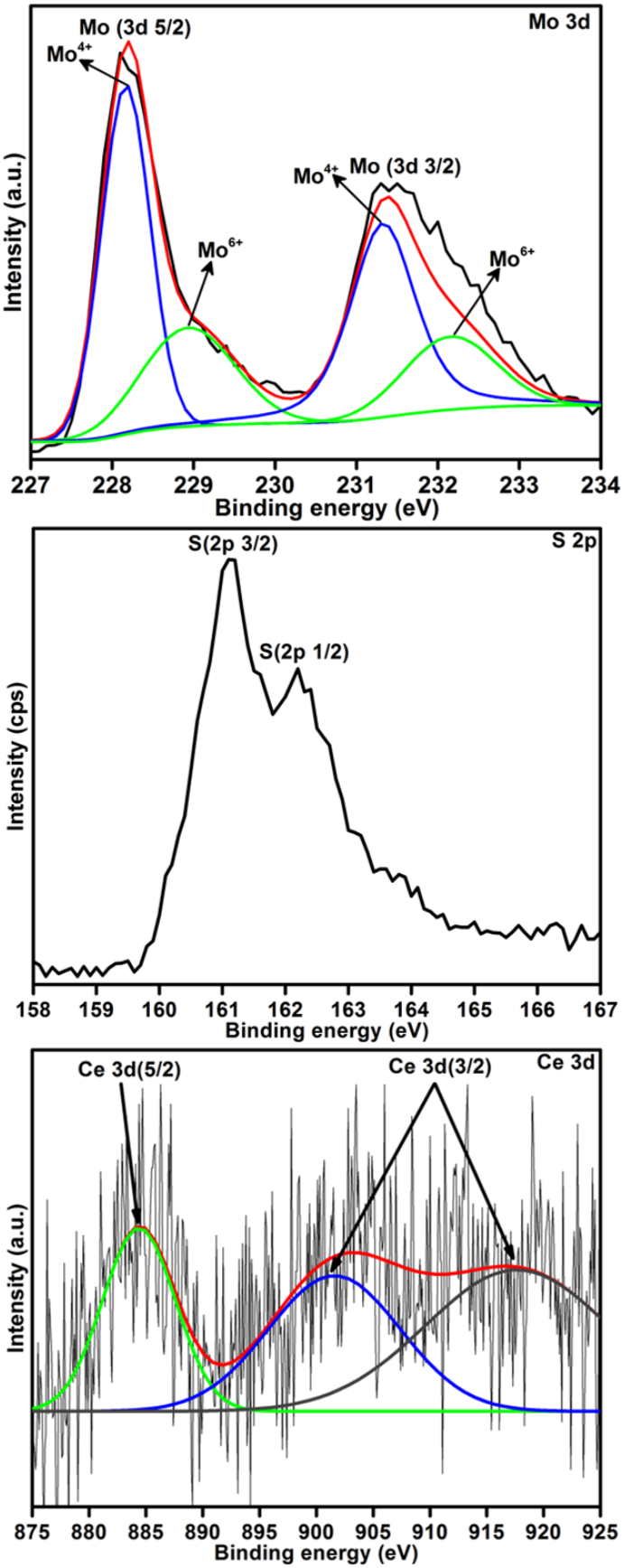

Figure 4.2 (d). XPS spectra of Ce doped layered MoS_2 (MC-4) nanosheets.

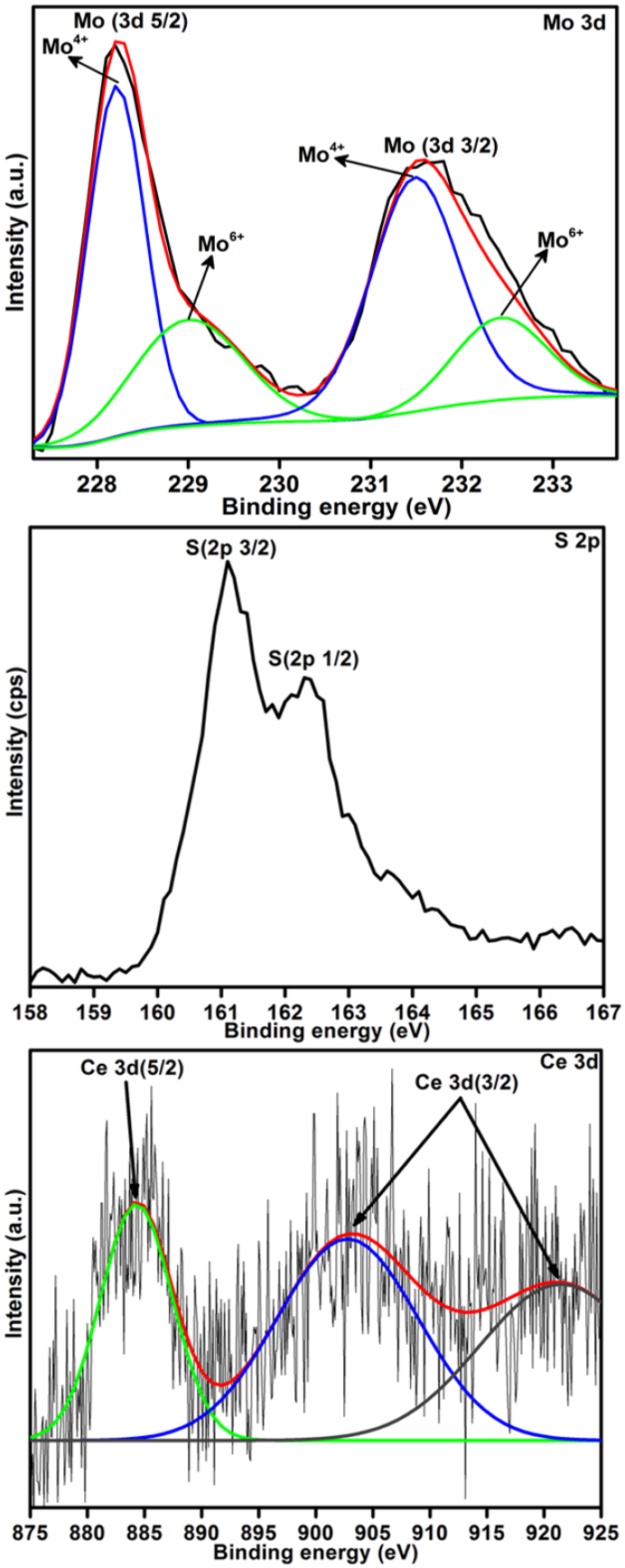

Figure 4.2 (e). XPS spectra of Ce doped layered MoS_2 (MC-5) nanosheets.

Figure 4.3 shows the FESEM and TEM images of pure MoS_2 and Ce doped MoS_2 nanostructures. It was found that the pure MoS_2 (MS-1) had the monodispersed layered nanosheets as shown in Fig. 4.3 (a). Whereas, Figure 4.3 (b and c) shows the low and high magnification TEM images with the lattice spacing of 0.61 nm which is corresponded to the (002 plane) XRD data. The addition of Ce in MoS_2 appears to affect the morphology and size of the nanostructures. Figure 4.3 (d) shows the FESEM images of Ce doped MoS_2 nanostructures and Fig. 4.3 (e, f) were corresponding low and high magnification TEM images, respectively. It was observed that the Ce doped MoS_2 (MC-2) was slightly agglomerated compared to undoped MoS_2. Figure 4.3 (g, j, m) shows the Ce doped MoS_2 FESEM images of sample MC-3, MC-4 and MC-5, respectively. Moreover, Figure 4. 3 (h, k, n) and (j, l, o) were low and high magnification TEM images of sample MC-3, MC-4 and MC-5, respectively. It was observed that with increase in the Ce concentration, the nanostructure was highly agglomerated between each layered nanosheets. The agglomeration might attribute due to synergetic and nucleation effect between MoS_2 and Ce nanostructures. According to the results in morphological analysis, the incorporation of Ce ions had strong interaction between nanosheets. EDS analysis of sample MC-5 was shown in Fig. 4.4 EDS analysis was confirmed that the all elements such as, Mo, S and Ce were presented in synthesized sample. The chemical composition of pure MoS_2 and Ce doped MoS_2 nanosheets were homogeneous as shown in Table 4.1.

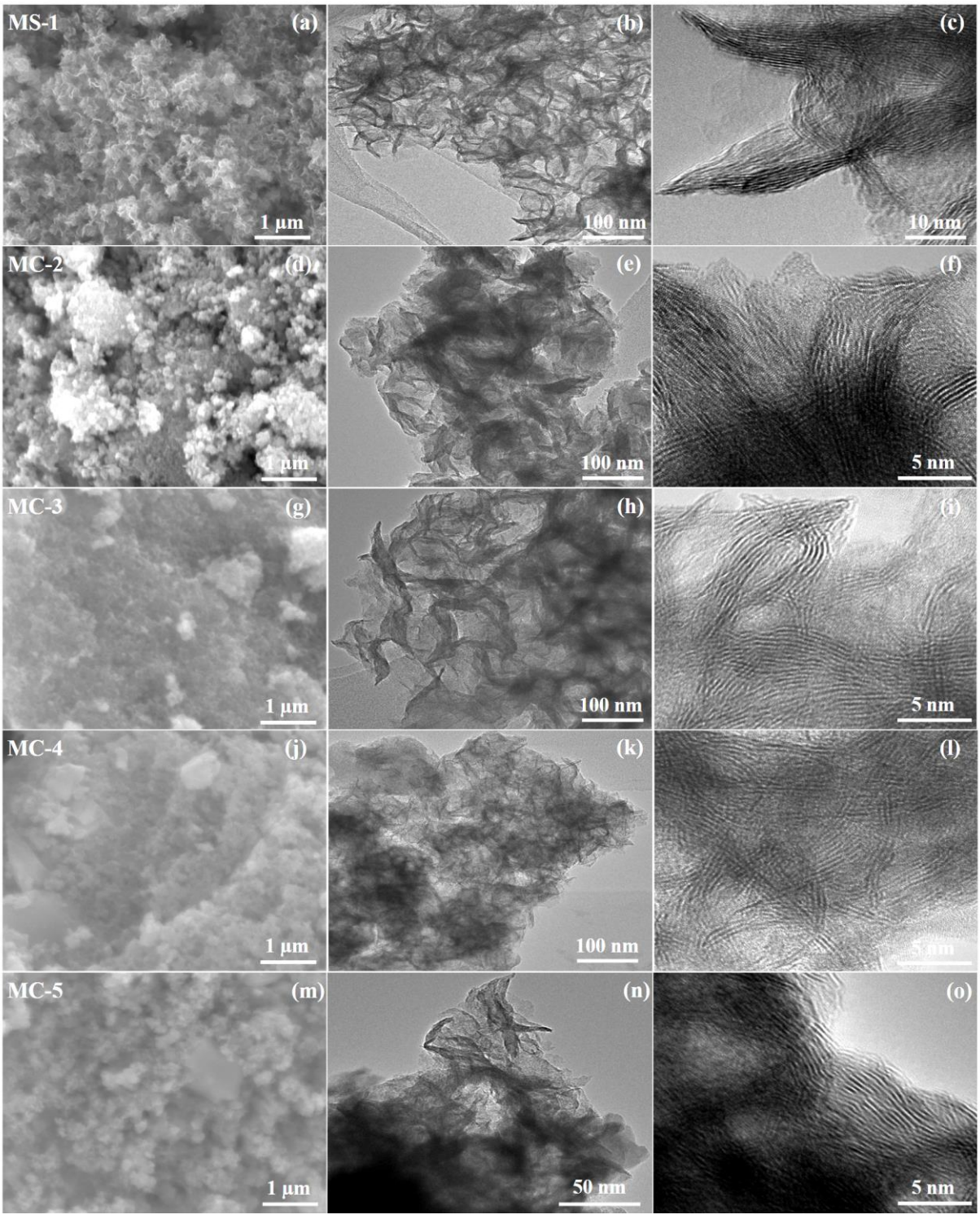

Figure 4.3. (a, d, g, j, m) FESEM, (b, e, h, k, n) TEM and (c, f, I, l, o) HRTEM images of sample MS-1 to MC-5.

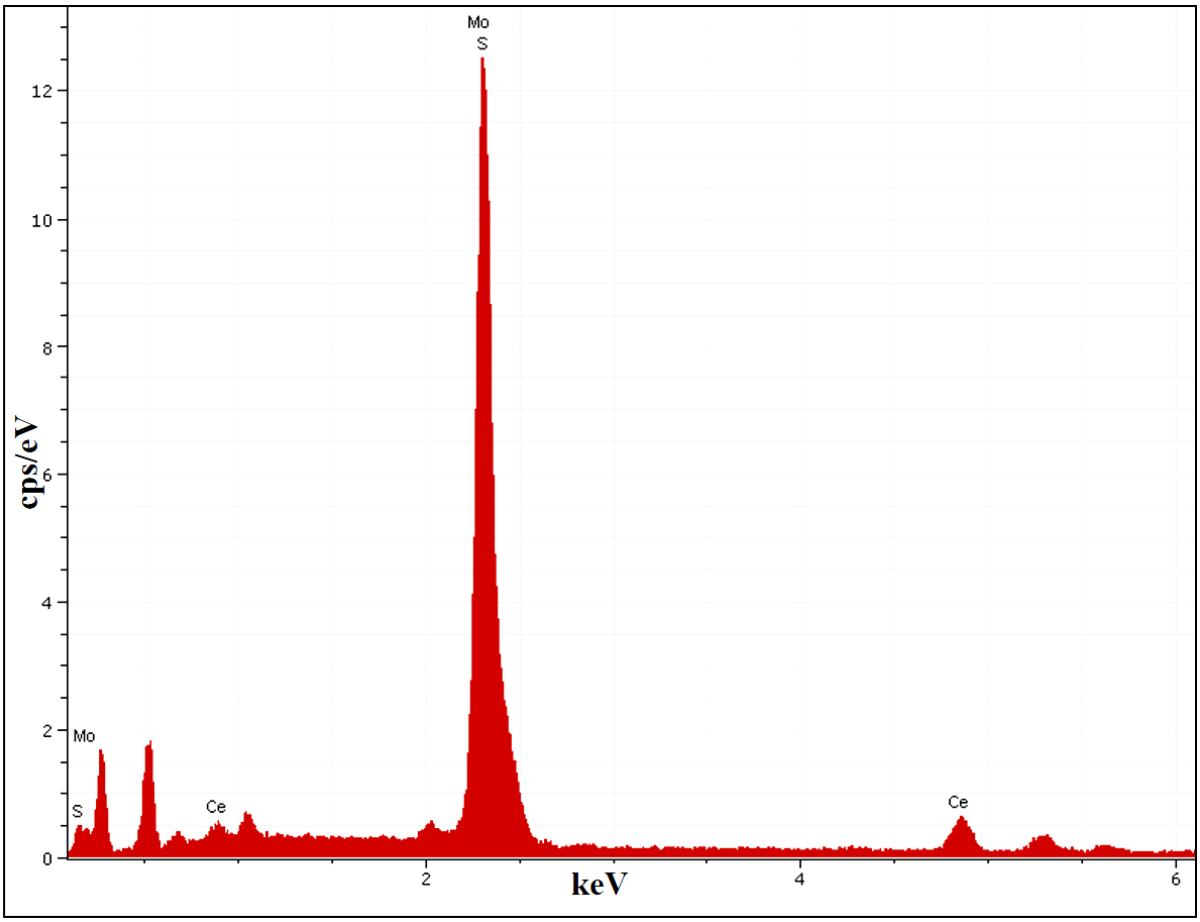

Figure 4.4. EDAX spectra of Ce doped layered MoS_2 (MC-5) nanosheets.

Element	MS-1	MC-2	MC-3	MC-4	MC-5
Mo	44.04	41.63	40.23	36.47	34.56
S	55.96	56.89	50.77	50.58	49.47
Ce	-	1.48	9	12.95	15.97

Table 4.1. Atomic percentage of pure and Ce doped layered MoS_2 nanosheets according to the concentration of Ce.

4.3.1 Photocatalytic activity

The photocatalytic activity of undoped and Ce doped MoS_2 nanostructures were performed using MB as a model pollutant under visible light irradiation. Figure 4.5 show the UV absorption spectra of undoped and doped MoS_2 nanostructures with different degradation time. The characteristic absorption peak of MB at 664 nm was chosen to monitor the photocatalytic degradation of MB. Figure 4.5(a) shows the UV absorption spectra of undoped (MS-1) sample with the degradation percentage of 98.69 % for 28 min of irradiation. Figure 4.5 (b-e) shows the UV absorption spectra of Ce doped MoS_2 with irradiation time of 20 min for sample MC-2, 12 min for sample MC-3, 32 min for sample MC-4 and 36 min for sample MC-5, respectively. In the addition of Ce with different concentration in the layered structure significantly enhanced the photocatalytic activity under visible light irradiation. The irradiation time was decreased to 20, 12 for samples MC-2, MC-3 and then the time was increased to 32, 36 for samples MC-4 and MC-5, respectively. The degradation of MB time was increased for sample MC-4 and MC-5 due to the agglomeration of nanosheets which affected the activity. Figure 4.5 (f) shows the degradation percentage of samples MC-2 (b), MC-3 (c), MC-4 (d), MC-5 (e) were 98.82, 99.39, 98.75 and 98.73 %, respectively. Among all the synthesized samples, MC-3 showed the enhanced photocatalytic activity because the Ce ions acted as electron acceptor and promoted the photocatalytic dye degradation. Moreover, the layered MoS_2 nanosheets has strong absorption ability towards organic dye molecules. The efficient charge carrier transfer between MoS_2 and Ce ions which enhanced the photocatalytic activity.

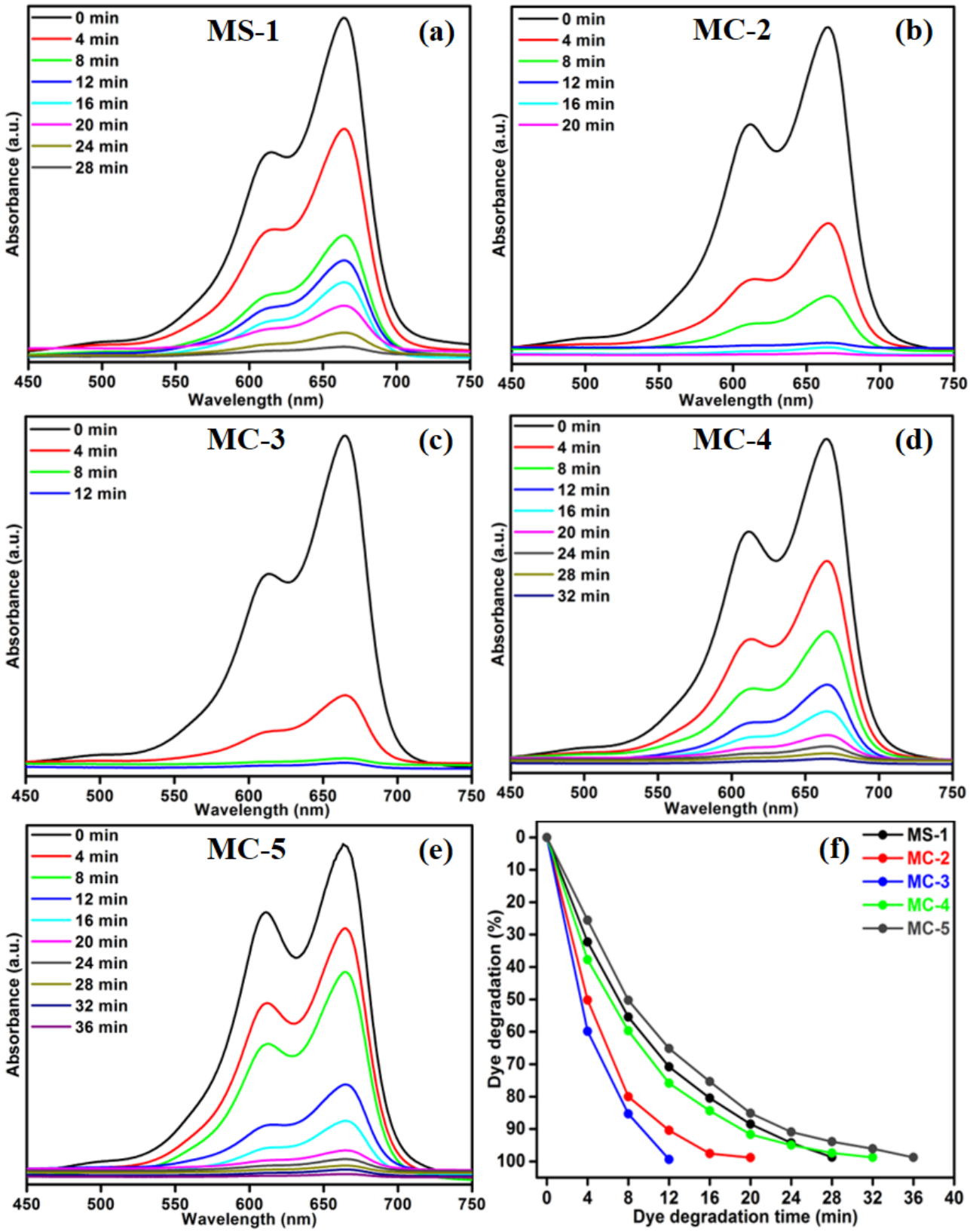

Figure 4.5. UV absorbance spectra of MB samples MS-1 (a), MC-2 (b), MC-3 (c), MC-4 (d), MC-5 (e) and MB degradation of samples MS-1, MC-2, MC-3, MC-4 and MC-5 Time (min) vs dye degradation (%) (f).

To understand which of the active species has the main role in the degradation of MB under visible light irradiation were conducted in the presence of different scavengers as shown in Fig. 4.6. The hydroxyl radicals ($^{\bullet}OH$) and superoxide anions ($O_2^{-\bullet}$) are possible reactive species for the degradation of organic pollutants during photocatalysis. EDTA-2Na was used as a hole (h^+) scavenger while N_2 was used as an electron (e^-) acceptor, respectively [35, 36]. The high purity gas of N_2 was continuously purged throughout the reaction container under ambient condition. The high purity N_2 gas which eliminated the oxygen content from the solution thereby prevented the $O_2^{-\bullet}$ formation. The degradation percentage was calculated to be 59.56 % when N_2 gas used as a scavenger. This conformed that superoxide anions played a minor role in the photocatalytic degradation of MB. When the EDTA ($^{\bullet}OH$ scavenger) added into the solution, the degradation of MB slowed down and the percentage of degradation was 35.79 % instead of 99.39 % in the scavenger free catalyst. Therefore, it is clearly illustrated that photoinduced holes (h^+) are one of the main reactive species while the photogenerated electrons (e^-) and O_2 also contributed in certain extend for the degradation of MB in the Ce doped MoS_2 photocatalyst.

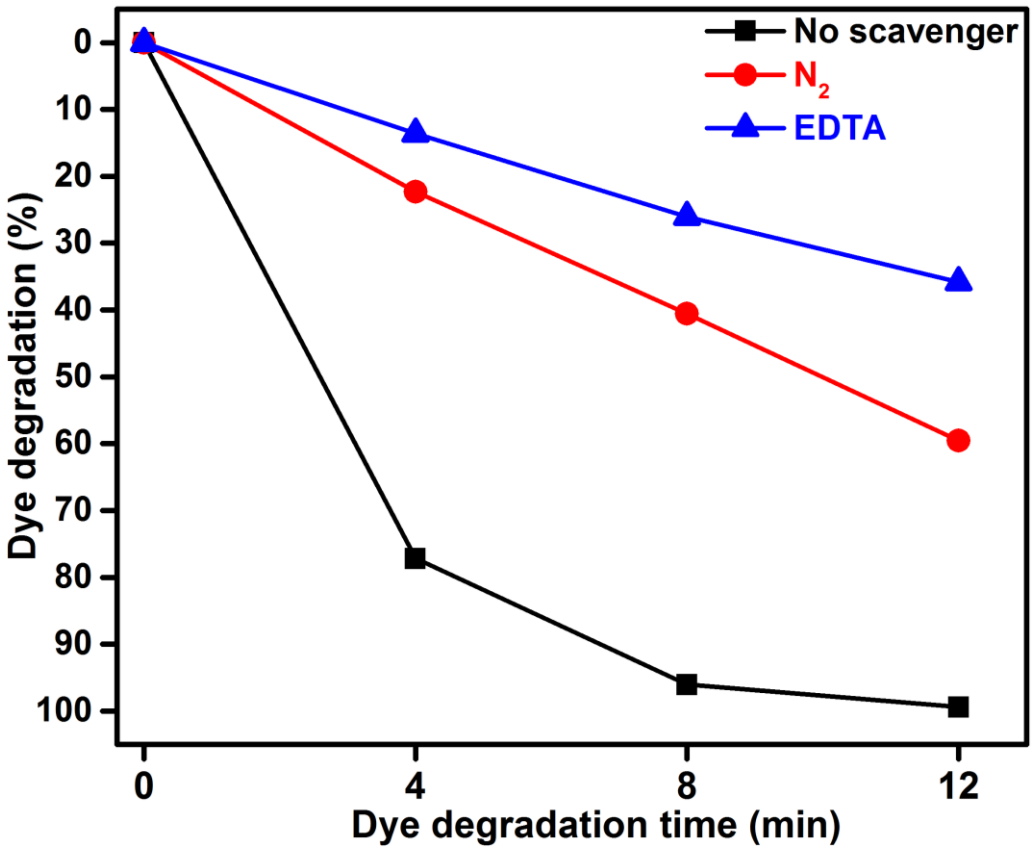

Figure 4.6. MB degradation using Ce doped MoS_2 (MC-3) nanosheets without scavenger and with scavengers under visible light irradiation.

The kinetic analysis for the degradation of MB is shown in Fig. 4.7. To investigate whether the process obeyed pseudo first order model a plot between $ln(C_0/C_t)$ versus irradiation time as shown in Figure. The apparent rate constants (K_{app}), corresponding correlation coefficients (R^2) and maximum dye degradation in presence of undoped and Ce doped MoS_2 nanostructures are shown in Table 4.2. The apparent rate constants were 0.1311, 0.2302, 0.427, 0.1344 and 0.1301 min^{-1} for sample MS-1, MC-2, MC-3, MC-4 and MC-5, respectively. The apparent rate constant value increased with increase the concentration of Ce from 0.1311 to 0.427 min^{-1} for sample MS-1 to MC-3. Further increase of the Ce concentration apparent rate constant value decreased to 0.1301 min^{-1} for sample MC-5. It

shows that apparent rate constant (plot of $ln(C_0/C_t)$ versus irradiation time) was about 4 times higher than the undoped catalyst.

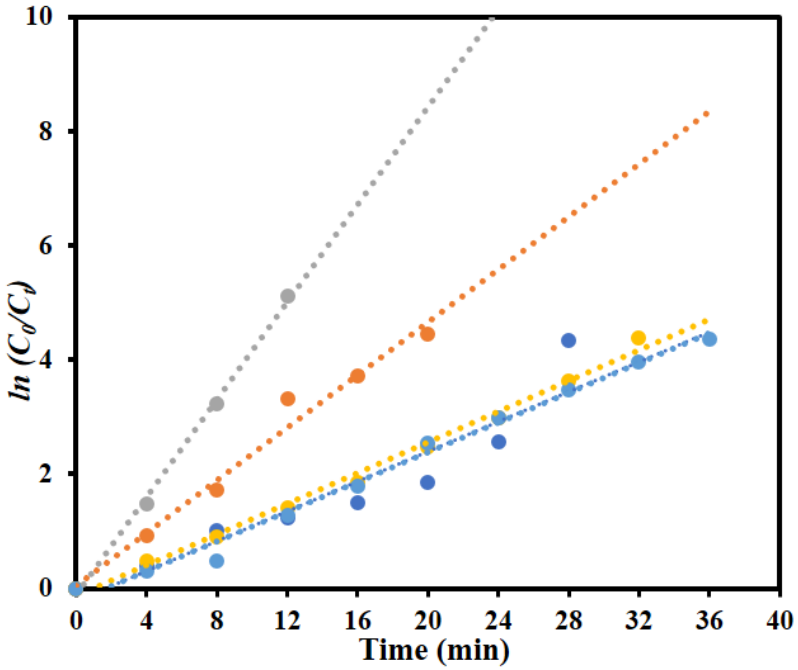

Figure 4.7. Kinetic plot of ln(C_0/C_t) as a function of time (min) for the degradation of MB.

Sample code	K_{app} (MoS_2)	R^2	Maximum degradation (%)	Time taken for maximum degradation (min)
MS-1	0.1311	0.8876	98.69	28
MC-2	0.2302	0.9778	98.82	20
MC-3	0.4270	0.9972	99.39	12
MC-4	0.1344	0.9933	98.75	32
MC-5	0.1301	0.9905	98.73	36

Table. 4.2. Observed pseudo-first-order rate constants, R^2 values, maximum degradation (%) and time required for maximum degradation by pure and Ce doped MoS_2 nanosheets.

Based on the above photocatalytic degradation result, we propose the possible mechanism for the Ce doped MoS_2 as photocatalysts [37]:

$$MoS_2\text{-}Ce^{3+} + h\nu \rightarrow MoS_2\,(h^+)/Ce^{3+}\,(e^-) \quad (1)$$

$$Ce^{3+} + O_2 + e^- \rightarrow \bullet O_2^- \quad (2)$$

$$H_2O + h^+ \rightarrow \bullet OH + H^+ \quad (3)$$

$$\bullet O_2^- + H_2O \rightarrow \bullet HO_2 + OH^- \quad (4)$$

$$\bullet HO_2 + H_2O \rightarrow H_2O_2 + \bullet OH \quad (5)$$

$$H_2O_2 \rightarrow 2\bullet OH \quad (6)$$

$$\bullet OH + MB \rightarrow CO_2 + H_2O + NO^-_3 + NH^+_4 + Cl^- \quad (7)$$

Figure 4.8 shows the degradation of sample MC-3 to determine the stability and reusability of photocatalyst under visible light irradiation. The sample MC-3 was reused for 4 successive runs of photodegradation of MB and after each run the catalyst was speared and set back to its initial value. The MB degradation was calculated to be 96.42, 91.68, 87.18 and 81.15, after 4 runs, respectively. The efficiency of the MC-3 catalyst did not declined significantly. The obtained result suggested that the catalyst had good chemical stability and sustainability for long time. Furthermore, the catalyst of MC-3 phase structure was characterized using XRD after four cycles as shown in Figure 9. It conformed that the phase structure of MoS_2 showed no change after four cycles when compared to its as-prepared sample.

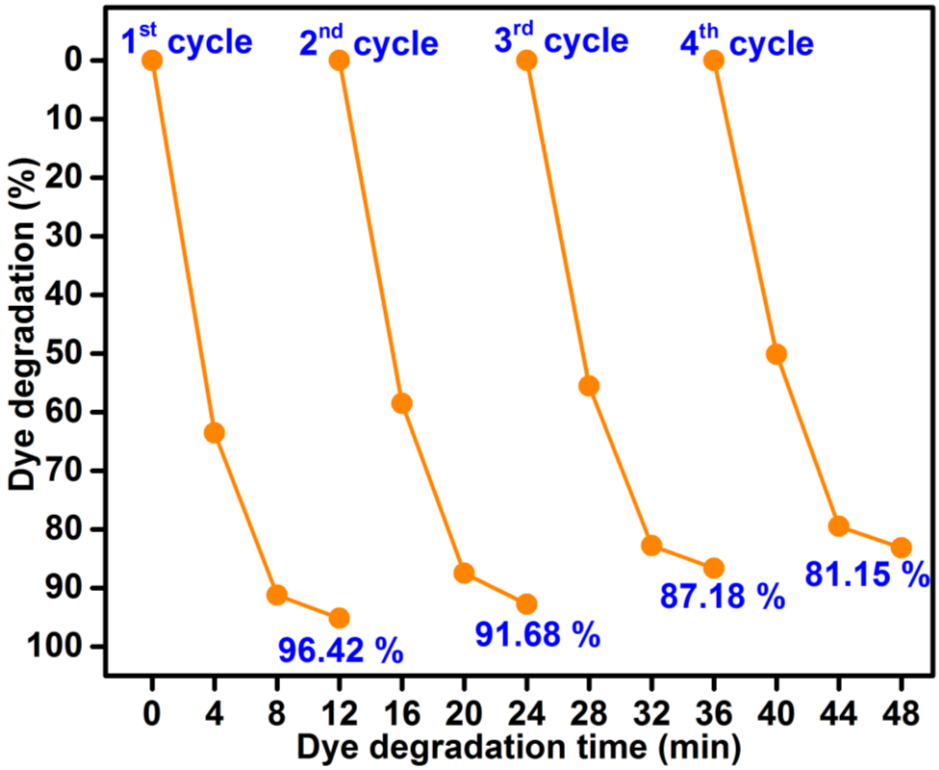

Figure 4.8. Reusability of sample MC-3 photocatalyst under visible light irradiation.

The schematic diagram illustrates the energy band structure and the charge transfer mechanism between MoS_2 and Ce was shown in Figure 4.9. Under visible light irradiation, the photoinduced electrons (e^-) are excited from valance band to its conduction band, leaving behind holes (h^+) in the valance band. The photogenerated holes react with either water (H_2O) or hydroxyl ions (OH^-) adsorbed by the catalyst surface to produce hydroxyl radicals (•OH). Meanwhile, the photoinduced electrons were trapped from the conduction band of MoS_2 to Ce^{3+} sites, which are subsequently transferred to the adsorbed O_2. The Ce trapped electrons react with oxygen (O_2) to form superoxide radicals ($•O_2^-$). Consequently, both •OH and $•O_2^-$ radicals can decompose the organic compounds to produce CO_2, H_2O and other inorganic compounds as a harmless product. It indicated that all the photoinduced charge carriers are lost in the recombination process which enhanced photocatalytic dye degradation under visible light irradiation.

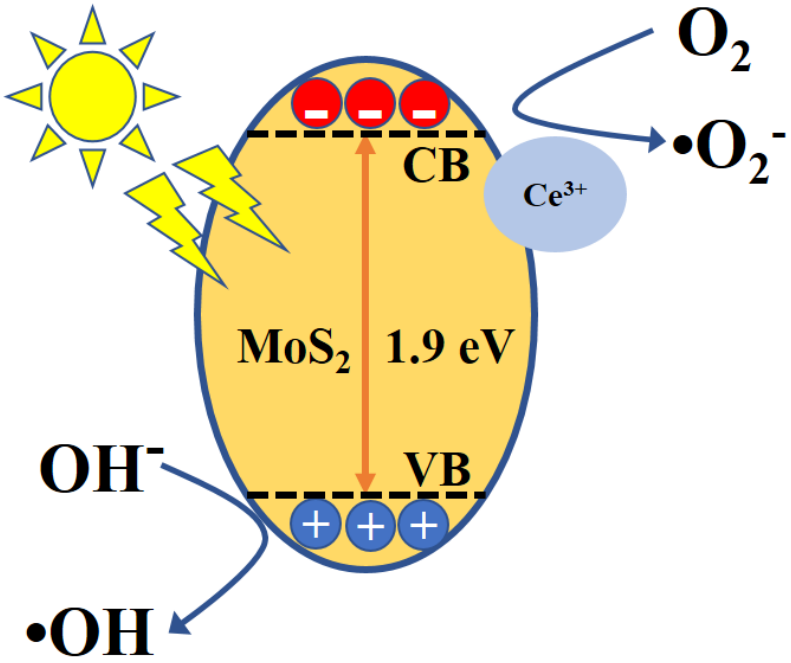

Figure 4.9. Schematic representation of charge transfer mechanism for Ce doped MoS_2 photocatalysis.

4.4. Conclusion

In summary, the undoped and Ce doped MoS_2 layered nanostructures were successfully prepared by hydrothermal method. Structural analysis revealed the formation of hexagonal phase with good crystalline nature. The profound effect of morphology has been observed from monodispersed nanosheets to agglomerated nanostructures have been observed with the addition of Ce doping. The rare earth doped MoS_2 photocatalyst exhibited higher photocatalytic activity compared to undoped sample. The significant photocatalytic enhancement of Ce doped MoS_2 nanostructures attributed to the specific electrons transfers. The maximum degradation efficiency was attained for sample MC-3 nanostructure photocatalyst in 12 min and the degradation percentage is calculated to be 99.39 %. The obtained result was three times higher than the pure MoS_2. The scavenger experiment was confirmed that photogenerated hydroxyl radicals played an important role in the degradation of organic pollutant.

References

1. G. A. Muller, J. B. Cook, H. Kim, S. H. Tolbert and B. Dunn, Nano. Lett., 2015, 15, 1911-1917.
2. Y. Zhang, Q. Li, R. Tang, Q. C. Hu, L. Sun and J. P. Zhai, Appl. Catal. B. Environ., 2009, 92, 351-356.
3. A. Mills, L. Punte and M. Stephan, J. Photochem. Photobiol. A., 1997, 108, 1-35.
4. Y. Q. Wang, B. F. Zou, T. Gao, X. P. Wu, S. Y. Lou and S. M. Zhou, J. Mater. Chem., 2012, 22, 9034-9040.

5. H. Abu Hasan, S.R.S. Abdullah, N.T. Kofli, S.K. Kamarudin, J. Environ. Manag., 2012, 111, 34–43.

6. V. Vinodhini, N. Das and V. Vinodhini, Int. J. Environ. Sci. Technol., 2010, 7, 85–92.

7. E.I. El-Shafey, J. Hazard. Mater., 2010, 175, 319–327.

8. O. M. Alfano, D. Bahnemann, A. E. Cassano, R. Dillert and R. Goslich, Catal. Today., 2000, 58, 199-230.

9. A. Fujishima and K. Honda, Nature, 1972, 238, 37 - 38.

10. H. G. Yang, C. H. Sun, S. Z. Qiao, J. Zou, G. Liu, S. C. Smith, H. M. Cheng and G. Q. Lu, Nature, 2008, 453, 638 - 641.

11. L. Zheng, S. Han, H. Liu, P. Yu and X. Fang, Small, 2016, 12, 1527 - 1536.

12. A. Splendiani, L. Sun, Y. Zhang, T. Li, J. Kim, C. Yung, G. Galli and F. Wang, Nano Lett., 2010, 10, 1271 - 1275.

13. M. R. Hilton, R. Bauer, S. V. Didziulis, M. T. Dugger, J. M Keem and J. Scholhamer, Surf. Coat. Technology., 1992, 53, 13-23.

14. Q. He, Z. Zheng, Z. Yin, H. Li, S. Wu, X. Huang and, H. Zhang, Small, 2012, 8, 2994-2999.

15. S. Ding, D. Zhang, J. S. Chen and X. W. Lou, Nanoscale, 2012, 4, 95-98.

16. G. Yue, J. Wu, Y. Xiao, M. Huang, J. Lin and J. Y. Lin, J. Mater. Chem. A, 2013, 1, 1495-1501.

17. W. Zhou, Z. Yin, Y, Du, X. Huang, Z. Zeng, Z. Fan, H. Liu, J. Wang and H. Zhang, Small, 2013, 9, 140-147.

18. Y. G. Li, H. L. Wang, L. M. Xie, Y. Y. Liang, G. S. Hong and H. J. Dai, J. Am. Chem. Soc., 2011, 133, 7296 - 7299.

19. I. Song, C. Park and H. Cheul Choi, RSC Adv., 2015, 5, 7495 - 7514.

20. T. S. Li and G. L. Galli, J. Phys. Chem.C., 2007, 111, 16192 - 16196.

21. H. L. Wang, L. S. Zhang, Z. G. Chen, J. Q. Hu, S. J. Li and Z. H. Wang, Chem. Soc. Rev., 2014, 43, 5234 - 5244.

22. T. A. Yourre, L. I. Rudaya, N. V. Klimova and V. V. Shamanin, Semiconductor, 2003, 37, 807-815.

23. Z. M. El-Bahy, A. A. Ismail and R. M. Mohamed, J. Hazard. Mater., 2009, 166, 138-143.

24. J. C. Sin, S. M. Lam, K. T. Lee and A. R. Mohamed, J. Mol. Catal. A: Chem., 2015, 409, 1-10.

25. A. S. Weber, A. M. Grady and R. T. Koodali, Catal. Sci. Tech., 2012, 2, 683-693.

26. Y. Cong, B. Tian and J. Zhang, Appl. Catal., B, 2011, 101, 376–381.

27. T. Tong, J. Zhang, B. Tian, F. Chen, D. He and M. Anpo, J. Colloid Interface Sci., 2007, 315, 382-388.

28. S. Harish, J. Archana, M. Navaneethan, A. Silambarasan, K. D. Nisha, S. Ponnusamy, C. Muthamizhchelvan, H. Ikeda, D. K. Aswal and Y. Hayakawa, RSC Adv., 2016, 6, 89721 - 89731.

29. S. Sakthivel, M. V. Shankar, M. Palanichamy, B. Arabindoo, D. W. Bahnemann and V. Murugesan, Water Res., 2004, 38, 3001-3008.

30. M. Kitaura, S. Tanaka, M. Itoh, A. Oknishi, H. Kominami and K. Hara, J. Lumin., 2016, 172, 243-248.

31. Y. Yan, B. Xia, N. Li, Z. Xu, A. Fisher and X. Wang, J. Mater. Chem. A, 2015, 3, 131 - 135.

32. F. A. Deorsola, N. Russo, G. A. Blengini and D. Fino, Chem. Eng. J., 2012, 195-196, 1-6.

33. J. Baltrusaitis, Courtney R. Usher and Vicki H. Grassian, Phys. Chem. Chem. Phys., 2007, 9, 3011-3024.

34. M. Yousefi, M. Amiri, R. Azimirad and A. Z. Moshfegh, J. Electroanal. Chem., 2014, 661, 106-112.

35. L. Peitao, L. Yonggang, Y. Weichun, M. Ji and G. Daqiang, Nanotechnology, 2016, 27, 225403 - 225410.

36. G. Gong, Y. Liu, B. Mao, B. Wang, L. Tan, D. Li, Y. Liu and W. Shi, RSC Adv., 2016, 6, 99023 - 99033.

37. Z. Fan, F. Meng, J. Gong, H. Li, Z. Ding and B. Ding, J. Mater. Sci. - Mater. Electron., 2016, 27, 11866-11872.

Chapter 5

Summary and Future work

5.1. Summary

Hydrothermal method was involved for the synthesis of 2D layered MoS_2 nanostructures. The growth condition of MoS_2 nanostructures were optimized. The optimized conditions such as growth temperature, concentration of the precursors and growth period were controlled to obtain desired morphology of 2D layered MoS_2 nanostructures. Functional properties of the prepared 2D layered MoS_2 nanostructures were characterized by X-ray diffraction patterns, UV-visible spectroscopy, X-ray photoelectron spectroscopy, field emission scanning electron microscope and transmission electron microscope. The synthesized 2D layered MoS_2 nanostructures were used to degrade the organic pollutant of methylene blue under visible light irradiation.

A facile hydrothermal method was involved to synthesize 2D layered MoS_2 nanostructures using citric acid as capping ligand. The effect of citric acid on the structural, optical and morphological properties of the 2D layered MoS_2 nanostructures were investigated. The sample prepared for the concentration of citric acid at 0.04 M (CA3) was significantly directed the formation of layered nanosheets. The photocatalytic activity of dye degradation for organic pollutant under visible light irradiation was investigated. It was found that the maximum dye degradation of 99.30 % was achieved after 24 min of visible light irradiation for sample CA3. The effect of pH on the 2D layered MoS_2 nanosheets was studied, and 96 % methylene blue degradation was observed at pH 12 after 2 min of visible light irradiation. The use of 2D layered MoS_2 nanostructures photocatalyst had potential to degrade the organic pollutant under visible light irradiation.

2D layered MoS_2 nanostructures and MoS_2/TiO_2 nanocomposites were synthesized by the hydrothermal method. The effect of TiO_2 concentrations on the formation of MoS_2/TiO_2 composites and functional properties were investigated. The photocatalytic activity of dye degradation for organic pollutant under visible light irradiation was investigated. It was found that the maximum dye degradation of 99.33 % was achieved after 12 min of visible light irradiation for sample S4. The heterostructure photocatalyst was significantly suppressed the charge carrier recombination. The use of MoS_2/TiO_2 photocatalyst was effectively transferred the charge carriers between two semiconductors.

The rare earth metal of Ce doped 2D layered MoS_2 nanostructures were prepared by hydrothermal method. The effect of Ce ions in 2D layered MoS_2 nanostructures functional properties and photocatalytic properties of dye degradation were investigated. It was found that the methylene blue absorption peak at 664 nm was completely disappeared after 12 min with 99.39 % of degradation under visible light irradiation at Ce concentration of 5 mM. The Ce ions in 2D layered MoS_2 nanostructures was effectively suppressed the electron-hole pair recombination. The use of Ce ions in photocatalytic activity which is accept the electrons and promote the dye degradation under visible light irradiation.

5.2. Future work

In the present work, 2D layered MoS_2 nanostructures and nanocomposites were synthesized and investigated their functional properties. The photocatalytic degradation of organic pollutant was studied under visible light irradiation.

In future, we aimed to synthesis 2D layered MoS_2 nanostructures with various nanocomposites through different preparation methods such as thermal decomposing method and hot injection method. The structural and morphological properties will be characterized using several techniques such as XRD, XPS, UV, FESEM and TEM.

The synthesized 2D layered MoS_2 nanostructures and nanocomposites will be used as photocatalysts in the photocatalytic degradation of organic pollutant under visible light irradiation. In addition, various dyes such as Rhodamine B, Methyl Orange and Azo dye will be used as model pollutant.

List of publications and conferences

(A) Journal publications

1) **M. Sabarinathan**, S. Harish, J. Archana, M. Navaneethan, H. Ikeda and Y. Hayakawa, (2017) "Highly efficient visible light photocatalytic activity of MoS_2 -TiO_2 mixtures hybrid photocatalyst and functional properties" *RSC Adv.* (Accepted manuscript).

2) **M. Sabarinathan**, S. Harish, J. Archana, M. Navaneethan, H. Ikeda and Y. Hayakawa, (2016) "Controlled exfoliation of monodispersed MoS_2 layered nanostructures by a ligand-assisted hydrothermal approach for the realization of ultrafast degradation of an organic pollutant" *RSC Adv.* 6:109495-109505.

(B) Other publications (Journal)

1) **M. Sabarinathan**, M. Omprakash, S. Harish, M. Navaneethan, J. Archana, S. Ponnusamy, H. Ikeda, T. Takeuchi, C. Muthamizhchelvan and Y. Hayakawa, (2017) "Enhancement of powerfactor by energy filtering effect in hierarchical $BiSbTe_3$ nanostructures for thermoelectric applications" *Appl. Surf. Sci.* (Article in press).

2) S. Harish, **M. Sabarinathan**, J. Archana, M. Navaneethan, S. Ponnusamy, C. Muthamizhchelvan, H. Ikeda, and Y. Hayakawa, (2017) "Functional properties and enhanced visible light photocatalytic performance of V_3O_4 nanostructures decorated ZnO nanorods" *Appl. Surf. Sci.* (Article in press).

3) S. Harish, **M. Sabarinathan**, J. Archana, M. Navaneethan, K. D. Nisha, S. Ponnusamy, Vinay Gupta, C. Muthamizhchelvan, D. K. Aswal, H. Ikeda, and Y. Hayakawa, (2017) "Synthesis ZnO/SrO nanocomposites for enhanced photocatalytic activity under visible light irradiation" *Appl. Surf. Sci.* (Article in press).

4) S. Harish, J. Archana, **M. Sabarinathan**, M. Navaneethan, K. D. Nisha, S. Ponnusamy, C. Muthamizhchelvan, H. Ikeda, D. K. Aswal and Y. Hayakawa, (2017) "Controlled structural and compositional characteristic of visible light active ZnO/CuO photocatalyst for the degradation of organic pollutant" *Appl. Surf. Sci.* (Article in press).

5) J. Archana, S. Harish, **M. Sabarinathan**, M. Navaneethan, S. Ponnusamy, C. Muthamizhchelvan, M. Shimomura, H. Ikeda, D. K. Aswal and Y. Hayakawa, (2016)

"Highly efficient dye-sensitized solar cell performance from template derived high surface area mesoporous nanospheres" *RSC Adv.* 6:68092-68099.

6) M. Omprakash, M. Arivanandhan, **M. Sabarinathan**, T. Koyama, Y. Momose, H. Ikeda, H. Tatsuoka, D. K. Aswal, S. Bhattacharya, Y. Inatomi, and Y. Hayakawa, (2016) "Vertical gradient solution of N-type $Si_{0.73}$ $Ge_{0.27}$ bulk crystals with homogeneous composition and its thermoelectric properties" *J. Cryst. Growth* 442:102-109.

7) M. Navaneethan, **M. Sabarinathan**, S. Harish, J. Archana, K. D. Nisha, Y. Hayakawa, S. Ponnusamy and C. Muthamizhchelavan, (2015) "Chemical synthesis and functional properties of multi-ligands passivated lead sulfide nanoparticles" *Mater. Lett.* 158:75-79.

8) J. Archana, **M. Sabarinathan,** M. Navaneethan, S. Ponnusamy, C. Muthamizhchelvan, and Y. Hayakawa, (2014) "Chemical synthesis and functional properties of hexamethylenetetramine capped ZnSe nanorods" *Mater. Lett.* 125:32-35.

(C) Conferences

1) **M. Sabarinathan**, S. Harish, J. Archana, M. Navaneethan, H. Ikeda T. Koyama and Y. Hayakawa "Controlled synthesis of monodispersed MoS_2 layered nanostructures by a ligand-assisted hydrothermal growth for the ultrafast degradation of organic pollutant" PP 22, (6^{th} Shizuoka University International Symposium 2016, Shizuoka University, Hamamatsu, Japan, Dec 8-9, 2016).

2) **M. Sabarinathan**, S. Harish, M. Navaneethan, J. Archana, H. Ikeda and Y. Hayakawa "Controlled synthesis of 2-D layered MoS_2 nanostructures for enhanced photocatalytic activity under visible light irradiation" PP 25, (The 18^{th} Takayanagi Kenjiro Memorial Symposium, Shizuoka University, Hamamatsu, Japan, Nov 15-16, 2016).

3) **M. Sabarinathan**, M. Omprakash, S. Harish, M. Navaneethan, J. Archana, S. Ponnusamy, H. Ikeda, T. Takeuchi, C. Muthamizhchelvan and Y. Hayakawa "Influence of silver on the conductivity and thermoelectric properties of Bi_2Te_3 nanostructures" PP-1260, (Asian Consortium on Computational Materials Science Theme meeting on First Principles Analysis & Experiment: Role in Energy Research, SRM University, Chennai, Tamilnadu, India, Sep 22-24, 2016).

4) **M. Sabarinathan**, S. Harish, M. Navaneethan, J. Archana, H. Ikeda and Y. Hayakawa "Controlled synthesis of layered MoS_2 nanosheets for ultrafast photocatalytic activity

under visible light irradiation" OP 23, (JST SAKURA and SSSV Seminar program, Shizuoka University, Hamamatsu, Japan, Aug 31, 2016).

5) **M. Sabarinathan**, M. Navaneethan, J. Archana, M. Omprakash, T. Koyama, H. Ikeda, Y. Hayakawa "Synthesis of bismuth antimony telluride alloyed nanostructures for thermoelectric applications" OP 18, (JST SAKURA and SSSV Seminar program, Shizuoka University, Hamamatsu, Japan, Sep 2, 2015).

6) **M. Sabarinathan**, S. Harish, A. Silambarasan, M. Navaneethan, S. Ponnusamy, C. Muthamizhchelvan and Y. Hayakawa "Synthesis and characterization of pyrrolidine and dodecylamine passivated CuO nanostructures" PP50, (International conference on advances in civil engineering and chemistry of innovative materials- ACECIM'14, SRM University, Ramapuram campus, Chennai, India Mar 13-14, 2014).

7) **M. Sabarinathan,** A. Silambarasan, M. Navaneethan, S. Ponnusamy, Helen P. Kavitha, Y. Hayakawa, "Synthesis of Glutamine capped ZnS nanoparticles- an investigation on their photocatalytic activity" PP-17, pp.- 35. (National Conference on Hierarchically structured materials (NCHSM 2013), SRM University, Chennai, India, Jan 24-25, 2013).

8) **M. Sabarinathan,** A. Silambarasan, Helen P. Kavitha, S. Ponnusamy, M. Navaneethan, and Y. Hayakawa "Synthesis of L-Glutamine capped ZnS nanoparticles and its an investigation on its photocatalytic activity" PP 17, (National conference on advanced materials for the emerging technologies-CAMET'13, Sri Ramakrishna Mission Vidhyalaya college of Arts & Science, Coimbatore, India, Jul 11-12, 2013).